POLITECNICO DI MILANO

School of Industrial and Information Engineering

Master of Science in Mechanical engineering

POLITECNICO
MILANO 1863

Lightweight design of mechanical components of a Shell Eco-marathon vehicle

Supervisor: Prof. Gianpiero Mastinu

Co-supervisor: Ing. Pietro Stabile

MSc thesis of Andrea Rongoni 905996

Academic Year 2019/2020

Abstract

The present thesis is devoted to the *lightweight design* of mechanical components of a vehicle for the *Shell Eco-marathon* competition. The work is focused on the design of the suspension supports and the wheel hubs. In the design process, optimization techniques are employed in order to minimize the mass while ensuring stiffness and safety.

For the design of suspension supports, the variation of the wheel camber and toe angles under the effect of race loads is analysed. The process is performed with the aid of analytical and numerical methods.

For the design of the wheel hubs, *topology optimization* techniques are employed to obtain a preliminary optimized shape. The topology optimization process is followed by CAD modelling and detailed FE analyses in order to assess the stiffness and structural integrity of the components.

As result, the designed components allow a mass reduction of about 65% compared to the existing components.

Keywords: *lightweight design, Shell Eco-marathon*, *topology optimization*.

Sommario

La presente tesi è dedicata al *lightweight design* di componenti meccanici di un veicolo per la competizione *Shell Eco-marathon*. Il lavoro si concentra sulla progettazione dei supporti delle sospensioni e dei mozzi delle ruote. Nel processo di progettazione, vengono utilizzate tecniche di ottimizzazione al fine di ridurre al minimo la massa garantendo rigidità e sicurezza.

Per la progettazione dei supporti delle sospensioni, viene analizzata la variazione degli angoli di camber e convergenza della ruota sotto l'effetto dei carichi durante la corsa. Il processo viene eseguito con l'ausilio di metodi analitici e numerici.

Per la progettazione dei mozzi delle ruote, vengono utilizzate tecniche di *ottimizzazione topologica* per ottenere una forma preliminare ottimizzata. Il processo di ottimizzazione topologica è seguito dalla modellazione CAD e da analisi FE dettagliate per valutare la rigidità e l'integrità strutturale dei componenti.

Come risultato, i componenti progettati consentono una riduzione di massa di circa il 65% rispetto ai componenti esistenti.

Parole chiave: *lightweight design, Shell Eco-marathon*, *ottimizzazione topologica*.

Contents

Abstract I
Sommario III
List of figures VII
List of tables XI
1 Introduction 1
2 Shell Eco-marathon 3
2.1 The competition 3
2.2 The categories 4
2.3 Politecnico di Milano and Shell Eco-marathon 5
3 State of the art 9
3.1 Vehicle design and specifications 9
3.2 Suspension system 10
3.3 Forces acting on the vehicle 12
3.3.1 Design loads 13
3.3.2 Race condition loads 14
4 Design of the suspension supports 15
4.1 Scheme and dimension of the suspensions 16
4.2 Forces and stresses calculation 18
4.2.1 Forces on the bearings and clamps 18
4.2.2 Internal forces and stresses 21
4.3 Sizing of the suspension tubes 24
4.3.1 Characteristic angles variation 26
4.4 Clamp and bearing pressure 30
4.5 Finite elements analysis 31
4.5.1 Creation of the model 32
4.5.2 FEM results 35
5 Design of the wheel hubs 39
5.1 Hubs components 39
5.2 Front Axle 41
5.2.1 Optimization of the internal diameter 47
5.3 Rear axle 51
5.4 Front hub 52

5.4.1 Basic topology optimization 52
5.4.2 Preliminary design 58
5.4.3 Shape optimization 64
5.5 Front hub and axle interaction 70
5.5.1 Shrink-fit 71
5.5.2 Characteristic angles variation 77
5.6 Rear Hub 78
5.6.1 Basic topology optimization 79
5.6.2 Preliminary design 82
5.6.3 Shape optimization 84
5.7 Rear hub and axle interaction 88
5.7.1 Shrink-fit 88
5.7.2 Characteristic angles variation 92
6 Conclusions 95
Appendix 97
Bibliography 103

List of figures

Figure 2.1 – Shell Eco-marathon participants 3
Figure 2.2 – Prototype vehicles 4
Figure 2.3 – Urban concepts 4
Figure 2.4 – Joulemeter 5
Figure 2.5 – Why Not?, first prototype vehicle of Politecnico di Milano 5
Figure 2.6 – Prototype Artemide 6
Figure 2.7 – Prototype Apollo, recognizable by the solar panel 6
Figure 2.8 – Urban concept Daphne in 2018 7
Figure 2.9 – Urban concept Leto 8
Figure 3.1 – Chassis 9
Figure 3.2 – CFD analysis 9
Figure 3.3 – Leto's drivetrain 10
Figure 3.4 – Car electronic system 10
Figure 3.5 – Suspension arrangement 11
Figure 3.6 – Detail of the mounting of the front tube 11
Figure 3.7 – Element connection 12
Figure 3.8 – Longitudinal load distribution 13
Figure 4.1 – Mounting of the suspension 15
Figure 4.2 – Tube dimensions 15
Figure 4.3 – Bearing application point 16
Figure 4.4 – Scheme of the front left suspension, top view 17
Figure 4.5 – Scheme of the front left suspension, front view 17
Figure 4.6 – Tube scheme 17
Figure 4.7 – Forces on the suspension 18
Figure 4.8 – Force from the rubber bumper 19
Figure 4.9 – Angular bearing axial forces 19
Figure 4.10 – Suspension tube scheme and forces 20
Figure 4.11 – Shear and bending, front tube 22
Figure 4.12 – Shear and bending, front tube curve only 23
Figure 4.13 – Shear and bending, rear tube 23
Figure 4.14 – Camber and toe definition 26
Figure 4.15 – Pinned-pinned beam deflection 27
Figure 4.16 – Relation between displacements and angle 28
Figure 4.17 – Front tube angles variation 28
Figure 4.18 – Rear tube angles variation 29
Figure 4.19 – Pressure distribution in a bolted coupling 30
Figure 4.20 – Front tube partition 32
Figure 4.21 – Rear tube partition 32
Figure 4.22 – Coupling of the clamps 33
Figure 4.23 – Axial load 34
Figure 4.24 – Bearing loads, front tube 34
Figure 4.25 – Meshed tube 35
Figure 4.26 – Detail of the mesh refinement on the fillet 35

Figure 4.27 – Circular path 36
Figure 4.28 – Axial stress graphs 36
Figure 5.1 – Photo of the front hub 39
Figure 5.2 – Front hub and hub-carrier 40
Figure 5.3 – Rear hub and hub-carrier 40
Figure 5.4 – Axle and wheel scheme 42
Figure 5.5 – Axle scheme 42
Figure 5.6 – Hub forces 43
Figure 5.7 – Brake force 43
Figure 5.8 – Shear and bending plots, braking case 46
Figure 5.9 – Shear and bending plots, NO braking case 46
Figure 5.10 – Partition of the beam in two elementary subsystems 48
Figure 5.11 – Front axle angles variation 50
Figure 5.12 – Rear axle 51
Figure 5.13 – Front hub 52
Figure 5.14 – Design space dimensions 53
Figure 5.15 – Basic geometry 53
Figure 5.16 – Design space highlighted in brown 54
Figure 5.17 – Connections 54
Figure 5.18 – Shape controls 55
Figure 5.19 – Hub scheme 55
Figure 5.20 – Result of the mass minimization process 56
Figure 5.21 – Result of the stiffness maximization, isometric front view 57
Figure 5.22 – Result of the stiffness maximization, front view 57
Figure 5.23 – Result of the stiffness maximization, isometric rear view 58
Figure 5.24 – Preliminary geometry, first version 59
Figure 5.25 – Shrink fit coupling 59
Figure 5.26 – Wheel coupling 60
Figure 5.27 – Brake coupling 60
Figure 5.28 – First concept front stresses 61
Figure 5.29 – First concept brake supports stresses 61
Figure 5.30 – First concept notch stress 62
Figure 5.31 – Preliminary design dimensions 62
Figure 5.32 – Preliminary design, front and rear isometric view 63
Figure 5.33 – Preliminary design holes stress 63
Figure 5.34 – Preliminary design wheel supports stress 64
Figure 5.35 – Preliminary design brake supports stress 64
Figure 5.36 – Schematization of the supports 65
Figure 5.37 – Thickness parameter 66
Figure 5.38 – Inclination parameter 66
Figure 5.39 – Stiffness-mass variation diagram 68
Figure 5.40 – Axle partitioning 73
Figure 5.41 – Bearings and bolted joints' couplings 74
Figure 5.42 – Surface-to-surface contact of the shrink-fit 74
Figure 5.43 – Shrink-fit mesh 75
Figure 5.44 – Paths 75
Figure 5.45 – Front hub shrink-fit stresses 76
Figure 5.46 – Rear hub 78
Figure 5.47 – Rear hub design space 79
Figure 5.48 – Connections 79
Figure 5.49 – Shape control 80
Figure 5.50 – Result of the stiffness maximization, isometric front view 81
Figure 5.51 – Result of the stiffness maximization, front view 81

Figure 5.52 – Result of the stiffness maximization, isometric rear view 82
Figure 5.53 – Preliminary design dimensions 82
Figure 5.54 – Preliminary design, front and rear isometric view 83
Figure 5.55 – Couplings 83
Figure 5.56 – Stresses 84
Figure 5.57 – Thickness parameter 84
Figure 5.58 – Angle parameter 85
Figure 5.59 – Stiffness-mass variation diagram 86
Figure 5.60 – Rear hub couplings 90
Figure 5.61 – Detail of the brake disc coupling 91
Figure 5.62 – Paths 91
Figure 5.63 – Rear hub shrink-fit stresses 92

List of tables

Table 3.1 – Vehicle data 12
Table 3.2 – Vehicle forces 13
Table 3.3 – Design loads 14
Table 3.4 – Race condition loads 14
Table 4.1 – Tube main properties 16
Table 4.2 – Suspension dimensions 18
Table 4.3 – Forces 21
Table 4.4 – Shear forces 21
Table 4.5 – Bending moments 22
Table 4.6 – Stresses of the original tubes 24
Table 4.7 – Materials' properties 25
Table 4.8 – Stresses of the new tubes 25
Table 4.9 – New tube mass 26
Table 4.10 – Front tube angles variation in 1e-3° 29
Table 4.11 – Rear tube angles variation in 1e-3° 29
Table 4.12 – Contact pressures 31
Table 4.13 – Von-Mises stresses 31
Table 4.14 – Bearings' forces application direction 33
Table 4.15 – Axial stress, maximum values 37
Table 4.16 – K_t evaluation 37
Table 5.1 – Main components, front 40
Table 5.2 – Main components, rear 41
Table 5.3 – Hubs materials and mass 41
Table 5.4 – Material properties 41
Table 5.5 – Axle dimensions 42
Table 5.6 – Forces on the front axle 45
Table 5.7 – Shear and bending internal forces 47
Table 5.8 – Angles variation for the original axle (thousandths of degree) 49
Table 5.9 – Angles variation for the maximum inner diameter (thousandths of degree) 49
Table 5.10 – Angle boundaries (min ÷ max) 50
Table 5.11 – New front axle mass 50
Table 5.12 – Front axle angles variation 51
Table 5.13 – Front hub design loads 56
Table 5.14 – Front hub sensitivity analysis 67
Table 5.15 – Variations ratios 68
Table 5.16 – Front hub race loads 69
Table 5.17 – Front hub results 70
Table 5.18 – Shrink-fit data 72
Table 5.19 – Shrink-fit results 73
Table 5.20 – Analytic and FEM results comparison 76
Table 5.21 – Single contact force loads 77
Table 5.22 – Front hub angle deflection (in thousandths of degrees) 78
Table 5.23 – Rear hub design loads 80

Table 5.24 – Rear hub sensitivity analysis 85
Table 5.25 – Variations ratios 86
Table 5.26 – Rear hub race loads 87
Table 5.27 – Rear hub results 87
Table 5.28 – Shrink-fit data 89
Table 5.29 – Shrink fit results 90
Table 5.30 – Analytic and FEM results comparison 92
Table 5.31 – Brake forces 92
Table 5.32 – Rear hub deflections (in thousandths of degrees) 93
Table 6.1 – Mass 95
Table 6.2 – Camber and toe angles variation at front 96
Table 6.3 – Camber and toe angles variation at rear 96

1 Introduction

Issues such as energy efficiency and eco–sustainable development are of great importance in this historical phase, characterized by a delicate economic situation and numerous issues related to energy and emission reduction.

One of the most source of pollution is represented by vehicle emission into urban areas. In 2011 the European Commission released a "*White paper of transportation*" in which it made a list of some concrete initiatives to reduce the pollution emission and build a competitive transport system; for example, for 2050 it's committed to not use any more conventionally – fuelled cars in cities. In this field, Mechanical Department of Politecnico di Milano coordinates several projects related to automotive sector, which they propose to develop and optimize high-sustainability electric vehicles, through the spread of which it is possible to reduce emissions localized in urban centers.

According to a relationship used also by the *New European Driving Cycle* [1], known as *NEDC* (even if it is almost obsolete, but for these considerations results helpful), to estimate the energy consumed for travel a fixed distance (100km), it's possible to highlight the main parameters which influence the energy consumption for a generic road vehicle:

$$E = A \cdot C_x \cdot 1.9 \cdot 10^4 + m \cdot f_r \cdot 8.4 \cdot 10^2 + m \cdot 10 \left[\frac{kJ}{100\ km}\right]$$

So, the energy consumed is directly related to the cross-sectional area of the vehicle (A), the drag coefficient (C_x), the rolling resistance of tires (f_r) and the vehicle mass (m). This relationship is fundamental for preliminary powertrain design, both for internal combustion engine and for electric powertrain.

In particular, after a sensitivity analysis involving each parameter separately, it's possible to state that the vehicle mass reduction is the more effective way to reduce the energy required to travel. In fact, mass reduction allows vehicles to accelerate more rapidly and this could lead to a general downsizing of others mechanical subsystems, like the powertrain itself.

Since 2005, Mechanical Department of Politecnico di Milano supports a team of students and researchers who develop low-emissions prototype participating at the international competition *Shell Eco-Marathon®*, to encourage the experimentation of a series of innovative solutions which, hopefully, can be applied to common urban transport vehicles. The last vehicle, called *LETO*, was entirely made in 2019 by the members of *Team Mecc e-*, composed by Politecnico di Milano students.

The main topic of this thesis work is the lightweight redesign of oversized component of the last year car, reducing the overall mass of the vehicle and thus increase efficiency. In the following chapters are described:

- *Shell Eco-marathon*: an introduction to the Shell Eco-Marathon® competition, how it is organized, what are the main aspects and goals and what is the contribution of Politecnico di Milano at Shell Eco-Marathon® during years;

- *State of the art*: a brief description of the 2019 Politecnico di Milano vehicle with a focus on the suspension system and the definition of the loads used during the design process;
- *Design of the suspension* : the chapter focus on the resizing of the suspension tubes, analysing the contribution to camber and toe angles variation;
- *Design of the wheel hubs*: it is about the redesign process of three different elements: front axle, front hub and rear hub, by means of topology and shape optimization techniques, in order to minimize the mass in compliance with the displacements constraints;
- *Conclusions*: presentation of the obtained results for all the components analysed.

2 Shell Eco-marathon

2.1 The competition

The story of Shell Eco-marathon began in 1939, when a group of Shell's researchers from Wood River, Illinois (USA), bet on who would drive his car farther away with just one gallon of gasoline; then, the first edition of public European Shell Eco-Marathon held in 1985.

The competition is one of the most important education and training projects on sustainable mobility, for young people, from all over the world. The aim of the project is to promote values such as respect for the environment, energy efficiency and comprehension of individual and cultural diversity. Over the last few years, competition has become increasingly important and attracted a lot of attention, thanks to the extraordinary records obtained.

Figure 2.1 – Shell Eco-marathon participants

Shell Eco-Marathon is a competition in which university students and research institutes challenge each other to design, build and drive the most efficient vehicles. The vehicle that covers the race distance, using the least amount of energy and within a given time, is the winner.

Teams must complete a predetermined number of laps within a specified maximum time with an average speed that changes according to the category, and each team has four attempts to score the best result. Top research level is employed for the vehicles' development, adopting the newest kind of technologies. The safety aspect of the race, summarized by the race Technical director as "safety first" rule, is a relevant constraint for the vehicle design.

To reward the teams' effort in term of innovation and safety, Shell has instituted a technical innovation, a vehicle design and a safety design award, in addition to the energy efficiency prize.

2.2 The categories

The vehicles participating in the Shell Eco-Marathon are divided into two categories: the *Prototype* category (*Figure 2.2*), focused on seeking the maximum efficiency, and *Urban Concept* category (*Figure 2.3*), that aims to realize energy efficient vehicles, resembling forms and general layout that can also be applied to ordinary city cars.

Figure 2.2 – Prototype vehicles

Figure 2.3 – Urban concepts

Vehicles are further classified according to the energy source: battery-electric, hydrogen fuel cell, and internal combustion engine (gasoline, diesel, or ethanol). Internal combustion fuel consumption is scored in terms of km/l of equivalent consumption in gasoline, while electric vehicles energy efficiency is expressed in terms of km/kWh. Those values are calculated by a joulemeter installed on car's electric system, with the connections shown in *Figure 2.4*. Prizes are awarded separately for each vehicle class and energy category. The pinnacle of the competition is the *Shell Eco-marathon*

Drivers' World Championship, where the most energy efficient Urban Concept vehicles compete in a race with a limited amount of energy.

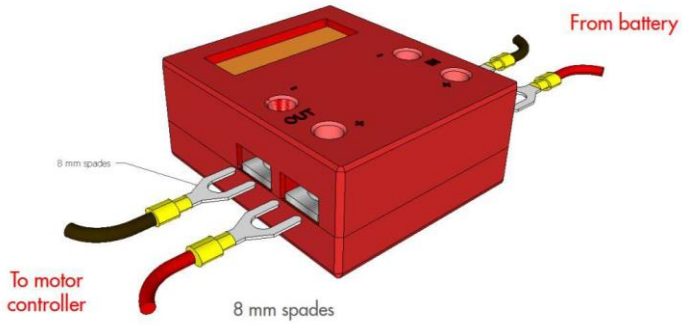

Figure 2.4 – Joulemeter

2.3 Politecnico di Milano and Shell Eco-marathon

Politecnico di Milano has been participating in Shell Eco-marathon since 2005: the team is always composed mainly by students, who put together their theoretical knowledge and practical abilities to the realization of the vehicle.

The first project was a prototype car called *Why Not?* (*Figure 2.5*), powered by gasoline engine, which has been converted into an electric type in 2008, powered by a hydrogen fuel cell. The prototype Why Not? scored 1931km/l in the Shell Eco-Marathon UK 2008, obtaining the Italian record for the hydrogen-fuelled prototype category in that year.

Figure 2.5 – Why Not?, first prototype vehicle of Politecnico di Milano

In 2009, Politecnico di Milano introduced a new prototype called *ARTEMIDE* (*Figure 2.6*), powered again by a hydrogen cell. The design has been strongly optimized: it has two wheels at the front axle

and one steering and driving wheel at the rear axis; the chassis was no longer made by aluminium tubes, but it turned into a CFRP monocoque, allowing a better aerodynamic design as well. The name is an acronym of the words Aerodynamics, Resistance, Frame (Telaio), Electronics, Modeling, Hydrogen (Idrogeno), DEsign. ARTEMIDE scored the Italian record of 2741 km/l in its category and won the Design Award.

Figure 2.6 – Prototype Artemide

In 2010, the prototype faced an evolution, introducing a partially new vehicle called *Apollo* (*Figure 2.7*). The main innovation consisted in the adoption of a photovoltaic cells system, installed on a wing body at the rear end. During the 2011 edition, *Apollo* scored the record of 1108 km/kWh, equal to 9757 km/l. This extraordinary result represented the lowest consumption ever made by a vehicle in the Shell Eco-Marathon competition.

Figure 2.7 – Prototype Apollo, recognizable by the solar panel

Since 2011, Politecnico di Milano decided to move to the Urban Concept category, giving birth to the new vehicle called *Daphne* (*Figure 2.8*). This was the vehicle with which Politecnico di Milano

competed until 2018, the year of the last race that matched the achievement of its best result: 130 km/kWh and fifth place at the Shell Eco-marathon Europe. Over the years the vehicle has undergone several changes, especially to deal with regulatory changes. The main features of the latest version are described below.

The vehicle is made of a CFRP structural monocoque and due to the changing rules, an external non-structural bodywork has been added to the original monocoque, in order to comply to the latest rules, requiring covered wheels and a closed external profile.

The suspension layout is a double wishbone with parallel arms and independent wheels, which is suitable for an easy tuning of the suspension parameters. The attachment to the chassis is represented by conventional ball joint system.

The steering system presents a configuration that allows to have a camber steering effect, with the aim to minimize the wheels working space, hence the vehicle's frontal area. This system is actuated by a slider, attached to the suspension's upper wishbone. Previously the steering system had a four steering wheels configuration.

Daphne is powered by two 200 Watt electric DC brushed motors, mounted on the rear wheels through single gear transmission. Each motor has a pinion directly mounted on the motor shaft. Pinion engage with a gear mounted on the wheel axis through a freewheel. The power source consists in a 48 Volt Lithium Ion battery pack, with a maximum capacity of 6800 mAh.

Figure 2.8 – Urban concept Daphne in 2018

For the 2019 competition the team decided to compete with a completely new vehicle, called Leto (*Figure 2.9*), belonging to the Urban Concept battery electric category. In the 2019 edition of Shell Eco marathon, Leto scored an energy consumption of 184 km/kWh, with an overall 4th place at the end of the competition, the best result ever for Politecnico di Milano team in the urban concept category.

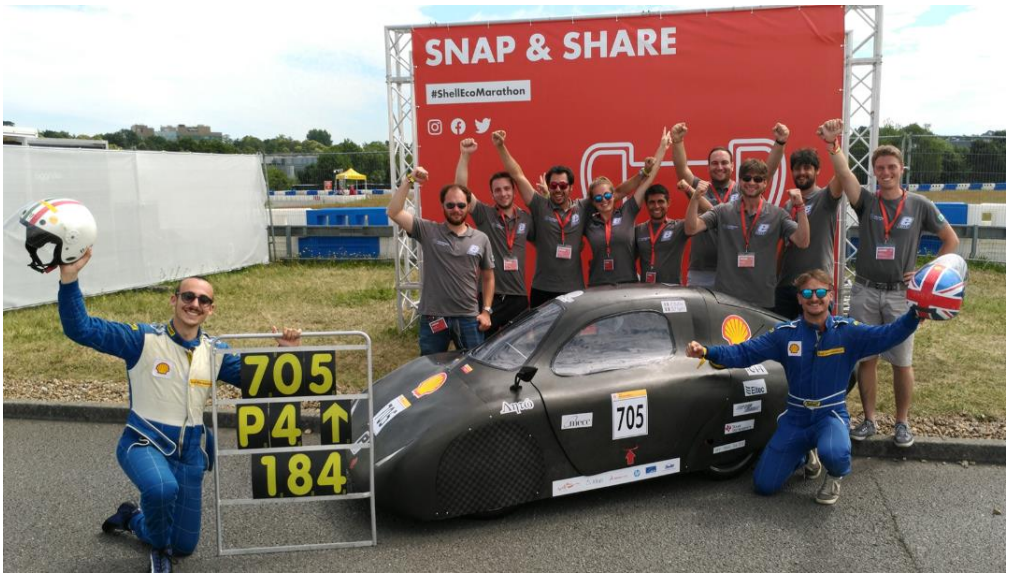

Figure 2.9 – Urban concept Leto

Design and specification of the new vehicle are described in chapter *3.1*.

3 State of the art

3.1 Vehicle design and specifications

The vehicle is a one seat, four-wheel car, particular designed for the competition. The chassis and the body (*Figure 3.1*) are entirely made from composite materials [2]. The chassis is a floor that completely covers the vehicle from the bottom and is designed as a sandwich structure with *carbon fiber skins* and an *expanded polypropylene* (*EPP*) core. The body is a sandwich structure with a *honeycomb* core and carbon fiber skins. Front nose, doors and rear tail of the bodywork are fixed to these two parts.

The external shape is the result of in-depth fluid dynamics analysis aimed at maximizing the aerodynamic efficiency [3] (*Figure 3.2*).

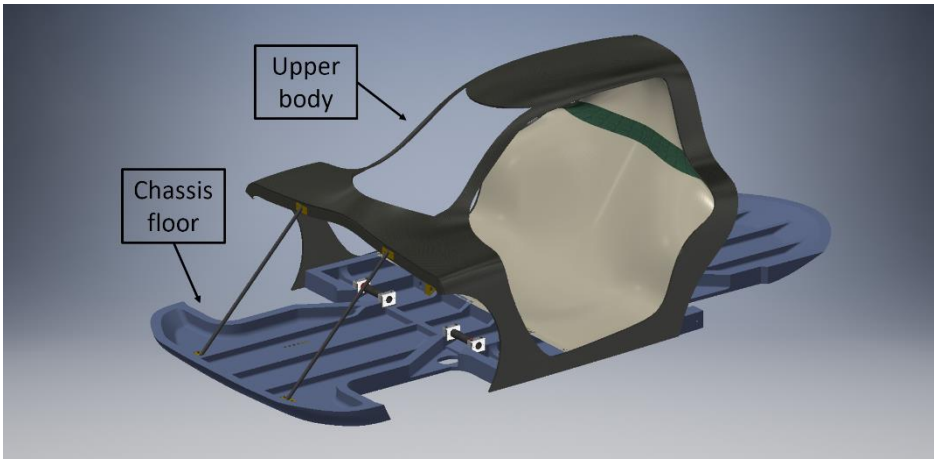

Figure 3.1 – Chassis

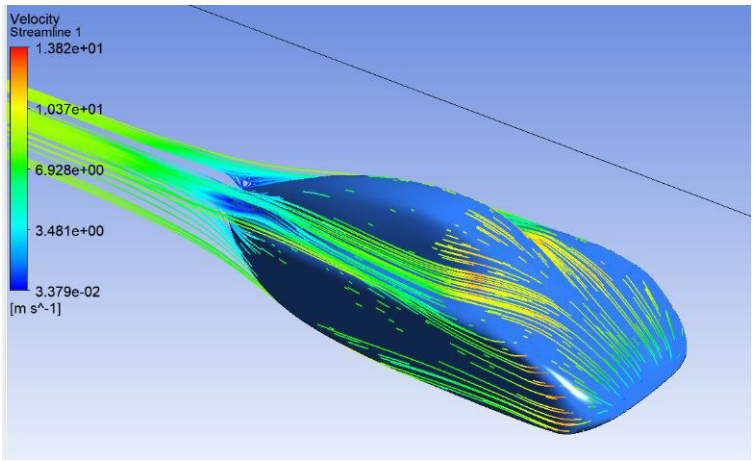

Figure 3.2 – CFD analysis

The vehicle is moved by an electric drivetrain powered by a Li-Ion battery pack. Two brushed DC motors are used with an overall power output of 400 W. The two DC motors are mounted on the two rear wheels. Transmission is realized by gear pairs. Each motor has a pinion directly mounted on the motor shaft. Pinion engages with a gear connected to the wheel hub (*Figure 3.3*).

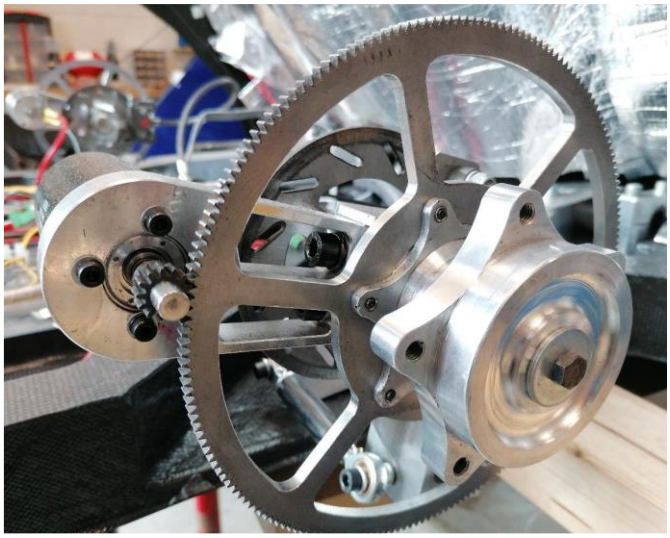

Figure 3.3 – Leto's drivetrain

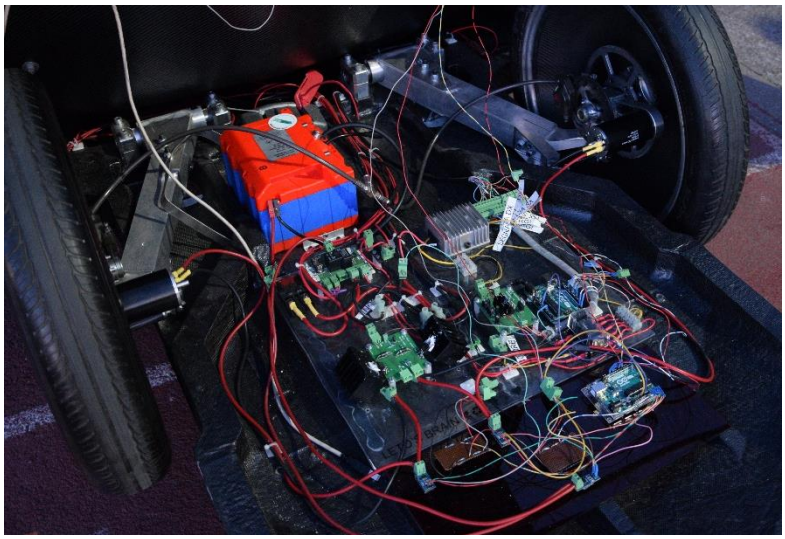

Figure 3.4 – Car electronic system

3.2 Suspension system

The vehicle is provided with trailing arms layout suspension system. Pros of this solution are:

- Simplicity, so cheaper and easier to design and manage
- Low room required, to increase driver comfort and more space to fit all mechanical and electronical components (*Figure 3.4*); the compactness allow to design a body with small cross area, thus reducing aerodynamic resistance and consumption

- No lateral slip, useful to reduce energy dissipation from tyres during vertical displacement caused by the irregularities and obstacles

The principal con of this solution is the absence of camber recovery: this means that the wheels camber angle in curve is equal to the chassis roll angle.

Figure 3.5 shows the arrangement of the suspension on the chassis.

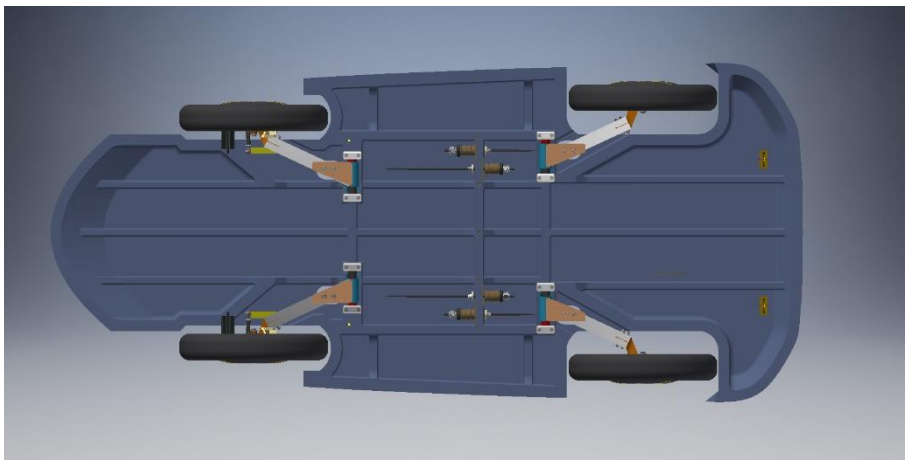

Figure 3.5 – Suspension arrangement

The suspension arm is mounted on a steel tube through two angular contact ball bearings. Two aluminium clamps fix the tube to the chassis (*Figure 3.6*). The suspension arm is then connected to the elastic element of the suspension system through the connection rod shown in *Figure 3.7*. Rubber bumpers are employed as elastic elements.

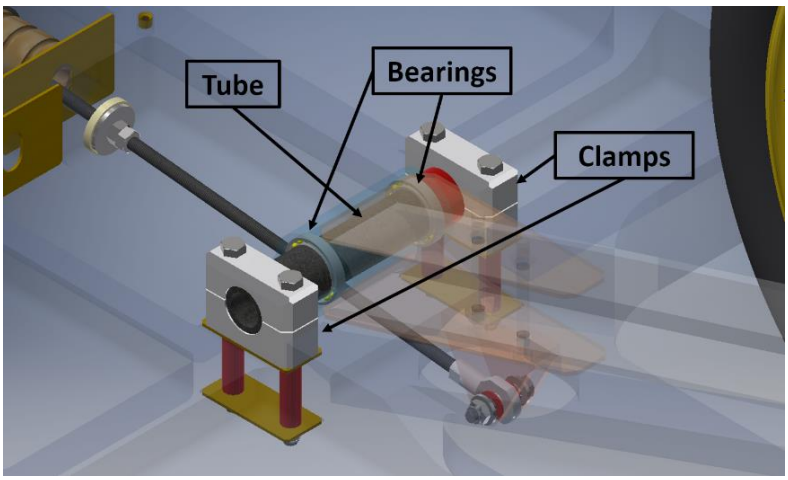

Figure 3.6 – Detail of the mounting of the front tube

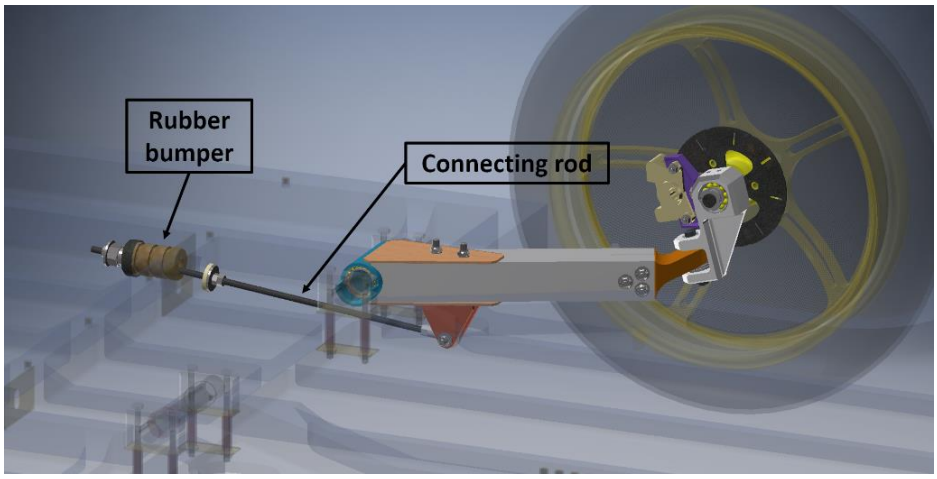

Figure 3.7 – Element connection

3.3 Forces acting on the vehicle

Simple models are used for the calculation of wheel-road contact forces acting in different load conditions:

- load due to gravitational force
- load during braking
- load in the cornering phase

Table 3.1 shows the data used.

Table 3.1 – Vehicle data

Vehicle mass	90 kg
Driver mass	70 kg
Total mass	160 kg
Wheelbase	1460 mm
Front wheel gauge	1000 mm
Rear wheel gauge	850 mm

The reference system has been defined as follow:

- X axis: longitudinal direction, pointing backward for the front wheel and frontward for the rear one
- Y axis: lateral inward direction
- Z axis: vertical upward direction

3.3.1 Design loads

Design load are used to verify the failure resistance of the redesigned parts. Total forces acting on the vehicle (*Table 3.2*) were simply calculated as

$$F = m \cdot a$$

where m is the total mass and a the acceleration, in particular [4]:

- Longitudinal force: deceleration under braking is considered constant and equal to 1 g (9.81 m/s²), $F_{long} = 160\ kg \cdot 9.81\ \frac{m}{s^2} \sim 1600\ N$
- Lateral force: is considered a constant lateral acceleration, so constant radius and speed, of 1 g, the result is again $F_{lat} = 1600\ N$
- Vertical force: considering a safety factor $\alpha = 3$ that takes into account the dynamic load coming from the uneven road, the equivalent force is $F_{vert} = m \cdot g \cdot \alpha = 160 \cdot 9.81 \cdot 3 \sim 4800\ N$

Table 3.2 – Vehicle forces

Longitudinal force	1600 N
Lateral force	1600 N
Vertical force	4800 N

For the computation of the resultant forces acting on each wheel, the quarter car model was considered: total forces were divided on each wheel and load transfers neglected.

First the forces must be divided between front and rear axle (*Figure 3.8*):

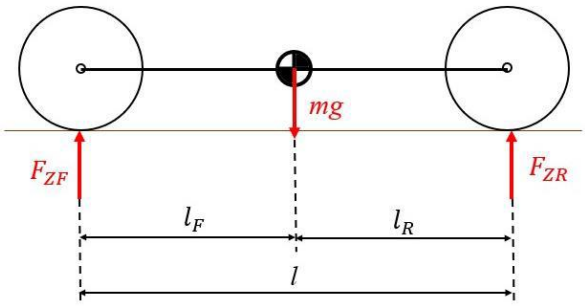

Figure 3.8 – Longitudinal load distribution

$$F_{ZF} + F_{ZR} = F_{vert}$$
$$F_{ZF} \cdot l_F - F_{ZR} \cdot l_R = 0$$

where F_{ZF} and F_{ZR} are the total vertical forces acting on the front and rear axles respectively.

These forces are then equally distributed on the two wheel of each axle: this means, being the load distribution nearly equal to 50:50 ($l_F \cong l_R$), on each wheel act a force equal to a fourth to those previously described, as shown in *Table 3.3*.

Table 3.3 – Design loads

Longitudinal force	400 N
Lateral force	400 N
Vertical force	1200 N

3.3.2 Race condition loads

Camber and toe angles variation must be calculated using race condition loads and not the ones used for designing the parts: from the data of the past Shell Eco-marathon competitions can be observed that the longitudinal acceleration is around 0.4 g and the lateral 0.3 g. For the vertical force is applied gravity only.

As calculated before, the force acting on a wheel are a quarter of the total forces acting on the vehicle. Considering again constant accelerations:

$$F_{long} = \frac{1}{4} m_{tot} \cdot a_{long} = 160\ N$$

$$F_{lat} = \frac{1}{4} m_{tot} \cdot a_{lat} = 120\ N$$

$$F_{vert} = \frac{1}{4} m_{tot} \cdot g = 400\ N$$

For the vertical force also the load transfer must be considered:

$$\Delta F_{z,long} = a_{long} \frac{h_{COG}}{w_{base}} mg\ , \qquad \Delta F_{z,lat} = a_{lat} \frac{h_{COG}}{w_{gauge}} mg$$

where h_{COG} is the centre of gravity height, w_{base} the wheelbase and w_{gauge} the wheel gauge.

Longitudinal load transfer must be added on front wheels and subtracted at rear during braking, lateral load transfer is added at the external wheels and subtracted to the inner ones during curve. These values must be also divided by 2 before being applied on the single wheel. The resultant forces are reported in *Table 3.4*, expressed in the relative reference system.

Table 3.4 – Race condition loads

	weight	braking	Internal curve	External curve	Int curve + braking	Ext curve + braking
Front F_x	0	160 N	0	0	160 N	160 N
Front F_y	0	0	-120 N	120 N	-120 N	120 N
Front F_z	400 N	476.7 N	316 N	484 N	392.7 N	560.7 N
Rear F_x	0	-160 N	0	0	-160 N	-160 N
Rear F_y	0	0	-120 N	120 N	-120 N	120 N
Rear F_z	400 N	323.3 N	301.2 N	498.8 N	224.5	422.1 N

4 Design of the suspension supports

In this chapter the lightweight design process of the suspension supports is presented. First the schematization of the suspension system is described, then forces and stresses calculation and evaluation of the characteristic angles variation are expounded.

Figure 4.1 pictures the mounting of the suspension to the chassis.

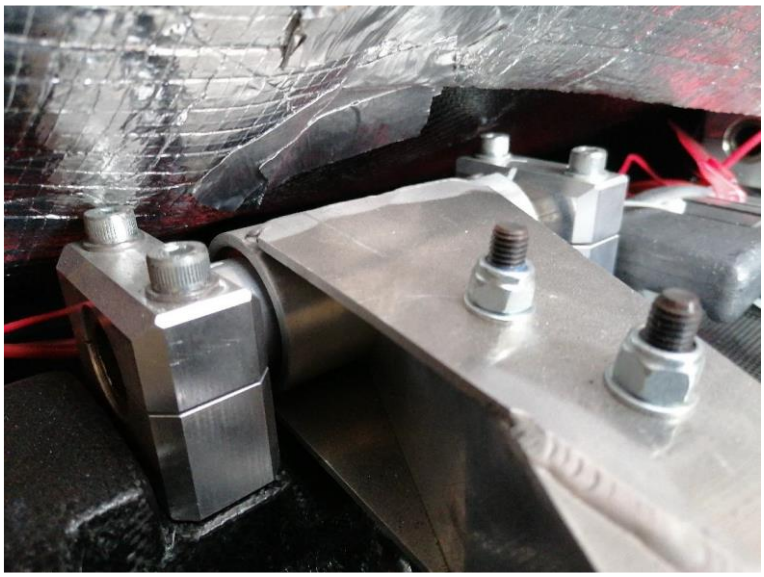

Figure 4.1 – Mounting of the suspension

Actually the suspension support consists of a steel tube. *Figure 4.2* shows its dimensions and in *Table 4.1* main properties are reported.

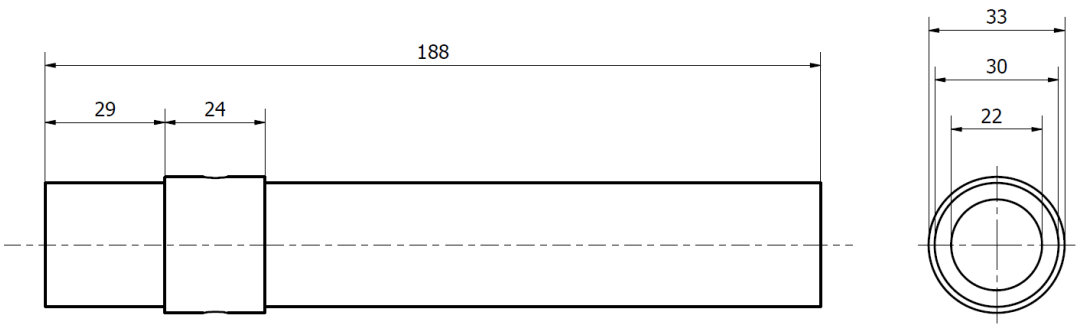

Figure 4.2 – Tube dimensions

Table 4.1 – Tube main properties

Length	188 mm
External diameter	30 mm
Internal diameter	22 mm
Material	Steel
Young modulus	206 GPa
Yield stress	750 MPa
Ultimate stress	1000 MPa
Density	7850 kg/m^3
Mass	510 g

Being oversized and heavy, we decided to redesign it.

4.1 Scheme and dimension of the suspensions

The system has been schematized as follow:

- Wheel, hub and trailing arm are considered as a rigid body that transmit the forces from ground to the angular contact bearings (mounted between arm and tube) that work as hinges, since they cannot transmit moments. Application points of these constraints have been considered on the axis and in the middle of each bearing, neglecting the distance of the virtual hinge due to the angular contact [5] (*Figure 4.3*) and its beneficial effect with the O arrangement, useful to reduce bending moments on the tube, in favour of safety;

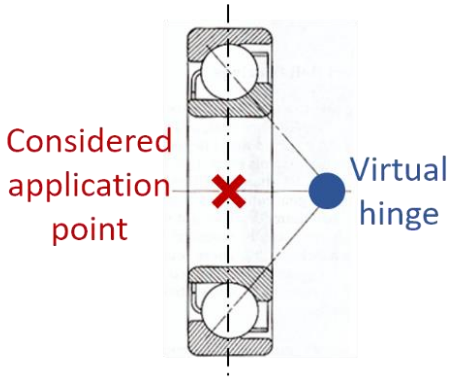

Figure 4.3 – Bearing application point

- The clamps that fix the tube to the floor are modelized, due to their compliance and the small angle considered, as pins.

Scheme and dimensions of the suspension system are shown in *Figure 4.4*, *Figure 4.5* and *Figure 4.6*.

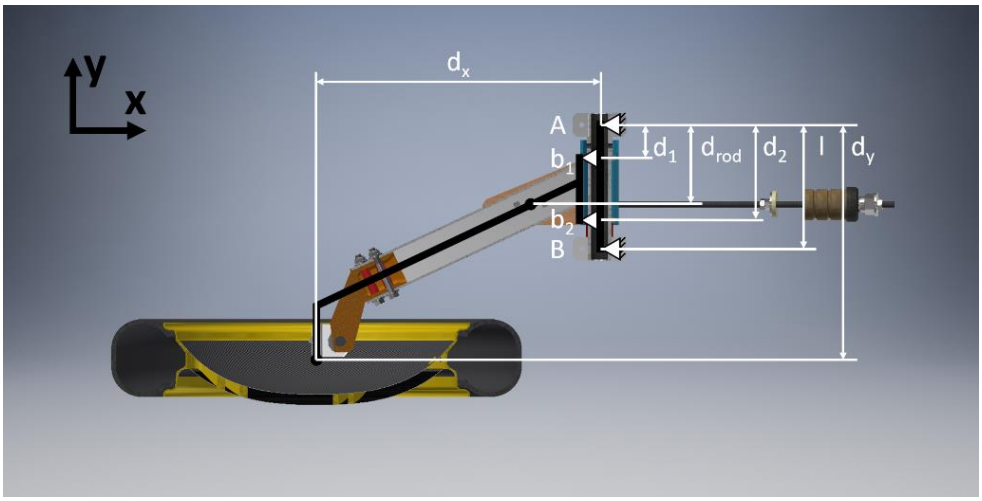

Figure 4.4 – Scheme of the front left suspension, top view

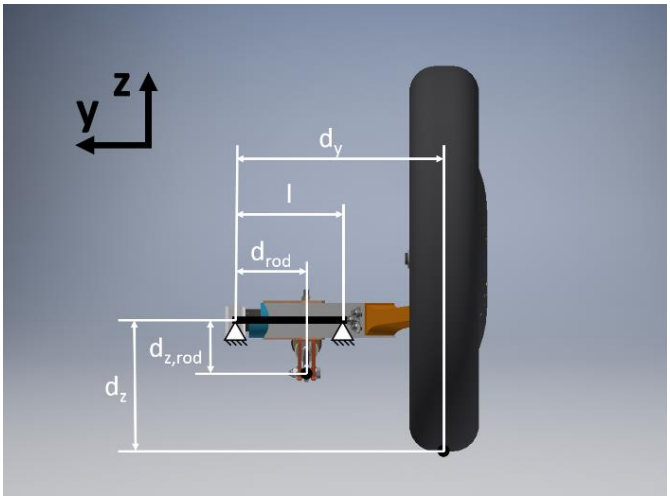

Figure 4.5 – Scheme of the front left suspension, front view

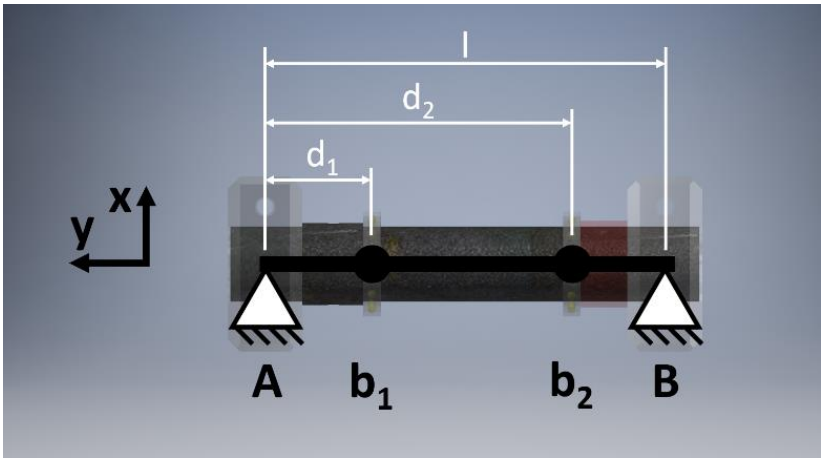

Figure 4.6 – Tube scheme

Front and rear suspension dimensions are reported in *Table 4.2*.

Table 4.2 – Suspension dimensions

Dimensions	Front	Rear
d_x	365 mm	370 mm
d_y	303 mm	308 mm
d_z	190 mm	190 mm
d_1	42.8 mm	49.4 mm
d_{rod}	102.8 mm	109.3 mm
$d_{z,rod}$	76 mm	76 mm
d_2	122.8 mm	129.4 mm
l	160 mm	160 mm

4.2 Forces and stresses calculation

4.2.1 Forces on the bearings and clamps

The first step is to transport the forces from ground to the bearings on the tube; *Figure 4.7* shows scheme and forces applied.

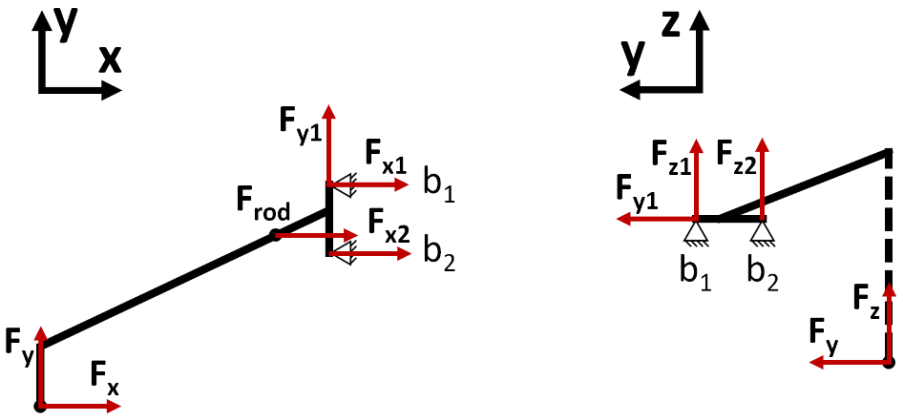

Figure 4.7 – Forces on the suspension

XY plane (horizontal):

$$\begin{matrix} Equilibrium\ along\ X: \\ Equilibrium\ along\ Y: \\ Moment\ equlibrium\ around\ A: \end{matrix} \begin{cases} Fx_1 + Fx_2 = F_x + F_{rod} \\ Fy_1 = F_y \\ Fx_1 \cdot d_1 + Fx_2 \cdot d_2 = F_x \cdot d_y - F_y \cdot d_x + F_{rod} \cdot d_{rod} \end{cases}$$

where F_{rod} is the force coming from the rubber bumper, which acts in longitudinal direction (*Figure 4.8*), and can be calculated as:

$$F_{rod} = \frac{d_x}{d_{z,rod}} F_z \cong 5\ F_z$$

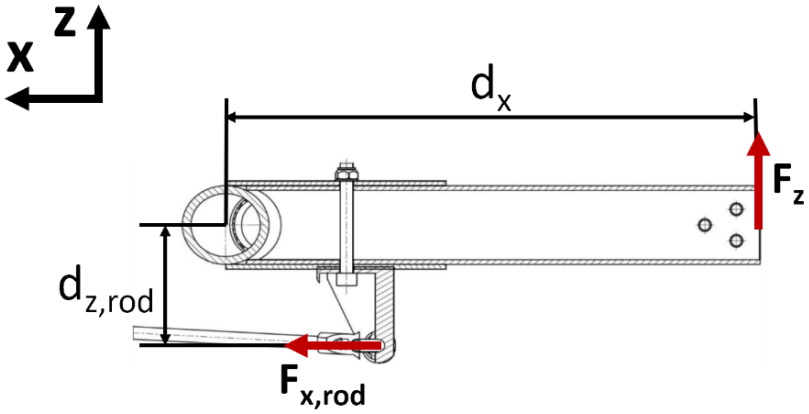

Figure 4.8 – Force from the rubber bumper

About the lateral force, the bearing which support it depends on the direction of application of the same: this is due to how single row angular contact ball bearings work, who can sustain axial force in one direction only (*Figure 4.9*).

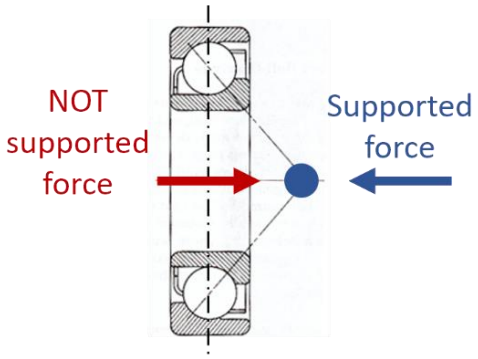

Figure 4.9 – Angular bearing axial forces

So, in case of positive F_y (inner direction) as considered, the force is transmitted by the bearing b_1, while b_2 works as a slide; vice versa for a negative F_y (external direction), it is the b_2 to support the load.

A is the internal clamp, respect which dimensions have been defined.

YZ plane (front vertical):

$$\begin{matrix} Equilibrium\ along\ Z: \\ Moment\ equlibrium\ around\ A: \end{matrix} \begin{cases} Fz_1 + Fz_2 = F_z \\ Fz_1 \cdot d_1 + Fz_2 \cdot d_2 = -F_y \cdot d_z + F_z \cdot d_y \end{cases}$$

In matrix form the equations become

$$\begin{bmatrix} 1 & 1 \\ d_1 & d_2 \end{bmatrix} \begin{Bmatrix} Fx_1 \\ Fx_2 \end{Bmatrix} = \begin{Bmatrix} F_x + F_{rod} \\ F_x d_y - F_y d_x + F_{rod} d_{rod} \end{Bmatrix}$$

$$\begin{bmatrix} 1 & 1 \\ d_1 & d_2 \end{bmatrix} \begin{Bmatrix} Fz_1 \\ Fz_2 \end{Bmatrix} = \begin{Bmatrix} F_z \\ -F_y d_z + F_z d_y \end{Bmatrix}$$

So, the equations are in the form

$$[A]\underline{u} = \underline{b}$$

and can be simply solved as

$$\underline{u} = [A]^{-1}\underline{b}$$

giving the result of the unknowns Fx_1, Fz_1, Fx_2 and Fz_1. This and the following calculations have been done with the software *Matlab*.

Now that the forces transmitted by the bearings are known, it is possible to find the constraint reactions provided by the clamps (*Figure 4.10*).

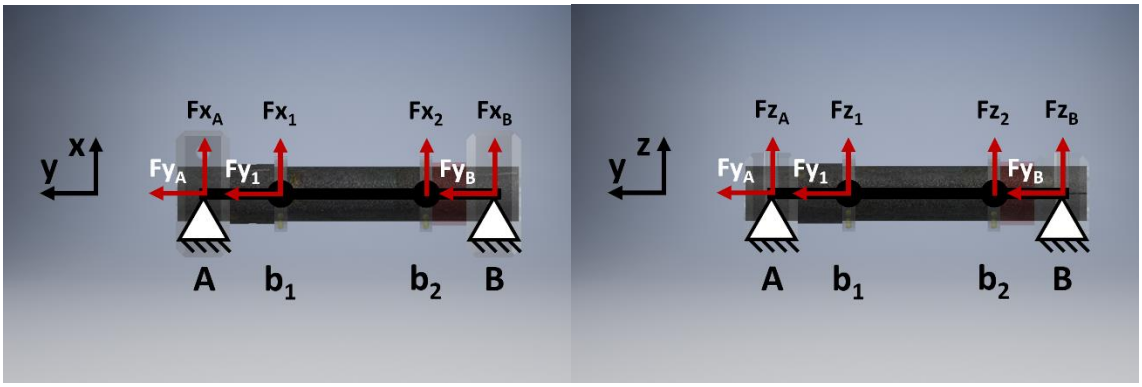

Figure 4.10 – Suspension tube scheme and forces

XY plane:

$$\begin{array}{ll} Equilibrium\ along\ X: & \begin{cases} Fx_A + Fx_B + Fx_1 + Fx_2 = 0 \\ Fy_A + Fy_B = Fy_1 \\ Fx_B \cdot l + Fx_1 \cdot d_1 + Fx_2 \cdot d_2 = 0 \end{cases} \\ Equilibrium\ along\ Y: & \\ Moment\ equlibrium\ around\ A: & \end{array}$$

YZ plane:

$$\begin{array}{ll} Equilibrium\ along\ Z: & \begin{cases} Fz_A + Fz_B + Fz_1 + Fz_2 = 0 \\ Fz_B \cdot l + Fz_1 \cdot d_1 + Fz_2 \cdot d_2 = 0 \end{cases} \\ Moment\ equlibrium\ around\ A: & \end{array}$$

Matrix form:

$$\begin{bmatrix} 1 & 1 \\ 0 & l \end{bmatrix} \begin{Bmatrix} Fx_A \\ Fx_B \end{Bmatrix} = \begin{Bmatrix} -Fx_1 - Fx_2 \\ -Fx_1 \cdot d_1 - Fx_2 \cdot d_2 \end{Bmatrix}$$

$$\begin{bmatrix} 1 & 1 \\ 0 & l \end{bmatrix} \begin{Bmatrix} Fz_A \\ Fz_B \end{Bmatrix} = \begin{Bmatrix} -Fz_1 - Fz_2 \\ -Fz_1 \cdot d_1 - Fz_2 \cdot d_2 \end{Bmatrix}$$

Can be notice that the equilibrium in the lateral direction is undetermined, since the system is hyperstatic. Anyway, since the axial stress is much lower than the bending stress, so negligible, the contribution due to Fy_1 is not be considered for the failure resistance assessment.

Previous formulas are valid both for the front and the rear suspension. The force applied are the previous described, for a condition of braking during curve at the external wheel (the most stressed). F_x has opposite sign for front and rear due to different X axis definition (positive backward at front, positive backward at rear). Furthermore, a condition of pure curve is considered at the front, the reason is clarified later.

In the *Table 4.3* data and results are summarized.

Table 4.3 – Forces

Forces	Front	Front (curve only)	Rear
F_x	400 N	0	-400 N
F_y	400 N	400 N	400 N
F_z	1200 N	1200 N	1200 N
Resultants on the bearings			
Fx_1	2424 N	3325N	4250.5 N
Fy_1	400 N	400 N	400 N
Fz_1	-1753 N	-1753 N	-1729 N
Fx_2	3976 N	2675 N	1349.5 N
Fz_2	2953 N	2953	2929 N
Constraint reactions of the clamps			
Fx_A	-2700 N	-3057.5 N	-3196.25 N
Fz_A	597.5 N	597.5 N	-1729 N
Fx_B	-3700 N	-2942.5 N	-2403.75 N
Fz_B	-1797.5 N	-1797.5 N	-1835 N

4.2.2 Internal forces and stresses

Found forces and constraints reaction on the suspension tube, we now must find the internal action, through which the stresses are calculated. Shear stress takes three different value: one in the section between *A* and b_1, one between the two bearings and then from b_2 to *B*. These values are

$$T_{xy} = \{Fx_A, \quad Fx_A + Fx_1, \quad -Fx_B\}$$

$$T_{yz} = \{Fz_A, \quad Fz_A + Fz_1, \quad -Fz_B\}$$

$$T = \sqrt{T_{xy}^2 + T_{yz}^2}$$

Table 4.4 reports the results.

Table 4.4 – Shear forces

Shear forces	Front	Front (curve only)	Rear
A to b_1	2765.3 N	3115.3 N	3258.7 N
b_1 to b_2	1188 N	1186.1 N	1519.3 N
b_2 to B	4113.5 N	3448.1 N	3024.1 N

Bending moment, instead, linearly increase from 0 at *A* to b_1, then to b_1 to b_2 and it decrease linearly to *B*. At notch, bearings b_1 and b_2 it is

$$M_{xy} = \{Fx_A \cdot d_n, \quad Fx_A \cdot d_1, \quad Fx_B \cdot (l - d_2)\}$$
$$M_{yz} = \{Fz_A \cdot d_n, \quad Fz_A \cdot d_1, \quad Fz_B \cdot (l - d_2)\}$$

where $d_n = 39.6\ mm$ is the distance between point *A* and notch.

$$M_b = \sqrt{M_{xy}^2 + M_{yz}^2}$$

In *Table 4.5* are shown the bending moments in the considered sections.

Table 4.5 – Bending moments

Bending moment	Front	Front (curve only)	Rear
Notch	109507 Nmm	123367 Nmm	129045 Nmm
Bearing b_1	118356 Nmm	133336 Nmm	160981 Nmm
Bearing b_2	153023 Nmm	128268 Nmm	92538 Nmm

In *Figure 4.11*, *Figure 4.12* and *Figure 4.13* are pictured the plots of the trends of shear and bending for the three load cases.

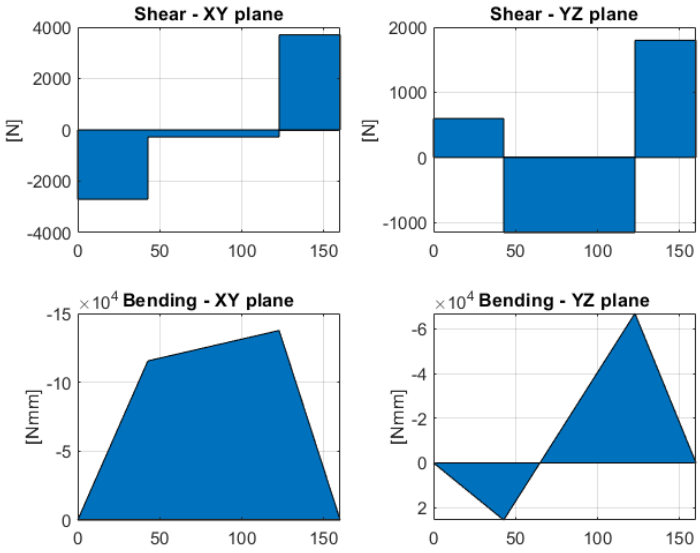

Figure 4.11 – Shear and bending, front tube

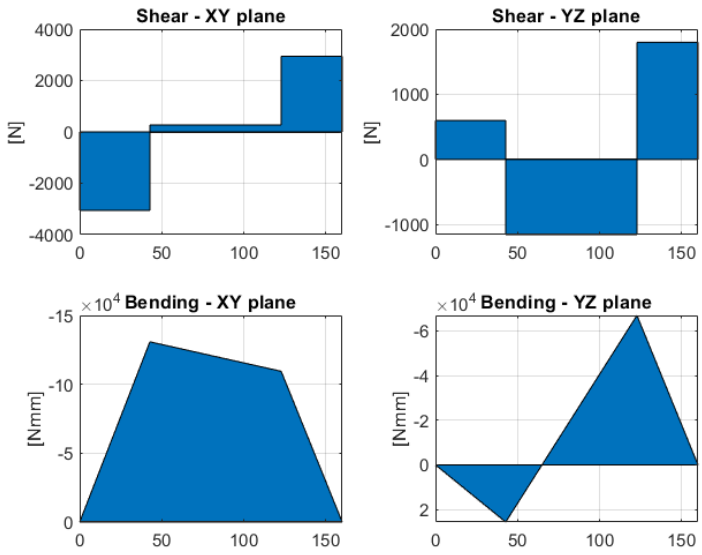

Figure 4.12 – Shear and bending, front tube curve only

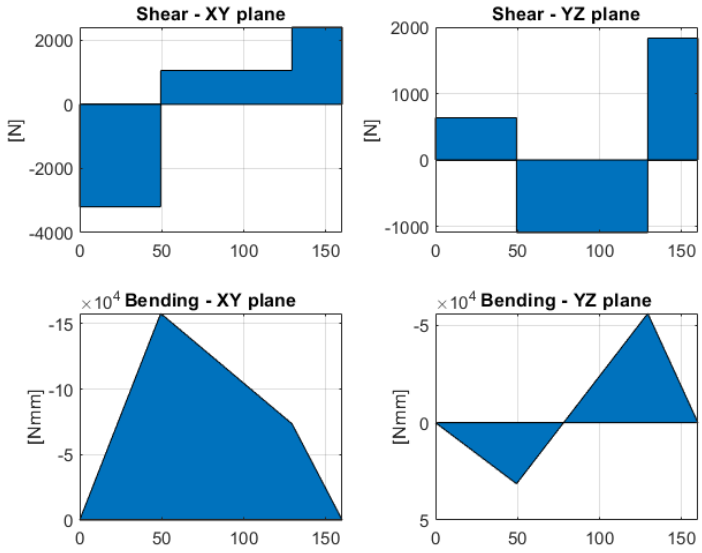

Figure 4.13 – Shear and bending, rear tube

The next step is to calculate bending stresses:

$$\sigma = K_t \frac{M_b \cdot \frac{D_{ext}}{2}}{J}$$

$$J = \frac{\pi}{64}\left(D_{ext}^4 - D_{int}^4\right)$$

where $D_{ext} = 30\ mm$ and $D_{int} = 22\ mm$ are, respectively, the external and internal diameter of the original tubes.

$K_t = 2.76$ is the stress intensity factor to apply at the notch, calculated from Peterson for a solid shaft (since no data was found for a hollow one), with change of diameter and subjected to bending moment [6]. *Table 4.6* shows the result for the original tubes.

Table 4.6 – Stresses of the original tubes

Stress	Front	Front (curve only)	Rear
Notch	160.2 MPa	180.4 MPa	188.8 MPa
Bearing b_1	62.8 MPa	70.8 MPa	85.4 MPa
Bearing b_2	81.2 MPa	68.1 MPa	49.1 MPa

Now the reason to consider also the case of pure curve at the front is evident: due to the transportation moment of F_x that counteract the one of F_y, in case of braking the force on the internal bearing b_1 is smaller, thus the bending moment and stress at the notch, the most stressed region due to the notch effect. This doesn't happen on the rear, since both transportation moment act in the same direction.

Is noticeable from the very high safety coefficient $\eta = \frac{R_{p02}}{\sigma_{MAX}} = \frac{750}{188.8} = 3.97$ that the piece is oversized and, since it's a heavy part of approximately 500 g, has to be resized.

4.3 Sizing of the suspension tubes

In the design phase of the suspension tubes the following constraints are considered:

- Length: defined by the position of the clamps on the chassis;
- External diameter: it's imposed by the internal diameter of the bearings, equal to 30 mm, so it can't be enlarged without change them; reducing it would be possible but counterproductive, since this solution would reduce the moment of inertia of the section;
- Fillet radius at the diameter change: this has to be bigger to reduce the notch effect, and the maximum possible allowed by the bearings is equal to 0.3 mm;
- Shoulder dimensions: length is fixed by the suspension geometry; diameter must be the smaller possible to reduce the notch effect and the minimum value allowed by the bearing is 32 mm.

So, the only variables to work with are the material and the internal diameter.

The material choice is principally based on the value of the strength/density ratio: in order to have the lightest part it must be maximized. Another parameter is the young modulus: it affects toe and camber angle variation which must be small, so a high elastic modulus is preferred.

Possible materials are (properties in *Table 4.7*):

- Steel: very high Young modulus and yield stress, but due to its density, might be difficult to achieve a lightweight component;
- Titanium alloy (Ti-6Al-4V): yield and ultimate stress comparable with the steel's ones, but, being the density almost the half, it is more suitable for the application. The cons of this choice are the high costs of the material and its machining, made difficult by its mechanical properties and the low heat dissipation;

- Aluminium alloy (6061-T6): very light material but presents low resistance properties (less than one third of the previous ones);
- Ergal (Al 7075-T6): particular aluminium alloy that, thanks to the addition of zinc, has high mechanical properties, double than the normal aluminium's ones, probably doing this material the best choice for this application; the only limit could be the low young modulus, virtually the same of the others aluminium alloys.

For the reasons listed, the choice falls on Ergal.

Table 4.7 – Materials' properties

Material	Density	Yield stress	Ultimate stress	Young modulus
Steel	7890 kg/m^3	450 – 800+ MPa	500 – 1000+ MPa	206 GPa
Ti-6Al-4V	4430 kg/m^3	880 MPa	950 MPa	113.8 GPa
Al 6061-T6	2700 kg/m^3	276 MPa	310 MPa	68.9 GPa
Al 7075-T6	2810 kg/m^3	430 – 500 MPa	510 – 540 MPa	71.7 GPa

To minimize the mass, we need to maximize the internal diameter, so its relation to the constraints (failure under design loads (previously defined) and toe and camber variation in case of realistic loads) must be defined.

Imposing $\sigma_{MAX} = \sigma_{yield}$ (safety factor is not needed since loads are overestimated respect the real ones), is possible to find the minimum diameter with the next formulas:

$$J_{min} = K_t \frac{M_b \cdot \frac{D_{ext}}{2}}{\sigma_{yield}}$$

$$D_{int,MAX} = \sqrt[4]{D_{ext}^4 - \frac{64 J_{min}}{\pi}}$$

where $K_t = 2.55$. The formula gives the result of $D_{int,MAX} = 27.55\, mm$. This means that the thickness must be 1.23 mm, such a small value is not acceptable due to manufacturing issues: for this reason the internal diameter is chosen equal to 26 mm (2 mm thick), still bigger than the original of 22 mm. The corresponding stresses are shown in *Table 4.8*. Safety factors were calculated in relation of the lower yield stress for Ergal (430 MPa).

Table 4.8 – Stresses of the new tubes

Stress	Front	Front (curve only)	Rear
Notch	241.6 MPa	272.2 MPa	284.8 MPa
Bearing b_1	102.5 MPa	115.4 MPa	139.3 MPa
Bearing b_2	132.5 MPa	111.0 MPa	80.1 MPa
Safety factor	1.78	1.58	1.51

Table 4.9 reports the mass of the resized tube and the variation with respect to the original one.

Table 4.9 – New tube mass

Mass	100 g
Variation	-410 g
Variation %	-80.4%

4.3.1 Characteristic angles variation

In this section toe and camber angles variations under the effect of the loads in race conditions are evaluated. They are defined as (*Figure 4.14*):

- Toe: identifies the angle between the direction the tires point and the centerline of the vehicle when viewed from directly above: if these are convergent (the two lines intercept in front of the vehicle), it is said toe-in, if they diverges it's called toe-out. There isn't an official sign convention about this angle, so we must consider negative values for toe-in and positive for toe-out;
- Camber: is the tilt of the tires as viewed from the front. Inward tilt is negative, outward tilt is positive.

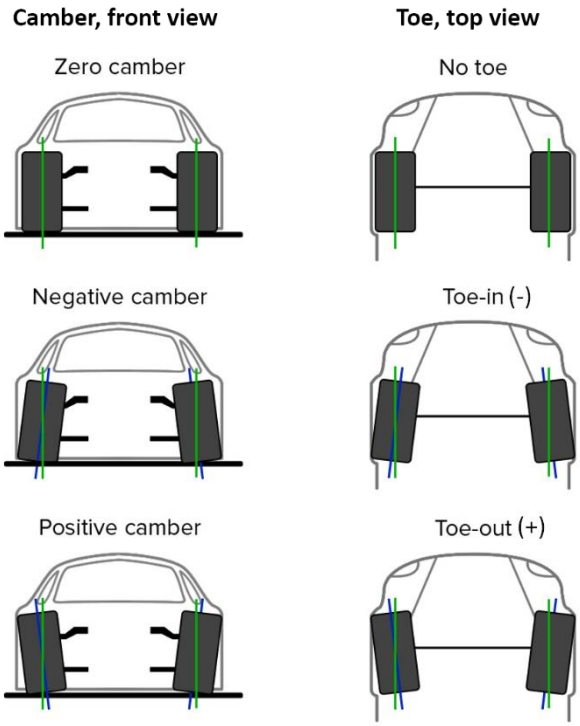

Figure 4.14 – Camber and toe definition

According to tests previously carried out on the tires used, the best configuration in order to minimize the energy consumption is a null value for both angles.

Displacements were calculated by means of the Euler-Bernoulli beam theory [7]. The suspension tube is modelled as a pinned-pinned beam (*Figure 4.15*). Forces are applied at the points where the bearings are located.

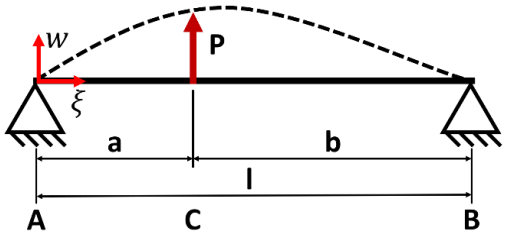

Figure 4.15 – Pinned-pinned beam deflection

$$AC\ (\xi < a): \quad w = \frac{Pb}{6lEJ}\xi^3 + \frac{Pb(l^2 - b^2)}{6lEJ}\xi$$

$$CB\ (\xi > a): \quad w = -\frac{Pb}{6lEJ}\xi^3 + \frac{P(\xi - a)^3}{6EJ} + \frac{Pb(l^2 - b^2)}{6lEJ}\xi$$

Defining dimensions and substituting them in the equations:

$$\begin{cases} F_1: a = d_1 \\ \quad\ b = w - d_1 \\ F_2: a = d_2 \\ \quad\ b = w - d_2 \end{cases}$$

$$w_{1,F_1} = \frac{-F_1(l - d_1)d_1^3 + F_1(l - d_1)(2ld_1 - d_1^2)d_1}{6lEJ}$$

$$w_{1,F_1} = -\frac{F_1(l - d_1)d_2^3}{6lEJ} + \frac{F_1(d_2 - d_1)^3}{6EJ} + \frac{F_1(l - d_1)(2ld_1 - d_1^2)d_2}{6lEJ}$$

$$w_{1,F_2} = \frac{-F_2(l - d_2)d_1^3 + F_2(l - d_2)(2ld_2 - d_2^2)d_1}{6lEJ}$$

$$w_{2,F_2} = \frac{-F_2(l - d_2)d_2^3 + F_2(l - d_2)(2ld_2 - d_2^2)d_2}{6lEJ}$$

where w_{m,F_n} means the deflection w at the bearing m due to the force at the bearing n.

The total deflection is then calculated as superimposition of the action due to both forces on XY and YZ planes:

$$\Delta x_1 = w_{1,Fx_1} + w_{1,Fx_2}$$

$$\Delta x_2 = w_{2,Fx_1} + w_{2,Fx_2}$$

$$\Delta z_1 = w_{1,Fz_1} + w_{1,Fz_2}$$

$$\Delta z_2 = w_{2,Fz_1} + w_{2,Fz_2}$$

From displacements is possible to calculate the variation of the angles with a simple geometry consideration, shown in *Figure 4.16*.

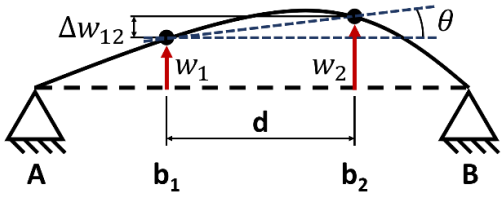

Figure 4.16 – Relation between displacements and angle

$$\tan\theta = \frac{w_2 - w_1}{d} = \frac{\Delta w_{12}}{d}$$

$d = d_2 - d_1 = 80\ mm$ is the distance between the bearing, equal for front and rear tubes.

Specifically, to define camber and toe:

$$\Delta toe_{front} = \tan^{-1}\frac{\Delta x_{12,front}}{d}, \qquad \Delta \text{camber}_{\text{front}} = \tan^{-1}\frac{-\Delta z_{12,front}}{d}$$

$$\Delta toe_{rear} = \tan^{-1}\frac{-\Delta x_{12,rear}}{d}, \qquad \Delta camber_{rear} = \tan^{-1}\frac{-\Delta z_{12,rear}}{d}$$

Results are shown in *Figure 4.17* and *Figure 4.18*, in *Table 4.10* and *Table 4.11* are reported the correspondent value in thousandths of degree. In the plots are represented in black the actual displacements of the new tubes while in red is highlighted the variation between the results obtained for new and original components.

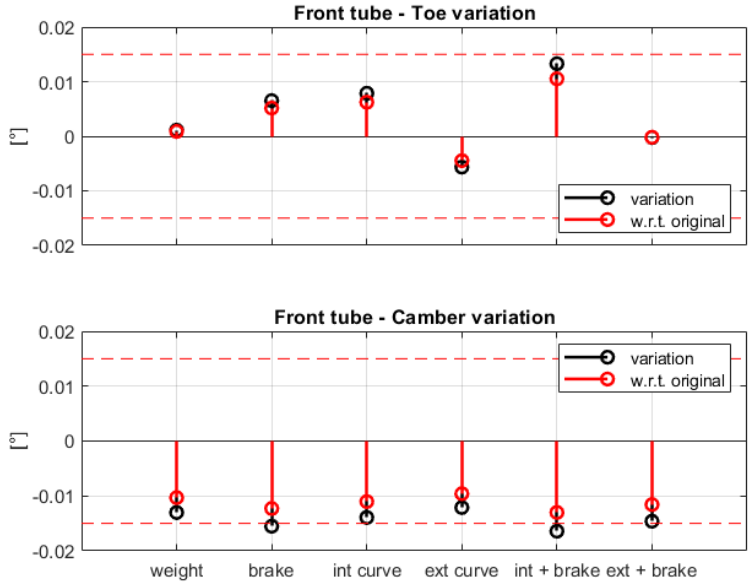

Figure 4.17 – Front tube angles variation

Table 4.10 – Front tube angles variation in 1e-3°

[1e-3°]	weight	braking	Internal curve	External curve	Int curve + braking	Ext curve + braking
Toe	1.1	6.5	7.9	-5.7	13.3	-0.24
Toe variation	0.88	5.2	6.2	-4.5	10.5	-0.19
Camber	-13.0	-15.5	-13.9	-12.1	-16.4	-14.6
Camber variation	-10.3	-12.3	-11.0	-9.6	-13.0	-11.6

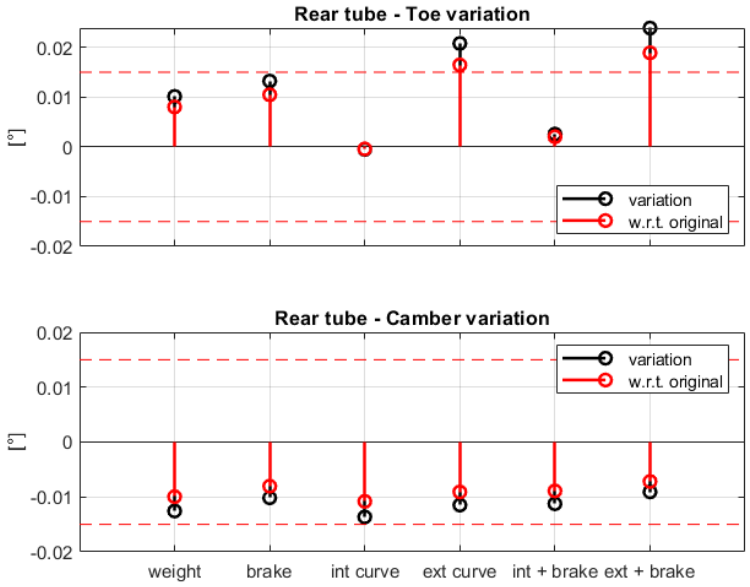

Figure 4.18 – Rear tube angles variation

Table 4.11 – Rear tube angles variation in 1e-3°

[1e-3°]	weight	braking	Internal curve	External curve	Int curve + braking	Ext curve + braking
Toe	10.1	13.2	-0.52	20.8	2.6	23.9
Toe variation	8.0	10.5	-0.41	16.4	2.0	18.9
Camber	-12.7	-10.2	-13.6	-11.5	-11.2	-9.1
Camber variation	-9.9	-8.0	-10.8	-9.1	-8.9	-7.2

Variations of the toe under the weight is mainly due to the action of the rubber bumper in the horizontal direction.

Values of toe and camber variation are very small (0.015° - 0.02° for external curve), but, since the hypothesis of model the claps as hinge is not perfect, thus in reality the system is more rigid, these angles would actually be smaller.

4.4 Clamp and bearing pressure

To complete the failure resistance in necessary to evaluate the stresses due to the bolted coupling, so the rise of tightening pressure in correspondence of the clamps, and the pressure exerted by the bearings.

The force exerted by the clamps must sustain the lateral force, equal to the design one $F_y = 400\ N$, hypnotizing to apply it on one clamp only.

The generation of the contact pressure in a bolted coupling is obtained by preloaded bolts. The fitting pressure acts evenly along the length and in plane, but it does not on the contact surface [5], as shown in *Figure 4.19*.:

$$p(\alpha) = p_{MAX}\sin(\alpha)$$

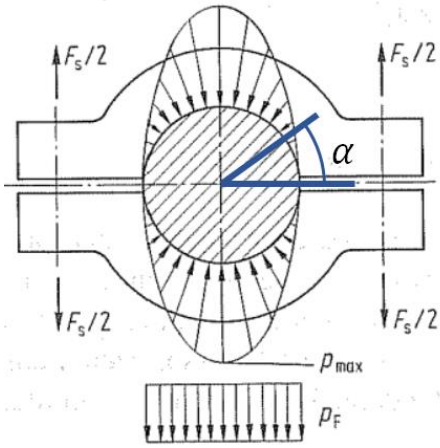

Figure 4.19 – Pressure distribution in a bolted coupling

From the vertical equilibrium of half of the fitting you get

$$F_s = \int_0^{\pi} p(\alpha)\cdot L\cdot\frac{D}{2}\cdot d\alpha\cdot\sin\alpha = p_{MAX}\cdot L\cdot\frac{D}{2}\cdot\int_0^{\pi}\sin^2\alpha\, d\alpha = \frac{\pi}{4}p_{MAX}\cdot L\cdot D$$

$$p_{MAX} = \frac{4F_s}{\pi LD}$$

where $L = 28\ mm$ is the contact length, D the external diameter of the tube and F_s the tightening force of the clamp. So, the transmissible force is:

$$F_{y,MAX} = 2\int_0^{\pi}\tau(\alpha)\cdot L\frac{D}{2}d\alpha = 2\int_0^{\pi}\mu\cdot p(\alpha)\cdot L\frac{D}{2}d\alpha = \frac{4\mu F_s}{\pi}$$

The friction coefficient μ for aluminium-aluminium contact is equal to 0.2, giving the result of 1570 N of minimum tightening force (785 N for each bolt) required to sustain the lateral force.

To verify the resistance of the tube in correspondence of the contacts, both for clamps and bearings, also the contribution of the forces is included: it has been hypothesized as a sinusoidal contact pressure, the same of the bolted coupling, but acting in the side in compression only: the maximum pressure is then calculated as $p_{MAX} = 4F_c/\pi LD$, where $F_c = \sqrt{F_x^2 + F_z^2}$ is the force exerted by the clamp or the bearing considered.

For the clamps the maximum contact pressure is calculated as the sum of the one due to the tightening and the one due to the reaction force, also if they are not actually allocated in the same point, in favour of safe. The tightening pressure is calculated for clamping force of 10000 N.

The contact pressure obtained are reported in *Table 4.12*.

Table 4.12 – Contact pressures

	Clamp A	Bearing 1	Bearing 2	Clamp B
Front	19.61 MPa	19.84 MPa	32.84 MPa	20.60 MPa
Front (curve only)	19.88 MPa	24.93 MPa	26.42 MPa	20.38 MPa
Rear	20.10 MPa	30.43 MPa	21.39 MPa	19.74 MPa

For the evaluation of radial and circumferential stresses was used the same formula of the interference fit, considering a constant pressure applied around the tube equal to the maximum one:

$$\begin{cases} \sigma_r = -p_{MAX} \\ \sigma_\theta = -p_{MAX}\left(\dfrac{a^2+1}{a^2-1}\right) \end{cases}$$

where $a = \frac{D_{ext}}{D_{int}}$.

The total stress is obtained by means of the Von-Mises formula for multi-axial stress:

$$\sigma_{VM} = \sqrt{(\sigma_r - \sigma_\theta)^2 + (\sigma_r - \sigma_{ax})^2 + (\sigma_{ax} - \sigma_\theta)^2}$$

where axial stress is due to the bending and is positive (tensile stress) for the clamps, while it's negative (compression stress) for the bearings, since the force act on the compressed side. In *Table 4.13* we can see the results.

Table 4.13 – Von-Mises stresses

	Clamp A	Bearing 1	Bearing 2	Clamp B
Front	196.5 MPa	218.3 MPa	172.5 MPa	165.9 MPa
Front (curve only)	202.9 MPa	229.1 MPa	138.2 MPa	163.3 MPa
Rear	208.0 MPa	160.0 MPa	111.9 MPa	155.2 MPa

All the stresses are much smaller than the yield stress of the material, so the failure resistance for the contact is verified.

4.5 Finite elements analysis

In this section the tubes are analysed with the *Finite Element Method* (*FEM*). For the front one only the case of pure curve was considered, since the most stressed.

4.5.1 Creation of the model

The part has been created as 3D solid deformable instance, obtained by revolution. It was then partitioned with planes normal to the axis of the tube (*Figure 4.20* and *Figure 4.21*) to define the position of:

- Clamps: one for each end, for a length of 28 mm
- Bearings: the contact length is equal to the width of the bearing (7 mm) minus the two fillets radius on the internal radius (0.3 mm each). Both partitions were then split again by two radial planes to define the half part in compression, on which the load is applied.

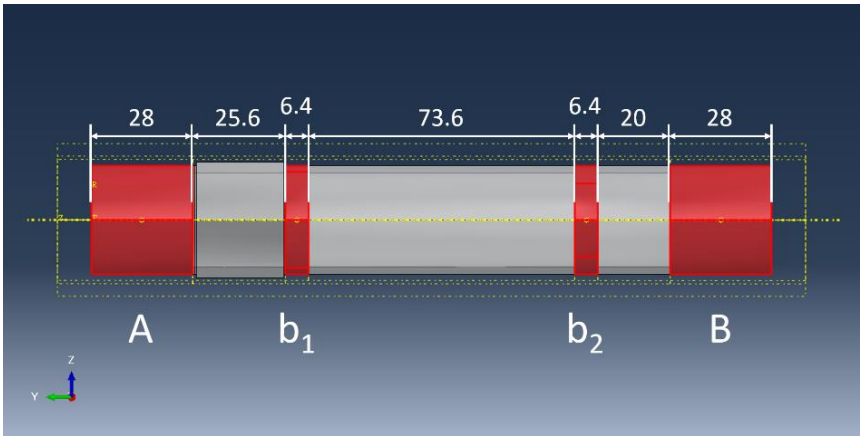

Figure 4.20 – Front tube partition

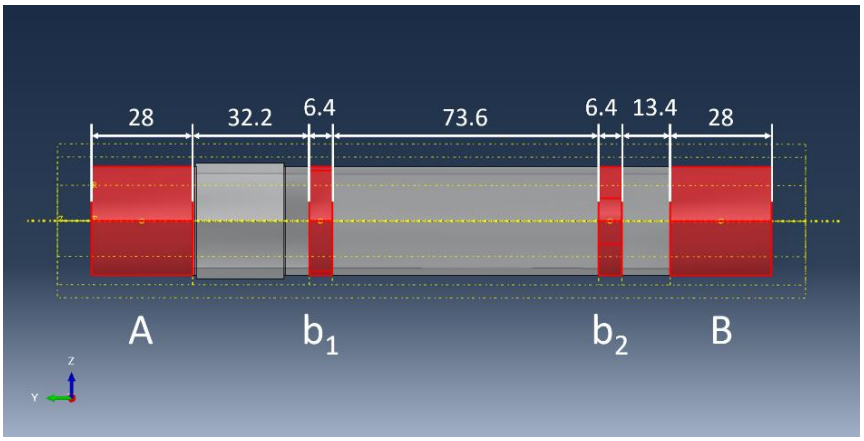

Figure 4.21 – Rear tube partition

One difference between front and rear tubes is the position of the bearings: while on front b_1 is directly lean on the shoulder, at rear is moved 6.6 mm from a spacer; bearing-bearing distance is instead, as already said, equal in both cases.

Forces acting on all bearing are different, not only in form, but also direction: for each one was defined a different radial plane, perpendicular to their direction of application, calculated as

$$\theta_F = \arg(F_z + iF_x)$$

that gives the value of the angle respect the Z axis. This calculation was done as *complex number argument* and not *arctangent* since the second returns only values between ±90°. In *Table 4.14* these values are presented.

Table 4.14 – Bearings' forces application direction

Bearing	Front (curve)	Rear
b_1	117.8°	112.1°
b_2	42.2°	24.7°

The material has been modelled as isotropic elastic with a Young modulus of 70000 MPa and Poisson equal to 0.33; it was then applied to the part as a solid homogeneous section.

In the *interaction* section two reference points were created, one for each clamp, on the tube axis and 14 mm from each end, in the middle of the contact length, were hinges has been positioned. They were then connected with a kinematic coupling for all degrees of freedom, as shown in *Figure 4.22*.

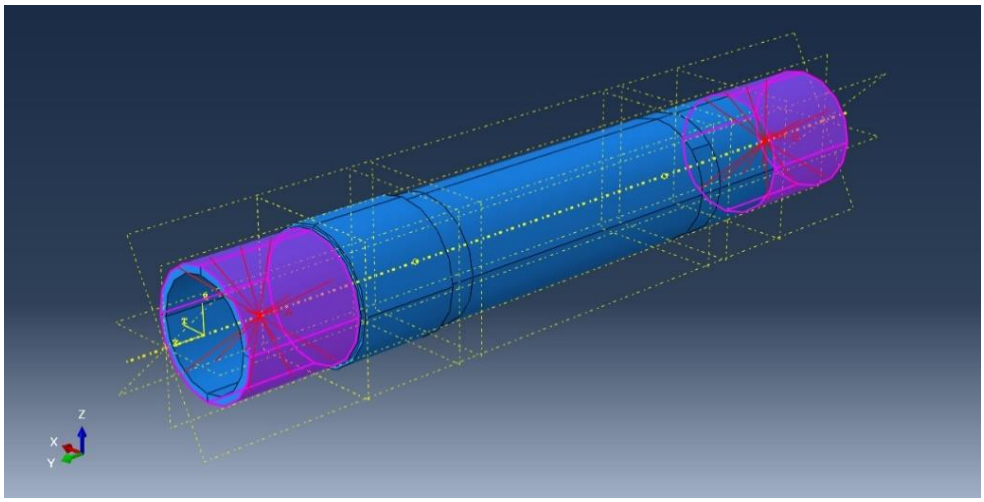

Figure 4.22 – Coupling of the clamps

To create the pins, displacements of the two reference points were constrained and, to avoid lability, was also necessary to lock the rotation around the axis of the tube.

Since the axial force is transmitted by the bearing b_1 to the tube shoulder, on its lateral surface a pressure with a total force of 400 N was applied (*Figure 4.23*).

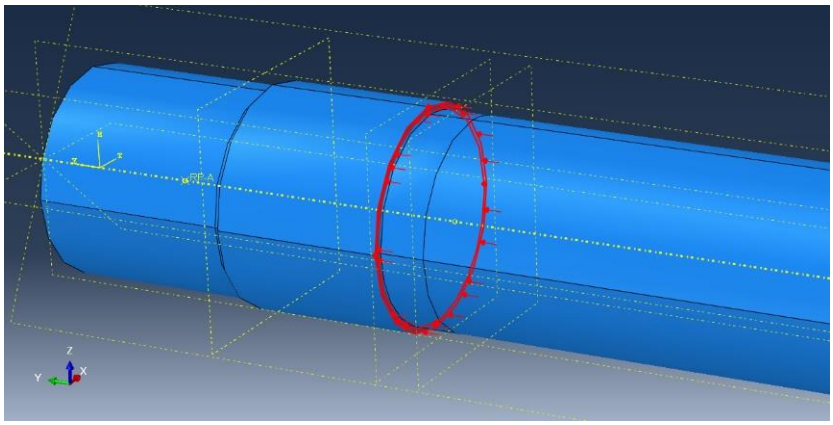

Figure 4.23 – Axial load

The force transmitted by the two bearing was applied as a pressure characterized by a sinusoidal distribution, defined as

$$-p_{MAX} \cdot \sin(\theta - \theta_F)$$

where p_{MAX} is the maximum contact pressure calculated in chapter *4.4*, θ the angle respect the Z axis and θ_F the angle of application of the force (*Table 4.14*). The pressure was applied on the compressed side. In *Figure 4.24* is pictured the load case of the front tube.

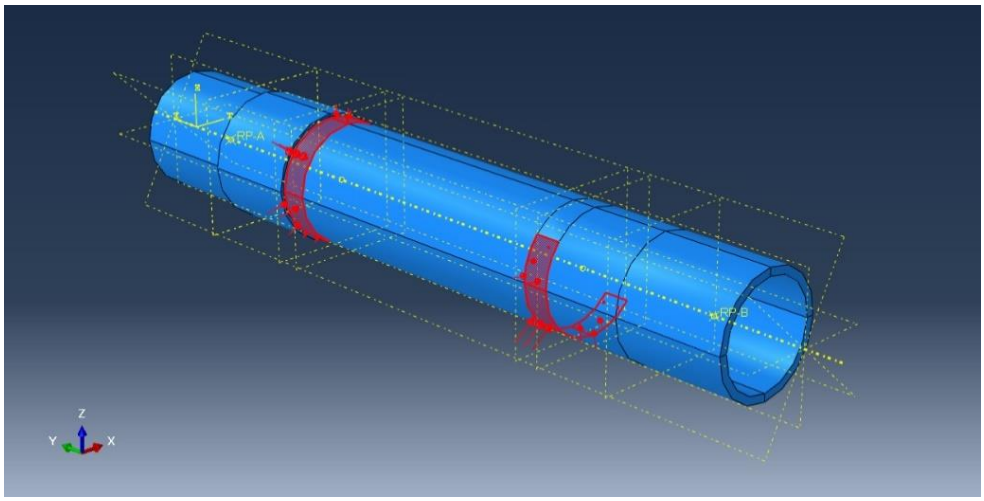

Figure 4.24 – Bearing loads, front tube

The simple shape of the axle allows the use of the hexahedral mesh but, to improve its quality nearby the fillet without increase too much the total number of elements, it was preferred to use the free tetrahedral mesh with quadratic geometric order (C3D10): in this way was possible to use a coarse mesh for the whole model, refining it with very small elements in the most stressed region, the fillet of the shoulder (*Figure 4.25* and *Figure 4.26*), to obtain a better estimation of stresses; to do this *tri-meshing mapping* option in *mesh control* was disabled.

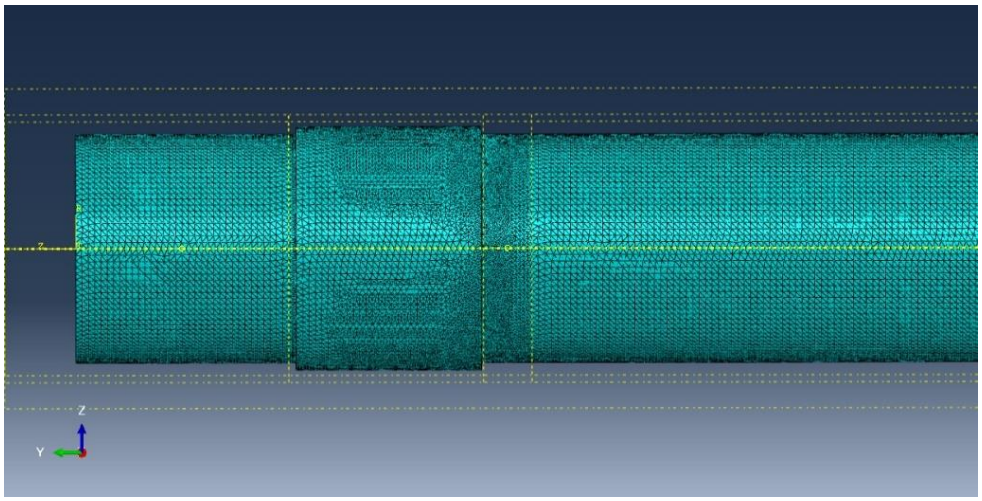

Figure 4.25 – Meshed tube

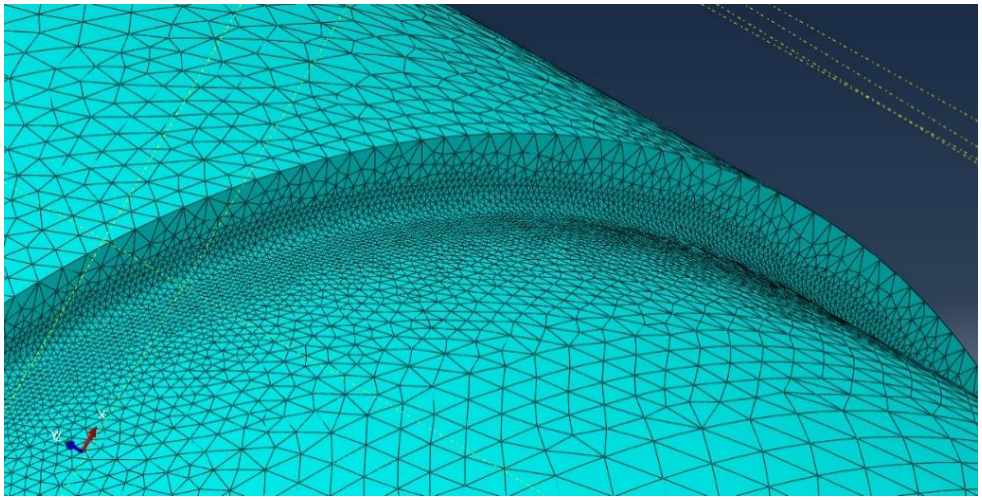

Figure 4.26 – Detail of the mesh refinement on the fillet

To accomplish a correct evaluation of the stresses avoiding computational errors, the local seed chosen was smaller than the fillet radius (0.3 mm) and to verify the convergence of the results, the analysis was run with different values of local seed: 0.25 mm, 0.1 mm and 0.05 mm.

4.5.2 FEM results

The data was extrapolated using a circular path was created in correspondence of the fillet, as shown in *Figure 4.27* (highlighted in red).

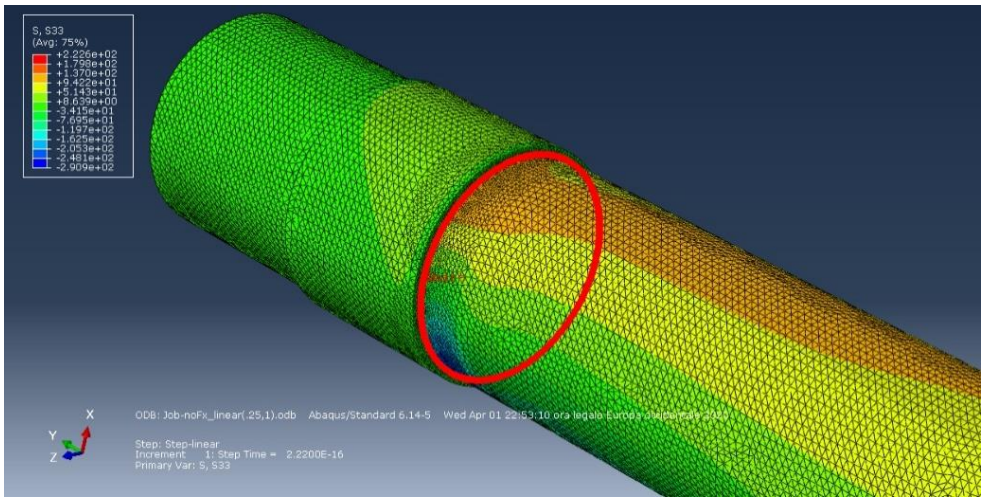

Figure 4.27 – Circular path

To compare FEM and analytical results, axial stress was considered; values taken on the defined path are reported in *Figure 4.28* and *Table 4.15*.

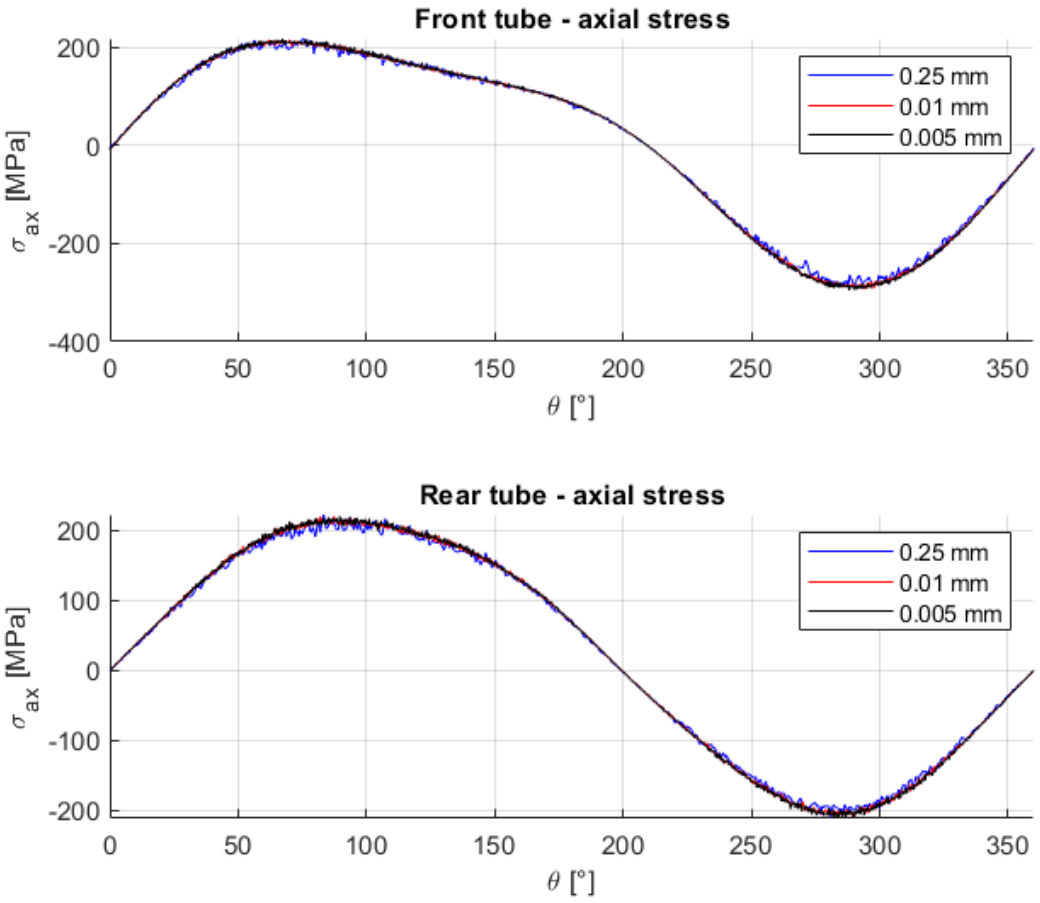

Figure 4.28 – Axial stress graphs

Table 4.15 – Axial stress, maximum values

Mesh size	Front tube	Rear tube
0.25 mm	218.5 MPa	223.1 MPa
0.10 mm	216.0 MPa	221.3 MPa
0.05 mm	218.1 MPa	221.0 MPa

As you can see from graphs and values, the results are convergent, so the data provided is reliable.

Anyway, values found are smaller than the expected from analytic calculation: this can be caused by the choice of the Peterson's coefficient for a solid shaft. To evaluate the correct K_t we use the formula

$$K_t = \frac{\sigma}{\sigma_{nom}}$$

$$\sigma_{nom} = \frac{M_{b,notch} \cdot \frac{D_{ext}}{2}}{J}$$

In *Table 4.16* are reported stresses and the coefficient calculated.

Table 4.16 – K_t evaluation

	Nominal stress	Actual stress	K_t
Front tube	106.8 MPa	218 MPa	2.04
Rear tube	111.7 MPa	222 MPa	1.99

5 Design of the wheel hubs

In this chapter the design process of the wheel hubs components is presented, in particular:

- Front axle: the part is designed as a hollow axle made from steel
- Front and rear hubs: the parts are designed with the aid of topology and shape optimization process.

Figure 5.1 pictures the front hub.

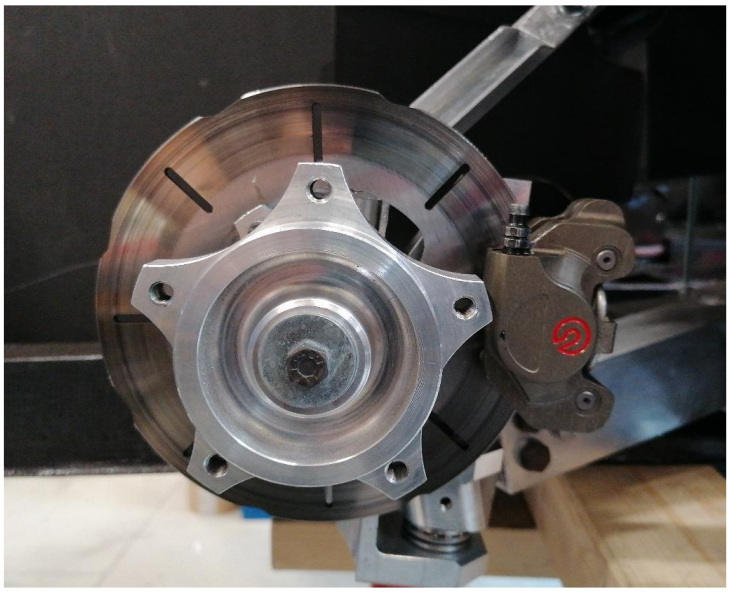

Figure 5.1 – Photo of the front hub

5.1 Hubs components

Front and rear hubs are composed by two elements each, the aluminium hub and the steel axle, shrink-fitted together. The main difference of the front and rear hub is the position of the brake disc: at front it is mounted directly on the hub, while on the rear, to allow the positioning of the drivetrain, it is mounted on the axle, on the opposite side with respect to the hub-carrier.

Figure 5.2 and *Figure 5.3* show the layout of front and rear hub respectively and their mounting in the hub-carrier, in *Table 5.1* and *Table 5.2* main components are listed.

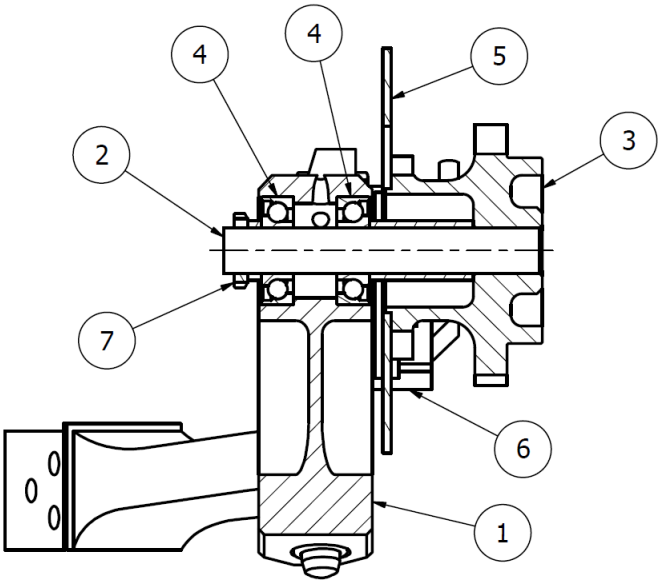

Figure 5.2 – Front hub and hub-carrier

Table 5.1 – Main components, front

1	Hub-carrier
2	Axle
3	Hub
4	Angular contact bearings
5	Brake disc
6	Brake pad
7	Locknut

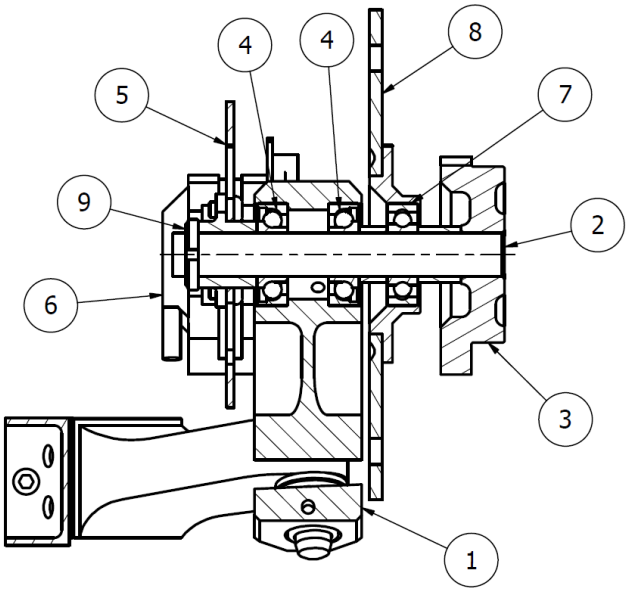

Figure 5.3 – Rear hub and hub-carrier

Table 5.2 – Main components, rear

1	Hub-carrier
2	Axle
3	Hub
4	Angular contact bearings
5	Brake disc
6	Brake pad
7	Freewheel
8	Driven gear
9	Locknut

In *Table 5.3* and *Table 5.4* are reported hubs and their material properties.

Table 5.3 – Hubs materials and mass

Part	Material	Mass
Front axle	Steel 39NiCrMo4	209 g
Rear axle	Steel 39NiCrMo4	228 g
Front hub	Aluminium 6061-T6	333 g
Rear hub	Aluminium 6061-T6	216 g

Table 5.4 – Material properties

Material	Density	Yield stress	Ultimate stress	Young modulus
Steel 39NiCrMo4	7890 kg/m^3	835 MPa	1000 MPa	206 GPa
Aluminium 6061-T6	2700 kg/m^3	240 MPa	260 MPa	68.9 GPa

5.2 Front Axle

Despite the small size, since it is a solid axle steel-made, it is quite heavy (209 g). This part is re-designed in a simple way as done for the suspension tubes: external diameter it's imposed by the bearings of the hub carrier and length is fixed.

The material was not changed to avoid big deformation, so toe and camber variation, since aluminium's young modulus is one third of the steel's one. In order to reduce weight, the axle was holed, according to maximum stress under design loads and maximum deflection in race conditions.

The system is schematized as a one-dimensional beam, supported by two hinges in correspondence of the bearings, while on the free end are applied forces and moments coming from the hub (*Figure 5.4* and *Figure 5.5*). Dimensions are reported in *Table 5.5*.

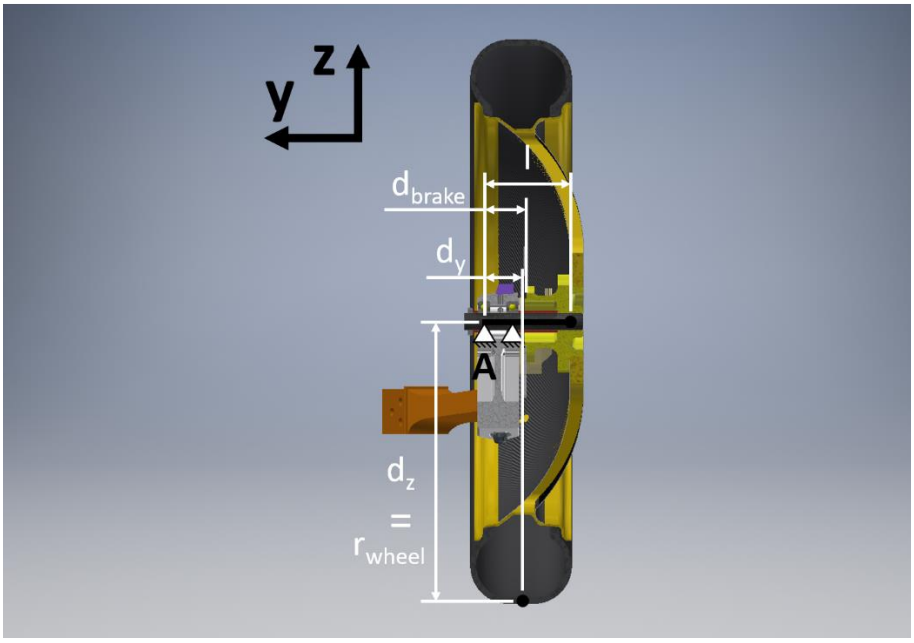

Figure 5.4 – Axle and wheel scheme

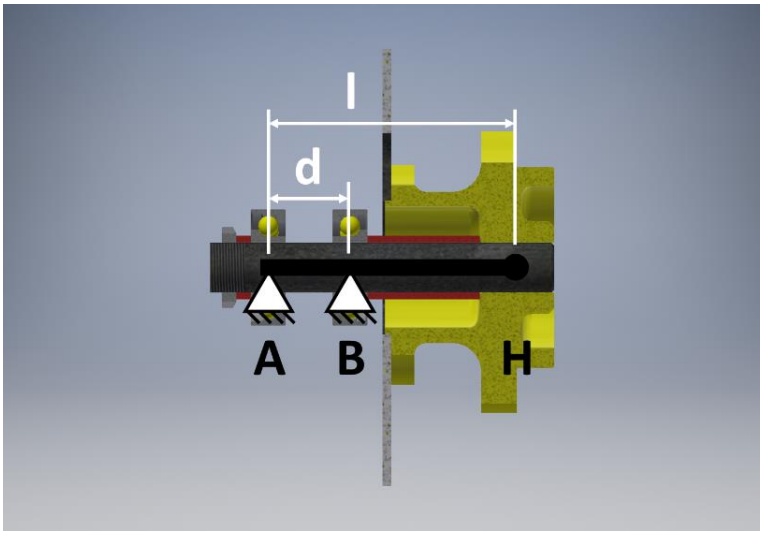

Figure 5.5 – Axle scheme

Table 5.5 – Axle dimensions

d_y	39 mm
$d_z = r_{wheel}$	279 mm
l	85 mm
d_{brake}	40.5 mm
d	28 mm

It is first necessary to transport the forces coming from the contact with the road to the hub, to apply them as concentrated forces and moments at the free-end of the axle (*Figure 5.6*).

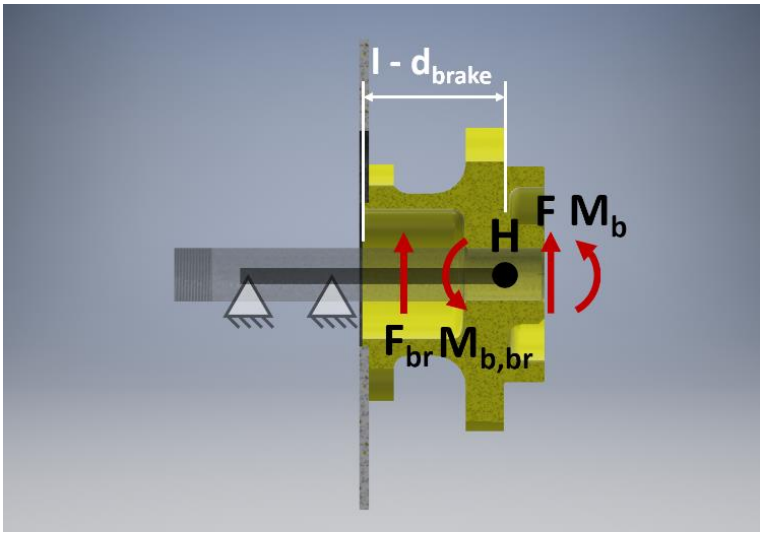

Figure 5.6 – Hub forces

The braking torque is not transmitted to the axle since the brake disc in directly mounted on the hub and, due to the eccentricity of the brake pad, there is a generated force (*Figure 5.7*) that established a bending moment that must be taken into account, adding their contribution in correspondence of the free-end of the axle (*Figure 5.6*).

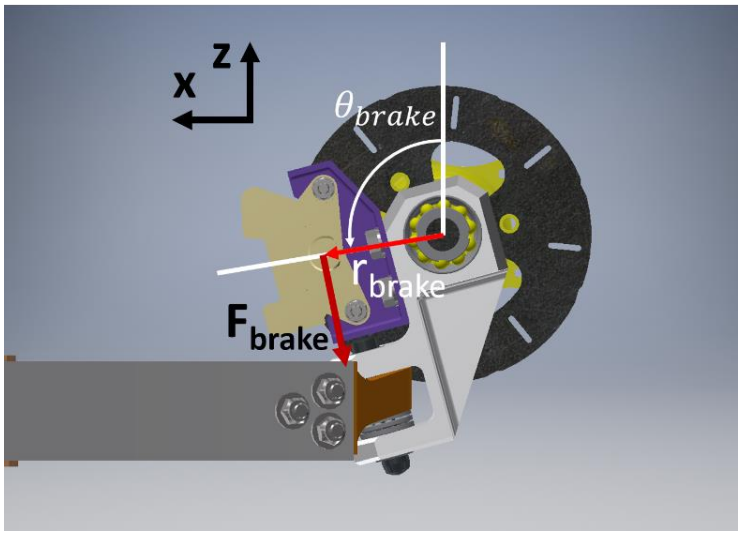

Figure 5.7 – Brake force

To calculate F_{brake} and its decomposition along the X and Z axis we proceed as follow:

$$F_{brake} = F_x \cdot \frac{r_{wheel}}{r_{brake}}$$

$$\begin{cases} Fx_{brake} = F_{brake} \cdot \cos\theta_{brake} \\ Fz_{brake} = -F_{brake} \cdot \sin\theta_{brake} \end{cases}$$

where $r_{brake} = 75.8\,mm$ is the distance of the brake pad from the axle and $\theta_{brake} = 99.4°$ the angle respect the vertical axis of its position along the brake.

Now it is possible to calculate the forces and moment transported to the hub:

$$\begin{cases} Fx_H = F_x + Fx_{brake} \\ Fy_H = F_y \\ Fz_H = F_z + Fz_{brake} \\ Mx_H = Fz_H \cdot l + F_y \cdot d_z - F_z \cdot d_y - Fz_{brake} \cdot d_{brake} \\ My_H = 0 \quad (no\ torque\ transmitted) \\ Mz_H = -Fx_H \cdot l + F_x \cdot d_y + Fx_{brake} \cdot d_{brake} \end{cases}$$

And to find the reaction forces exerted by the bearings the equations are:

XY plane:

$$\begin{matrix} Equilibrium\ along\ X: \\ Moment\ equlibrium\ around\ A: \end{matrix} \begin{cases} Fx_A + Fx_B + Fx_H = 0 \\ Fx_B \cdot d + Fx_H \cdot l + Mz_H = 0 \end{cases}$$

YZ plane:

$$\begin{matrix} Equilibrium\ along\ Z: \\ Moment\ equlibrium\ around\ A: \end{matrix} \begin{cases} Fz_A + Fz_B + Fz_H = 0 \\ -Fz_B \cdot d - Fz_H \cdot l + Mx_H = 0 \end{cases}$$

In matrix form

$$\begin{bmatrix} 1 & 1 \\ 0 & d \end{bmatrix} \begin{Bmatrix} Fx_A \\ Fx_B \end{Bmatrix} = \begin{Bmatrix} -Fx_H \\ -Fx_H \cdot l - Mz_H \end{Bmatrix}$$

$$\begin{bmatrix} 1 & 1 \\ 0 & d \end{bmatrix} \begin{Bmatrix} Fz_A \\ Fz_B \end{Bmatrix} = \begin{Bmatrix} -Fz_H \\ -Fz_H \cdot l + Mx_H \end{Bmatrix}$$

About the force along Y, the same considerations previously done for the suspension tubes and shown in *Figure 4.9*, therefore, since F_y is directed inward, $Fy_A = 0$ and $Fy_B = F_y$.

Table 5.6 shows the results.

Table 5.6 – Forces on the front axle

Forces	Braking	No braking
F_x	400 N	0
F_y	400 N	400 N
F_z	1200 N	1200 N
Brake forces		
Fx_{brake}	-239.4 N	0
Fz_{brake}	-1453.7 N	0
Resultants on the hub		
Fx_H	160.6 N	0
Fy_H	400 N	400 N
Fz_H	-253.7 N	1200 N
Mx_H	102111 Nmm	166800 Nmm
My_H	0	0
Mz_H	-7749 Nmm	0
Constraint reactions of the bearings		
Fx_A	50.28 N	0
Fy_A	0	0
Fz_A	-4163.3 N	-3514.1 N
Fx_B	-210.9 N	0
Fy_B	400 N	400 N
Fz_B	4417.0 N	2314.3 N

Shear forces presents two different values: one constant between the bearings and the other one from bearing *B* to the hub:

$$T_{xy} = \{Fx_A\,, \quad -Fx_H\}$$
$$T_{yz} = \{Fz_A\,, \quad -Fz_H\}$$

The bending moment is null in correspondence of the bearing *A*, then increases linearly to *B* and then it goes linearly to the value assumed at the hub:

$$M_{xy} = \{Fx_A \cdot d\,, \quad -Mx_H\}$$
$$M_{yz} = \{Fz_A \cdot d\,, \quad Mz_H\}$$

In *Figure 5.8* and *Figure 5.9* are plotted the trends of the internal action in case of braking and pure curve respectively.

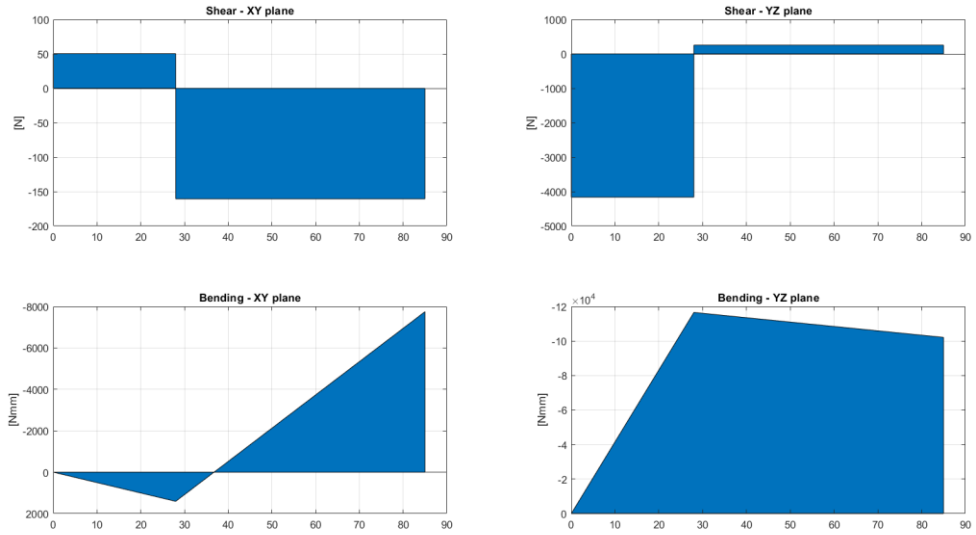

Figure 5.8 – Shear and bending plots, braking case

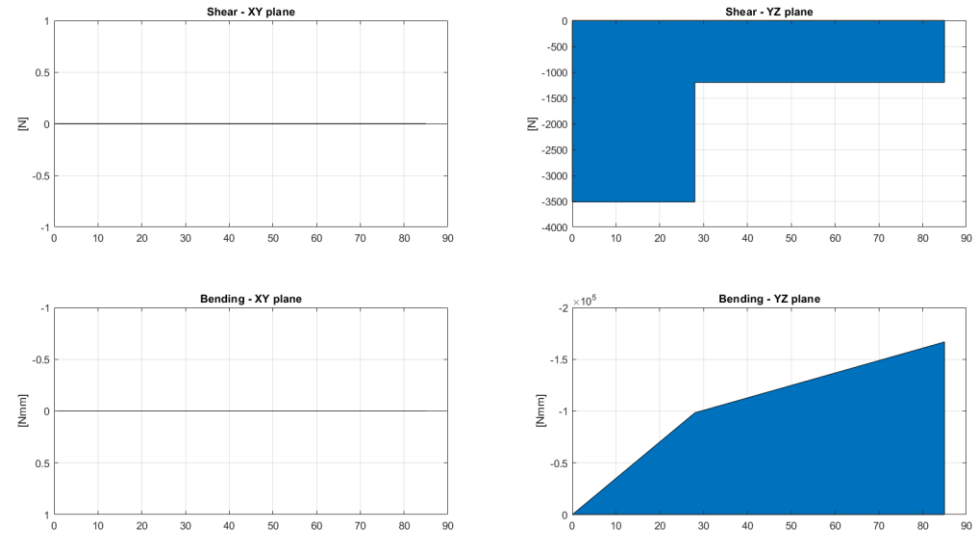

Figure 5.9 – Shear and bending plots, NO braking case

The absolute value of shear and bending internal forces are obviously:

$$T = \sqrt{T_{xy}^2 + T_{yz}^2}\,, \qquad M_b = \sqrt{M_{xy}^2 + M_{yz}^2}$$

And the relative results, for both cases, are shown in *Table 5.7*.

Table 5.7 – Shear and bending internal forces

Braking case		
T [N]	4163.6	300.3
M_b [Nmm]	116580	102404
NO braking case		
T [N]	3514.3	1200
M_b [Nmm]	98400	166800

You can see how the maximum bending moment not only different values from one case has to the other, but also its allocation is different: with braking the maximum is reached in correspondence of the bearing *B*, while without it is bigger and in correspondence of the hub.

5.2.1 Optimization of the internal diameter

The sizing of the internal diameter was done following the same concept used for the suspension tubes. We first need to calculate the maximum possible diameter able to resist to the stresses, with the same formulas already used. For the sake of simplicity, they are below reported:

$$J_{min} = K_t \frac{M_b \cdot \frac{D_{ext}}{2}}{\sigma_{yield}}$$

$$D_{int,MAX} = \sqrt[4]{D_{ext}^4 - \frac{64 J_{min}}{\pi}}$$

As found in the previous section, the maximum bending moment is the one in correspondence of the hub in the case of pure curve, with a value of 166800 Nmm (*Table 5.7*).Being the external diameter $D_{ext} = 17\ mm$ and $\sigma_{yield} = 850\ MPa$, the maximum allowed internal diameter is 14.9 mm, for which corresponds a mass of 49 g.

Axle must also satisfy the constraints on the maximum allowable variation of the wheel angles: to compute the deformation once again we apply the Euler-Bernoulli beam theory, the system is divided into two simpler ones, then the superimposition of the effect is applied to find the solution.

The original scheme of the axle can be decomposed into a pinned-pinned beam (*A*) for the section between the bearings and a cantilever beam (*B*) for the free end (the encastre simulate the continuity of the beam).

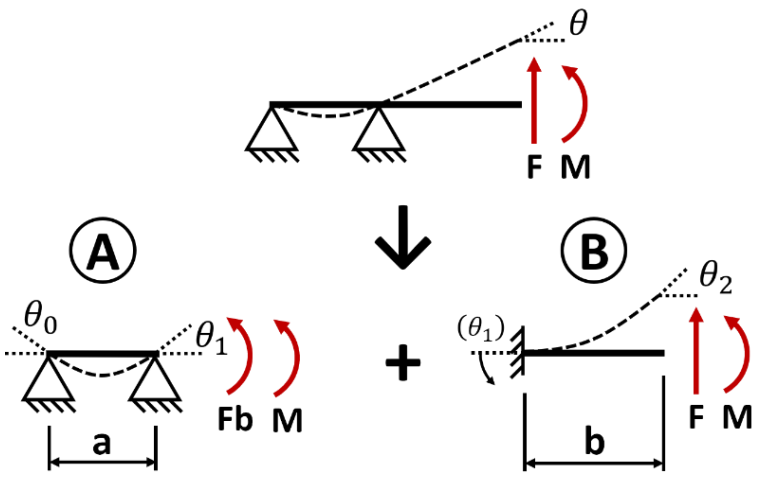

Figure 5.10 – Partition of the beam in two elementary subsystems

System A:

$$\theta_0 = \frac{a}{6EJ}(Fb + M)$$

$$\theta_1 = \frac{a}{3EJ}(Fb + M)$$

System B:

$$\theta_{2,M} = \frac{Ml}{EJ}$$

$$\theta_{2,F} = \frac{Fb^2}{2EJ}$$

$$\theta_2 = \theta_{2,F} + \theta_{2,M}$$

Solution:

$$\theta = \theta_1 + \theta_2$$

The solution equation represents the system *B* in which the encastre has been rotated by an angle equal to the rotation at the support bearing *B* in the system *A*, since in the real part in that section there's no relative rotation. From these equations is finally possible to predict toe and camber angles variation due to the axle deformation.

In order to assess the maximum deformation of the axle, applied loads are those in race condition (see *Table 3.4*).

In *Table 5.8* are shown, in thousandths of degree, the results for the original solid axle.

Table 5.8 – Angles variation for the original axle (thousandths of degree)

[1e-3°]	weight	braking	Internal curve	External curve	Int curve + braking	Ext curve + braking
Toe	0	11.6	0	0	11.6	11.6
Camber	68.4	-14.0	-96.7	233.4	-179.0	151.0

Table 5.9 reports the results related to an internal diameter of 14.9 mm: values of camber and toe angles and their variation with respect to the original case are reported.

Table 5.9 – Angles variation for the maximum inner diameter (thousandths of degree)

[1e-3°]	weight	braking	Internal curve	External curve	Int curve + braking	Ext curve + braking
Toe	0	28.4	0	0	28.4	28.4
Toe variation	0	16.7	0	0	16.7	16.7
Camber	166.8	-34.1	-235.8	569.4	-436.7	368.5
Camber variation	98.4	-20.1	-139.2	336.0	-257.7	217.5

As you can notice, the variation with respects to the original design is too excessive to be acceptable, being the worst case is the camber of the outer wheel which is 0.57°, 0.37° bigger than the corresponding for the original axle.

This means that the internal diameter must be decreased to comply with acceptable angle variations: the *Optimization Toolbox* for *Matlab* is used to solve the constrained optimization problem. The *fmincon* function is exploited in order to find the optimal value of the internal diameter.

First of all is necessary to write an objective function linked to the variable of our interest [8] [9], so the internal diameter: this function is minimized in compliance with the boundary that are later illustrated. Being the aim to reduce the weight, the objective function must be related to the mass, which is equal to:

$$m = \rho_{steel} \cdot l_{axle} \cdot \frac{\pi}{4}\left(D_{ext}^2 - D_{int}^2\right)$$

Since minimize the mass means maximize the internal diameter, our objective function is simply the reciprocal of it:

$$f_{obj}(D_{int}) = \frac{1}{D_{int}}$$

Upper and lower boundaries of the diameter are 14.9 mm (not bigger than the allowed one) and 0 (negative values are obviously not acceptable):

$$0 \leq D_{int} \leq 14.9\, mm$$

Constraints, shown in *Table 5.10*, are defined as maximum characteristic angles variations with respect to the base case.

They were included in the optimization as a non-linear function that returns the maximum difference between the angle variation and the boundaries: if the solution in bigger than zero, this

means that the constrain is not satisfied (according to the *fmincon* function), so the corresponding diameter is not acceptable.

Table 5.10 – Angle boundaries (min ÷ max)

[1e-3°]	weight	braking	Internal curve	External curve	Int curve + braking	Ext curve + braking
Toe	-5 ÷ +5	-50 ÷ 50	-10 ÷ 10	-10 ÷ 10	-50 ÷ 50	-50 ÷ 50
Camber	-10 ÷ 10	-50 ÷ 50	-30 ÷ 100	-100 ÷ 30	-50 ÷ 100	-100 ÷ 50

This procedure returns an optimum internal diameter of 9.9 mm, limited by the camber variation for the eternal wheel, which turns out to be the only active constraint.

To simplify the realization of the part, the final chosen diameter is 10 mm, just slightly bigger than the optimal one. *Table 5.11* sums up the mass results.

Table 5.11 – New front axle mass

Mass	136.6 g
Variation	-72.3 g
Variation %	-34.6%

In *Figure 5.11* and *Table 5.12* are reported deflections: plots show in black the actual deflection, while in red is highlighted the variation respect the original axle.

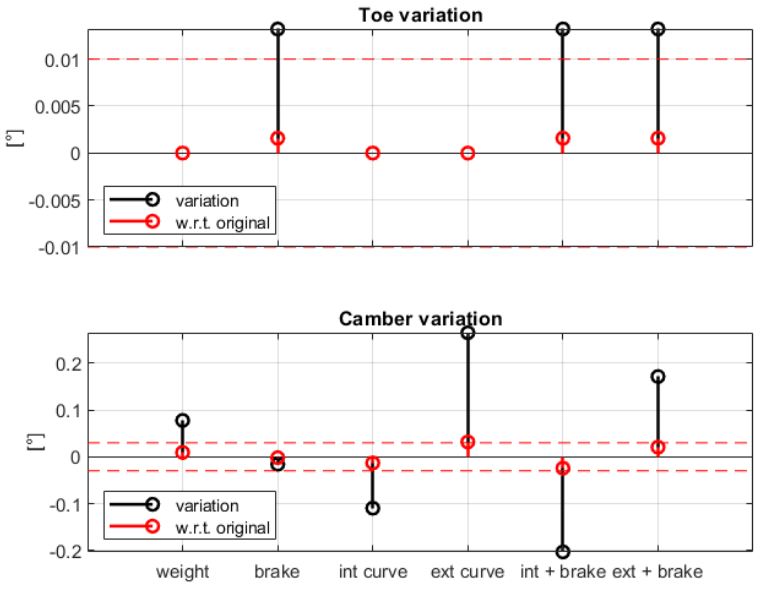

Figure 5.11 – Front axle angles variation

Table 5.12 – Front axle angles variation

[1e-3°]	weight	braking	Internal curve	External curve	Int curve + braking	Ext curve + braking
Toe	0	13.2	0	0	13.2	13.2
Toe variation	0	1.58	0	0	1.58	1.58
Camber	77.7	-15.9	-109.8	265.1	-203.3	171.6
Camber variation	9.30	-1.90	-13.1	31.7	-24.3	20.5

Despite the maximum difference with the original axle is really small (0.032°), the corresponding variation of camber angle is very big (0.27°): this happen because of the small inertia modulus of the section, since it depends on the four power of the diameter, which in turn is very small (17 mm). Anyway, since it depends on the internal diameter of the bearings, to increase it would be necessary to redesign the hub-carrier in order to accommodate bigger ones.

5.3 Rear axle

On rear axle are mounted the brake disc and the driven gear of the drivetrain: the coupling takes place by keys. The presence of the keyseats on the part (*Figure 5.12*), precludes the possibility to obtain a hollow axle: for this reason the component is left unchanged.

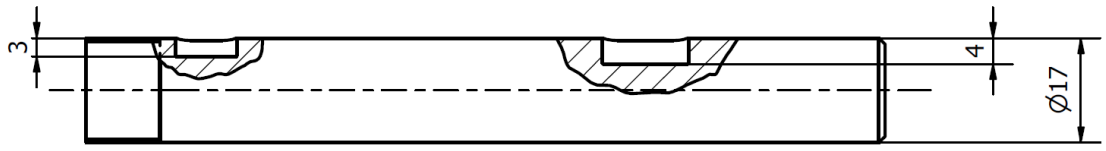

Figure 5.12 – Rear axle

5.4 Front hub

In *Figure 5.13* is represented the front hub, made from aluminium 6061-T6.

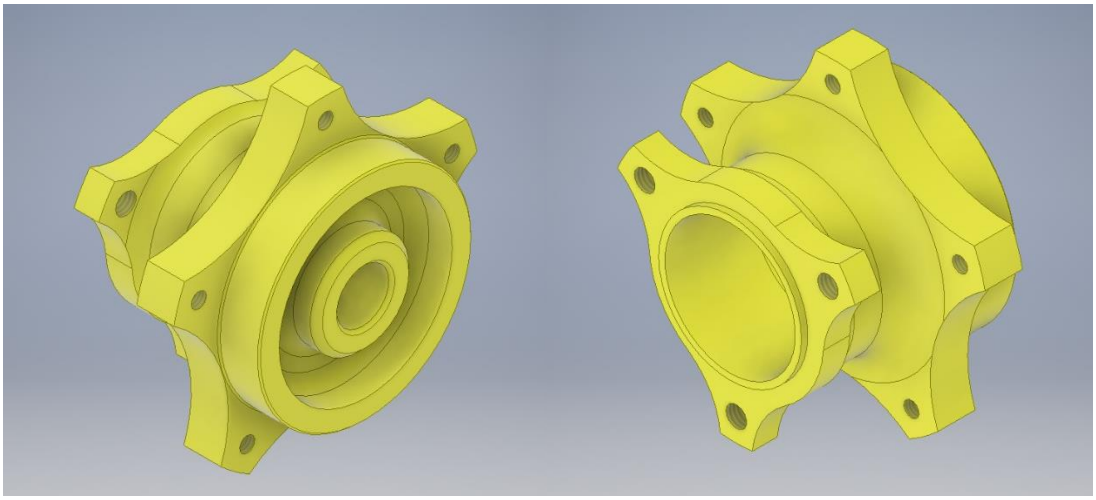

Figure 5.13 – Front hub

To reduce the mass of the hubs, a process of topology and shape optimization [10] has been applied. It consists in carrying out the following steps:

- Definition of the design space: the new part must respect some constraints about maximum dimension and position of some elements or constraints (e.g. the position of the bolts).
- Basic topology optimization: it is a method that optimize material layout, within the design space, for a given set of loads and constraints, with the goal of maximizing the performance of the system; the main difference from shape optimization and sizing is the possibility to have any shape within the design space: this step is useful to find a better shape that optimize the usage of the material.
- Preliminary design: the geometry found with the topology optimization is usually quite complex, thus difficult to obtain, especially without non-conventional manufacturing processes (e.g. additive manufacturing). In this step it is therefore defined a preliminary design according to the manufacturing constraints.
- Shape optimization: the preliminary geometry must be optimized according to some design variable, in order to obtain the best combination of them to satisfy constraints while minimizing a cost function.
- Final geometry: the result of this process is the geometry of the new part to be manufactured, which will have better overall performances than the original one.

5.4.1 Basic topology optimization

We must first define the design space, according to some constraints:

- Distance between wheel and brake (43 mm)
- Position of the bolts: five M6 on a diameter of 86 mm for the wheel, three M8 on a diameter of 68 mm for the brake

- Length of the threaded sections: it must be at least equal to the diameter of the bolt, so 8 mm for the brake support and 6 mm for the wheel bolts. However, due to the presence of vibration, the length on the side of the wheel must be greater than the minimum possible, according to previous experience it was decided to maintain a length of 12 mm.
- Wheel and brake centering: the first has an external diameter of 69 mm and a length of 13 mm, while the second a diameter of 46 mm and a length of 2 mm

In *Figure 5.14* and *Figure 5.15* is represented the rough geometry of the design space.

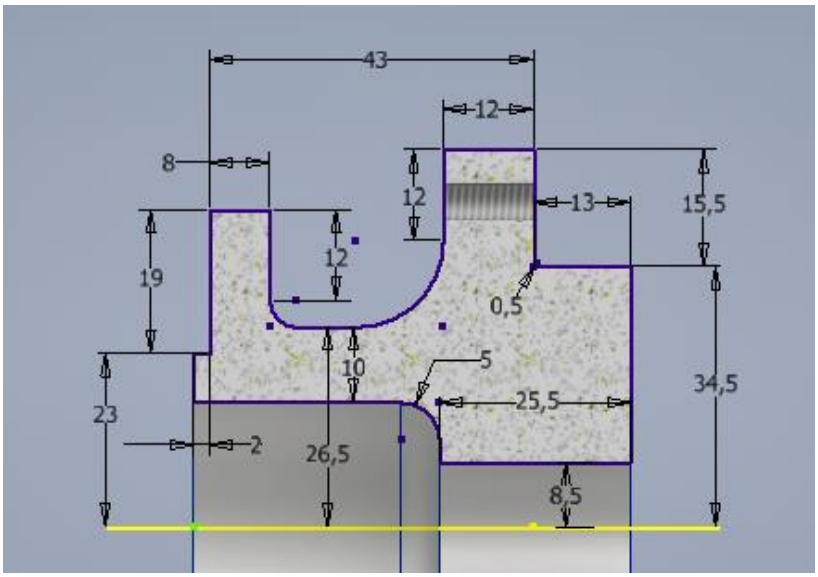

Figure 5.14 – Design space dimensions

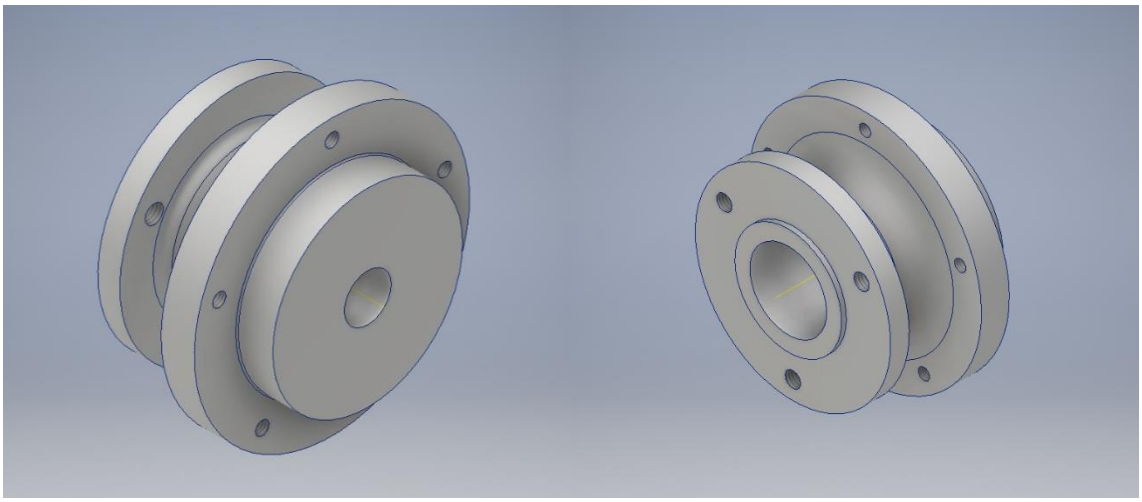

Figure 5.15 – Basic geometry

The topology optimization was made using *Altair Inspire*, a software created specifically for this type of analysis, able to generate weight-efficient design proposals.

The basic geometry has been imported in *Inspire*, creating partition to define the design space: threated holes, centering and the internal diameter must not be included in it (*Figure 5.16*).

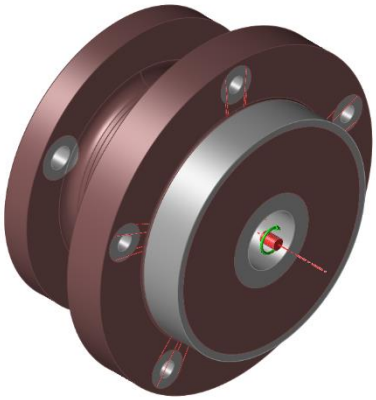

Figure 5.16 – Design space highlighted in brown

Two points are created on the rotation axis of the hub to define the application points of forces and constraints (*Figure 5.17*): one has been rigidly connected to the five holes concerning the bolted connection with the wheel, to which loads and moments coming from the it are applied, and the other one to the three holes on the brake side, who constrains the rotation around the axis and loaded with the forces coming from the eccentricity of the brake pad.

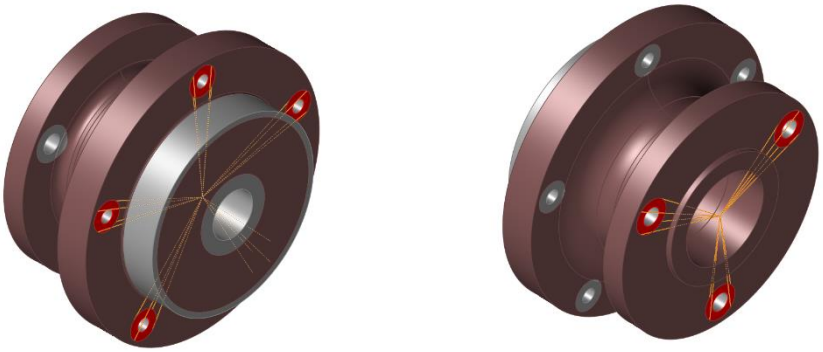

Figure 5.17 – Connections

The second point could be created in correspondence of the brake pad instead of on the rotation axis, but, for simplicity and to not create one reference point for each rotated load case, it was preferred to calculate and apply the forces due to the eccentricity are added to that single point (this is valid also for the following FEM analysis).

At the internal diameter, in correspondence of the shrink-fit, were constrained all the degrees of freedom but the axial rotation (since locked by the brake action).

The design space was divided into three part, in order to apply different shape controls (*Figure 5.18*):

- at the hub-wheel side a cyclic repetition with 5 planes of symmetry is imposed
- at the hub-brake disk side a cyclic repetition with 3 planes of symmetry is imposed

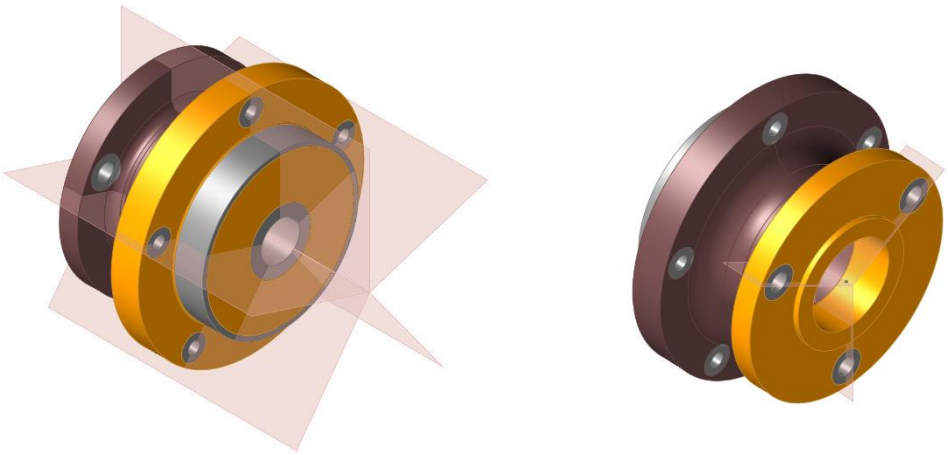

Figure 5.18 – Shape controls

Four different load cases were created, two rotated by 90° by the others, to simulate different stresses on the hub during rolling: two in braking condition and two in pure curve, using design loads. These forces are transported to the hub and the bending moments are:

$$M_x = F_y \cdot r_{wheel} + F_z \cdot d_y$$

$$M_y = F_x \cdot r_{wheel}$$

$$M_z = F_x \cdot d_y$$

where $r_{wheel} = 279\ mm$ is the wheel radius and $d_y = 46\ mm$ is the distance along Y axis from the contact patch (*Figure 2.1*).

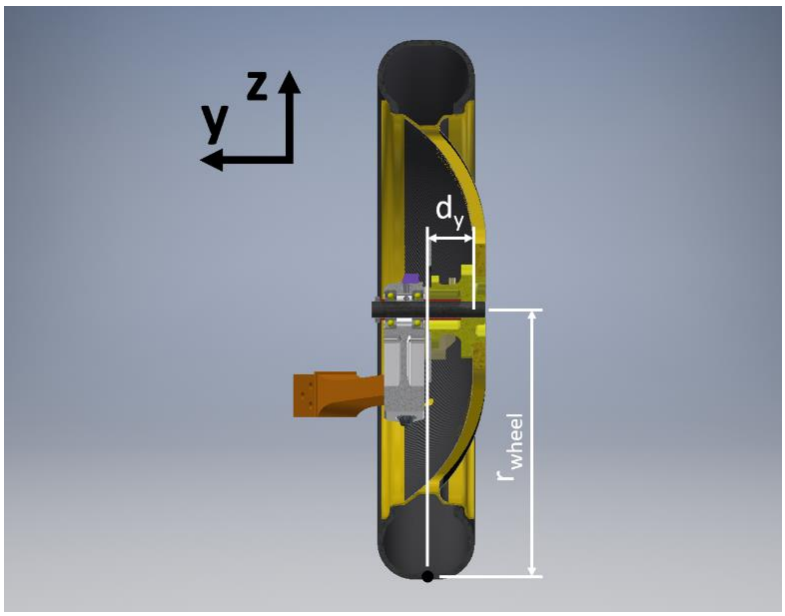

Figure 5.19 – Hub scheme

In *Table 5.13* forces and moments are reported. The forces on the brake are the same calculated in the previous section about the axle.

Table 5.13 – Front hub design loads

Design	F_x	F_y	F_z	M_x	M_y	M_z
Loads 0°	400 N	400 N	1200 N	-	-	-
Loads 90°	-1200 N	400 N	400 N	-	-	-
Curve 0°	0	400 N	1200 N	-	-	-
Curve 90°	-1200 N	400 N	0	-	-	-
Load case 0°						
Wheel	400 N	400 N	1200 N	166800 Nmm	-111600 Nmm	-18400 Nmm
Brake	-239.4 N	0	-1453.7 N	0	constrained	0
Load case 90°						
Wheel	-1200 N	400 N	400 N	18400 Nmm	-111600 Nmm	166800 Nmm
Brake	1453.7 N	0 N	-239.4 N	0	constrained	0
Load case pure curve 0°						
Wheel	0	400 N	1200 N	166800 Nmm	0	0
Brake	0	0	0	0	constrained	0
Load case pure curve 90°						
Wheel	-1200 N	400 N	0	0	0	166800 Nmm
Brake	0	0	0	0	constrained	0

The optimization objective is set as the mass minimization, with a minimum safety coefficient equal to 1.5. Results of the optimization are shown in *Figure 5.20*.

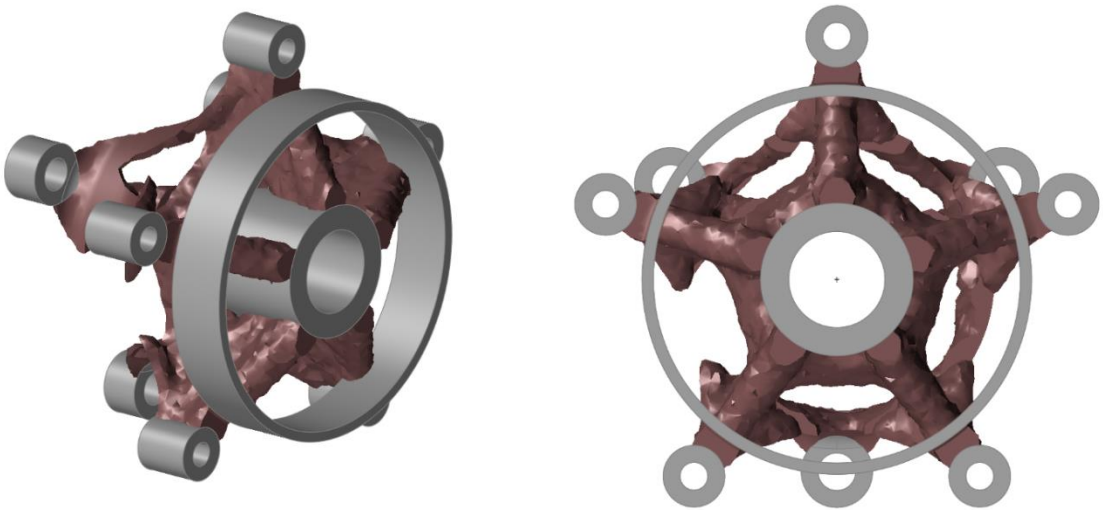

Figure 5.20 – Result of the mass minimization process

The obtained geometry with this analysis is very extreme and, as in this case, not satisfying. Therefore, a maximization of the stiffness was run, with a target mass equal to 30%. The results of this analysis are observable in Figure 5.21, Figure 5.22 and Figure 5.23.

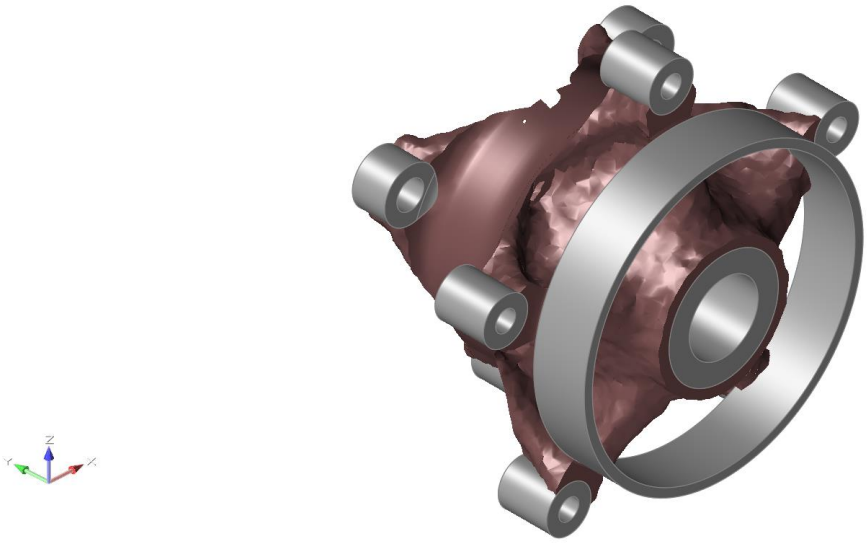

Figure 5.21 – Result of the stiffness maximization, isometric front view

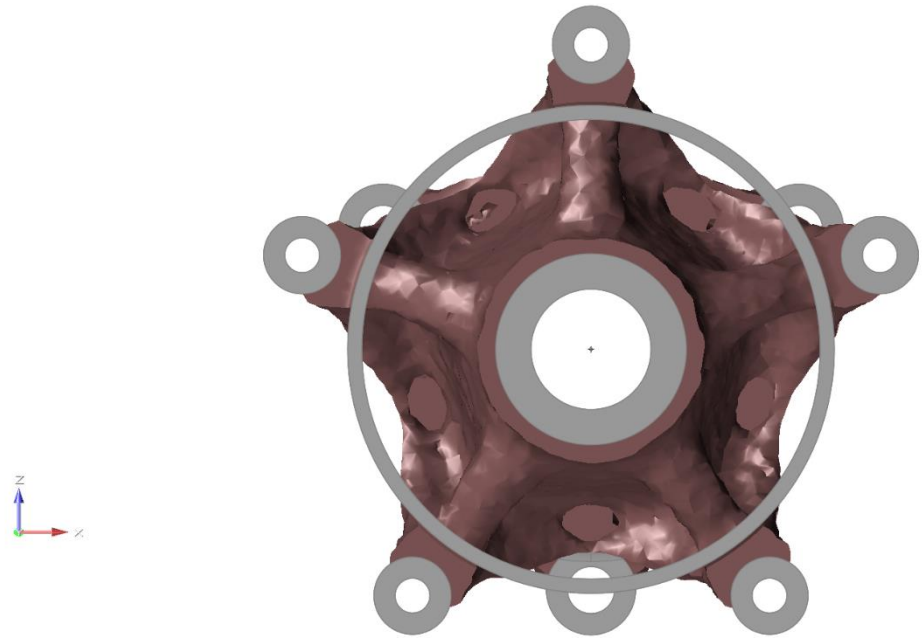

Figure 5.22 – Result of the stiffness maximization, front view

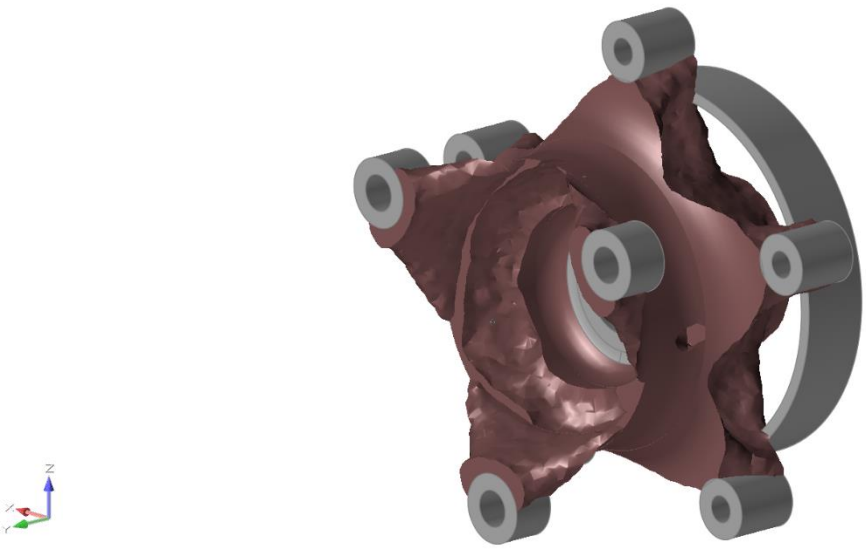

Figure 5.23 – Result of the stiffness maximization, isometric rear view

This time the result is much more meaningful to the creation of the preliminary design. The main feature that can be notice by the analysis are:

- "Star design" of the five wheel supports
- Small thickness of the hollow cylindrical section between the wheel and the brake side, increasing much as possible the external diameter (bigger inertia modulus)
- Material removal between the three brake supports

5.4.2 Preliminary design

Based on the result obtained through the topology optimization, a preliminary design is defined. In this phase the manufacturing process that is used is taken into account.

The first concept is shown in *Figure 5.24*:

- Triangular holes milled from the front to obtain the desired star shape
- Wheel and brake disk centerings have been thinned to 2 mm
- The thickness of the cylindrical cross-section in the middle was reduced to 2.5 mm, the minimum external diameter is constrained by the manufacturing process, the maximum internal diameter by the presence of the brake disk centering.
- Material removed by milling between the supports of the brake disc

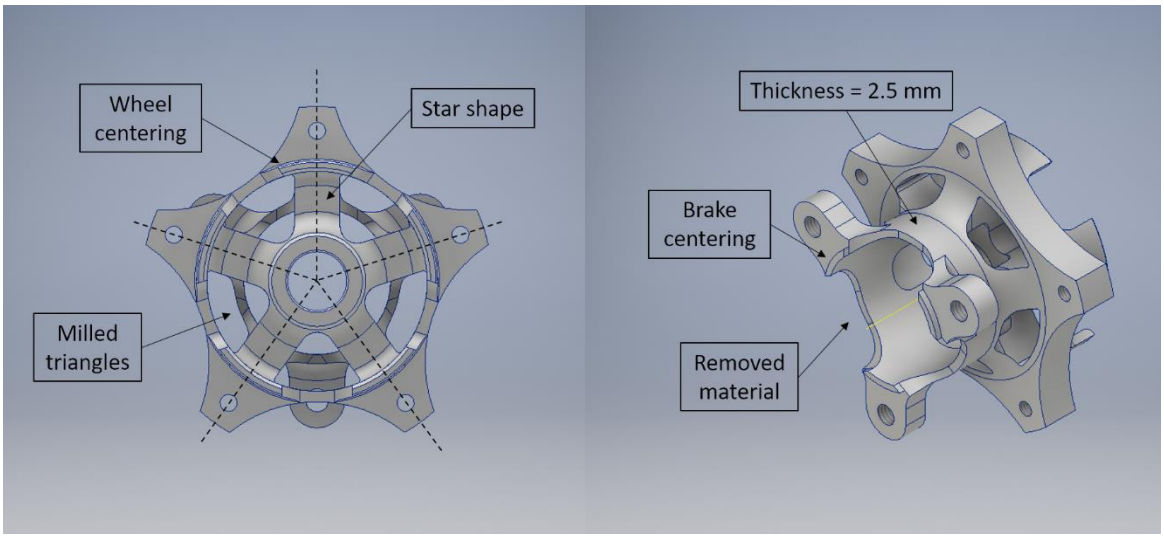

Figure 5.24 – Preliminary geometry, first version

A static assessment of the part is performed through the FE method, using the software *Abaqus*.

The part is imported as a 3D deformable solid part. A solid homogeneous section with the properties of the reference material is assigned to the solid region.

To apply load and constraints three reference points, positioned on the rotation axis of the hub, were created:

- Shrink fit: this reference point is created in the middle of the contact length of the shrink fit and it is connected with a rigid kinematic connection for all six degrees of freedom to the inner diameter of the hub (*Figure 5.25*)

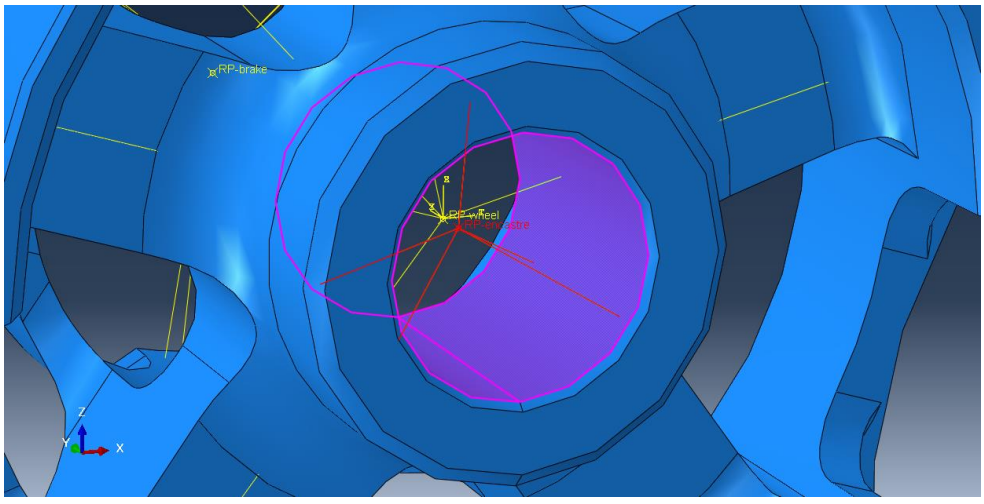

Figure 5.25 – Shrink fit coupling

- Wheel's bolted connection: a reference point is created on the plane of the hub-wheel interface and connected with a coupling to the contact surface between hub and wheel rim to simulate the friction bolted connection (*Figure 5.26*)

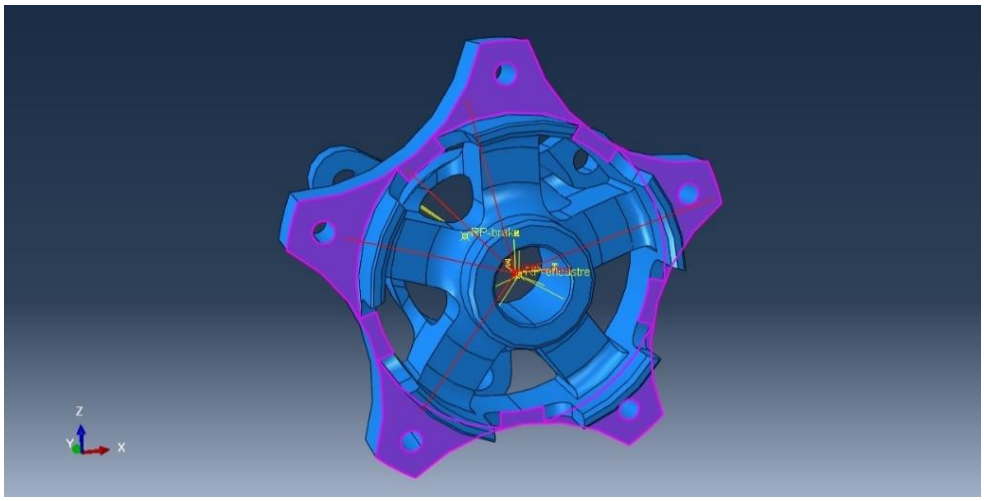

Figure 5.26 – Wheel coupling

- Brake disc's bolted connection: as for the wheel, also in this case the reference point was positioned on the plane of the friction bolted connection, coupled with a kinematic coupling locking all six d.o.f. (*Figure 4.22*)

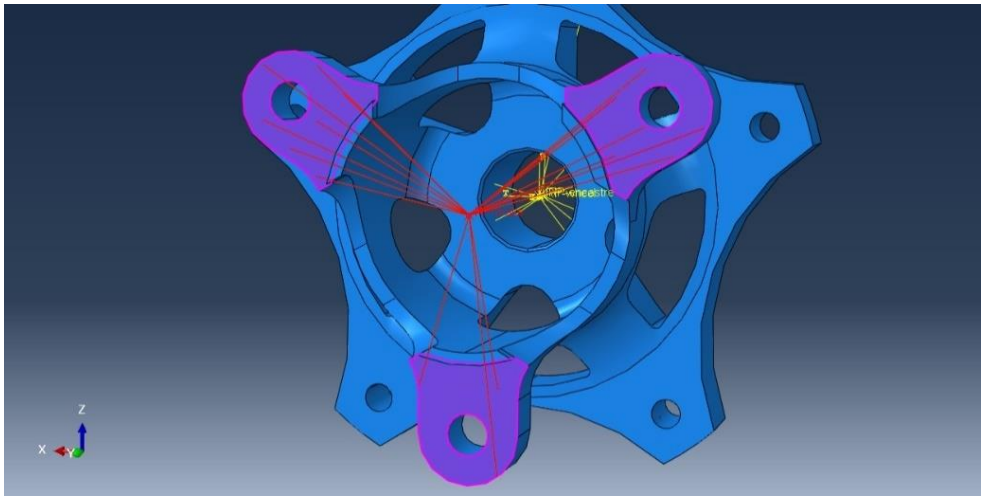

Figure 5.27 – Brake coupling

Boundary conditions are defined as follows:

- Displacements and rotation around the vertical and longitudinal axis locked by the shrink fit, applying these constraints to the coupled reference point
- Torsion locked by the brake, applying the constrain to the associated reference point

Also applied loads are the same of the topology analysis, shown in *Table 5.13*.

Due to the complexity of the shape, the mesh choice must fall to the tetrahedral one, setting a quadratic geometric order (C3D10 elements).

Resulting stresses of the radial supports of the wheels where satisfying, with a maximum stress from 140 to 150 MPa, obtained for the pure curve load case.

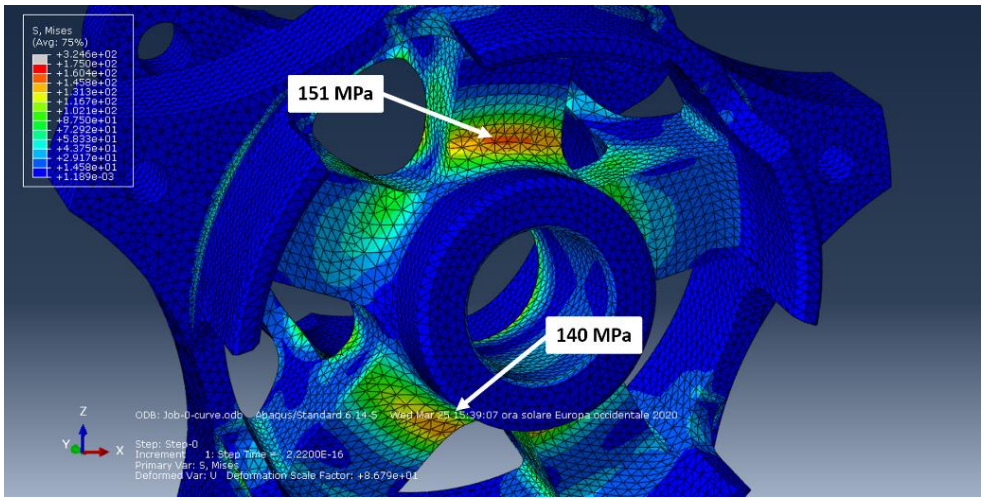

Figure 5.28 – First concept front stresses

Also in correspondence of the brakes support were no high stresses (braking load case), with values that not exceed much 140 MPa, as can be seen in *Figure 5.29*.

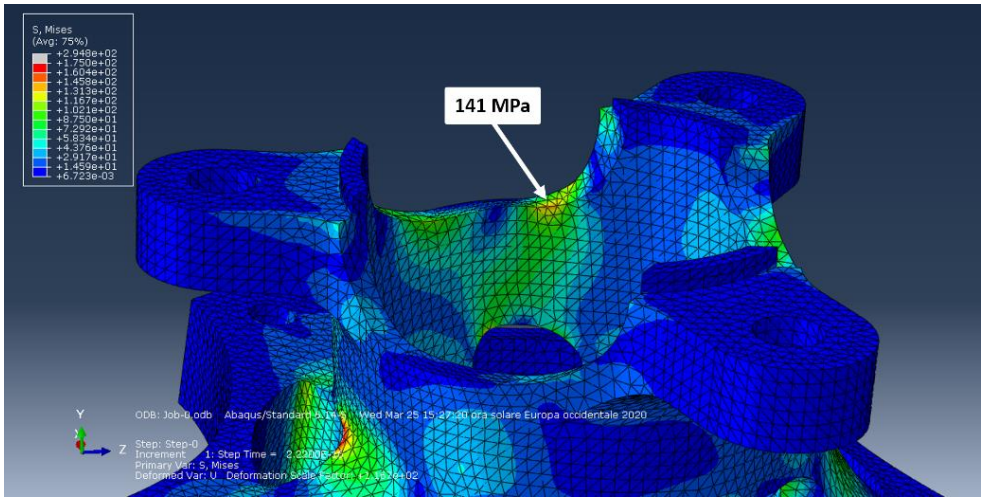

Figure 5.29 – First concept brake supports stresses

Very high value are obtained in correspondence of some edges, but since they are caused by the applications of the kinematic couplings, they are actually meaningless and unrealistic: since they are not in coincidence of critical stressed locations, these stresses can be neglected.

Anyway, at the notch between the wheel supports and the brake side, for the braking load case, there's a peak of the stresses caused by the combination of torsional and bending moments from the brake action, with values that reach 210 MPa.

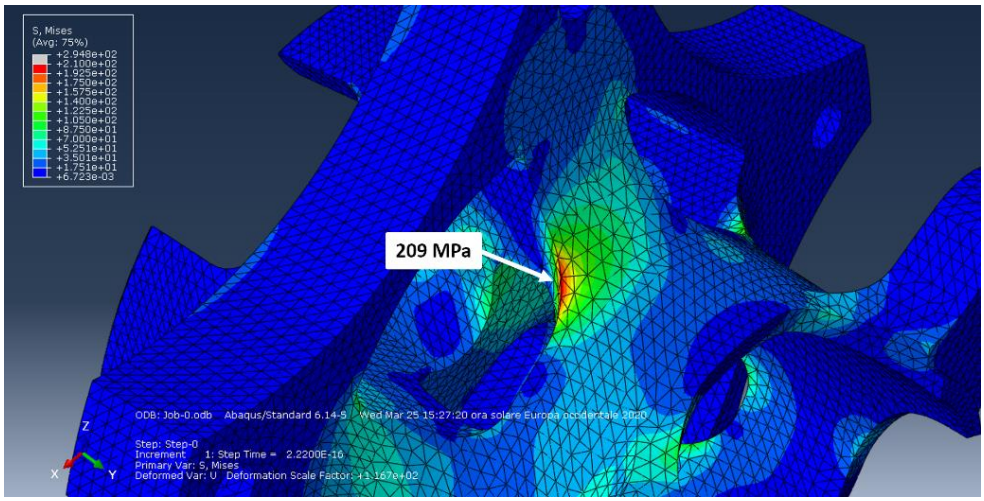

Figure 5.30 – First concept notch stress

Neither after some modification of this design, this problem has not been solved, precluding an effective shape optimization. Due to this structural problem and the difficulty to obtain this geometry by milling too, this design has soon been abandoned.

For the new design was decided to remove more material between the supports of the wheel and to leave five small shelves, one for each support and of the same width, avoiding cutting the cylindrical section to avoid that problematic notch effect. It was also possible to reduce the length threated section from 12 mm to 10 mm. These two variations of the design were a very efficient and effective way to reduce mass without increasing too much stresses nor reduce stiffness: indeed, since the bending moment depends on the distance from the application of the force, at the outer diameter stresses are low, so less material is needed in this area.

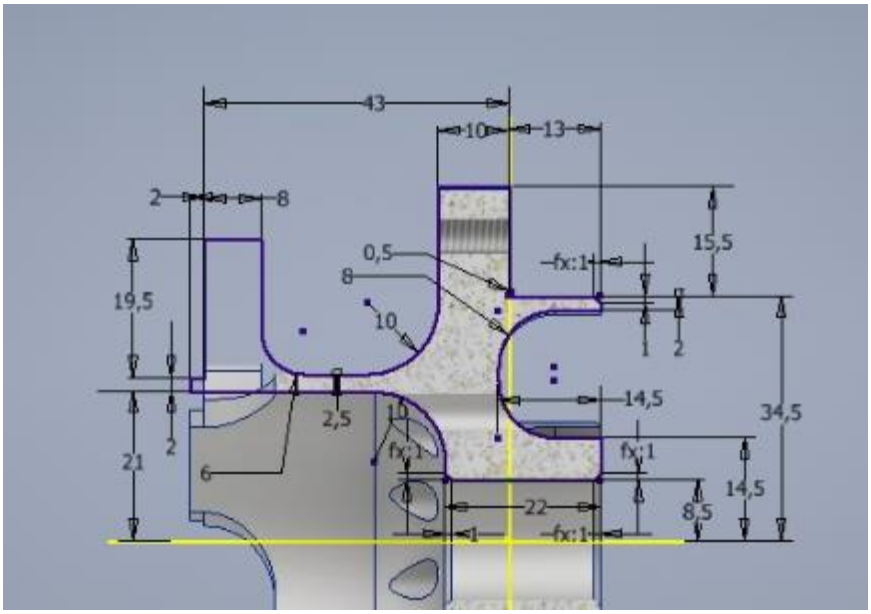

Figure 5.31 – Preliminary design dimensions

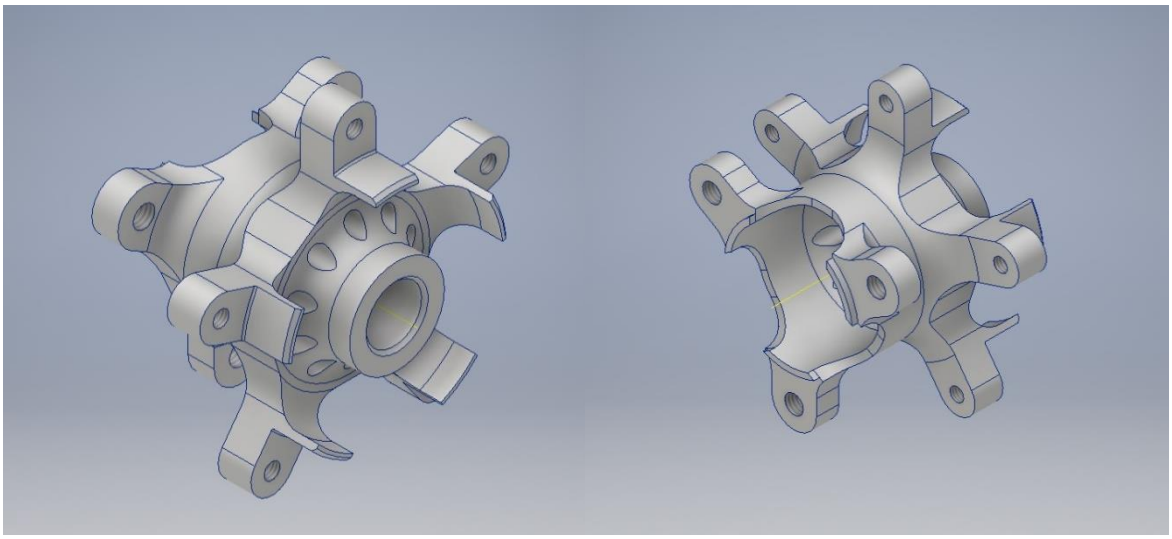

Figure 5.32 – Preliminary design, front and rear isometric view

Moreover, 10 holes of 5,5 mm of diameter (simple to obtain by drilling) were created on the frontal surface, to reduce the overall weight.

The part on the brake side weas mainly unchanged from the previous design, since the result from the FEM analysis were satisfying, without the presence of overstressed areas.

Before proceeding with the shape optimization, also this design was checked with a FEA; results are shown in *Figure 5.33*, *Figure 5.34* and *Figure 5.35*.

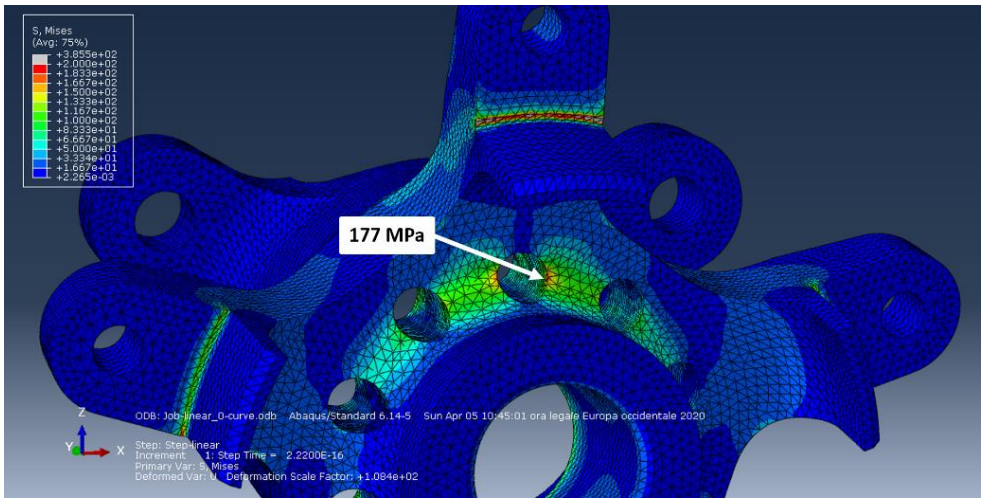

Figure 5.33 – Preliminary design holes stress

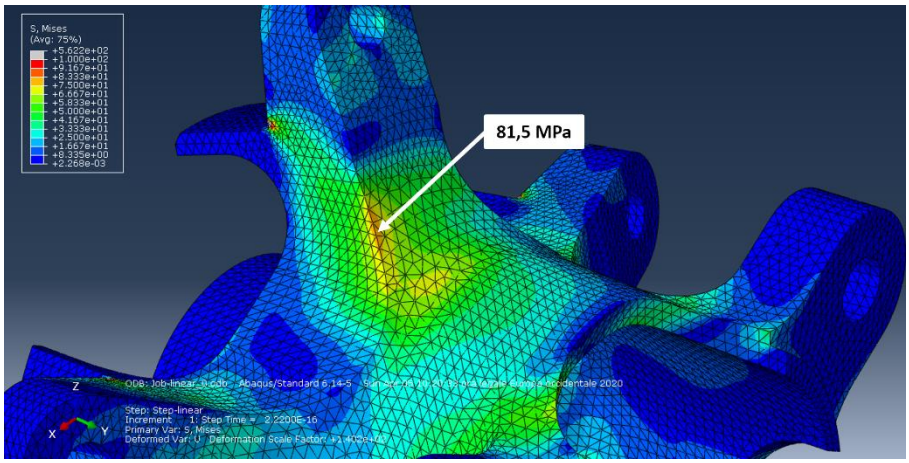

Figure 5.34 – Preliminary design wheel supports stress

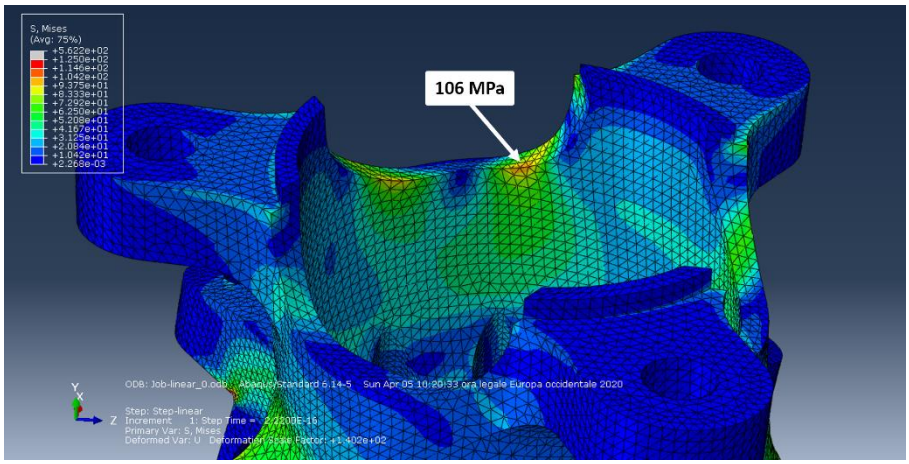

Figure 5.35 – Preliminary design brake supports stress

The higher stress is in correspondence of the holes (177 MPa), but still much lower than the yield stress of the material, with a safety factor $\eta = \frac{240}{177} = 1.36$.

The analysis of the shrink-fit is necessary too, but, for the linearity of the subjected topic, it is discussed in the dedicated section (*5.5.1 Shrink-fit*).

5.4.3 Shape optimization

The topology optimization process is followed by the shape optimization process.

Hub-wheel rim connection areas are schematized as cantilever beams, as shown in *Figure 5.36*.

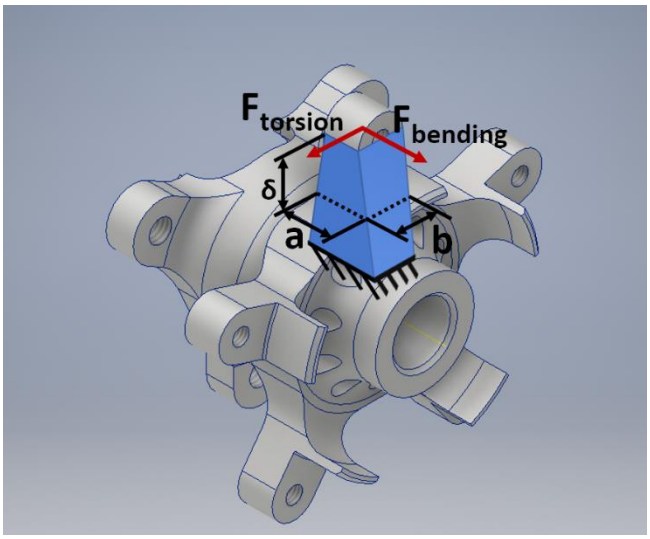

Figure 5.36 – Schematization of the supports

Bending moments transmitted by the wheel generates forces in axial direction in correspondence of the bolted connection, while the torque due to braking generates forces in circumferential direction, as shown in *Figure 5.36*. Stresses in a generic section can be calculated as:

$$\sigma_{bending} = \frac{M_b \cdot \frac{a}{2}}{J_{bending}} = \frac{F_{bending}\delta \cdot \frac{a}{2}}{J_{bending}}$$

$$\sigma_{torsion} = \frac{M_t \cdot \frac{b}{2}}{J_{torsion}} = \frac{F_{torsion}\delta \cdot \frac{b}{2}}{J_{torsion}}$$

Inertia modula of the section are calculated as:

$$J_{bending} = \frac{1}{12}a^3 b\,, \qquad J_{torsion} = \frac{1}{12}ab^3$$

where a and b are the dimensions of the cross-section (*Figure 5.36*).

From these formulas you can see that there's a linear correlation between b and $\sigma_{bending}$ while it is quadratic respect a, vice versa for $\sigma_{torsion}$.

About stiffness can be written the following formulas:

$$\eta = \frac{\delta^3}{3EJ}F\,, \qquad \phi = \frac{\delta^2}{2EJ}$$

where η and ϕ are the deflection and the rotation at the free end respectively.

From these simple equations is made obvious that the best way to reduce stress and increase stiffness is to increase the inertia modulus. Since we are interested reducing the variation of camber and toe angle, bending stiffness is the focus of the optimization.

The chosen parameters for this analysis [8] [9] then are:

- Thickness of the circumferential cross-section (*Figure 5.37*): this is related to the dimension a and, due to the non-linearity of the action of this parameter, the sensitivity analysis must

be on three level: 8.5 mm (base case of the preliminary geometry), 9.5 mm (+1 mm) and 11 mm (+2.5 mm).

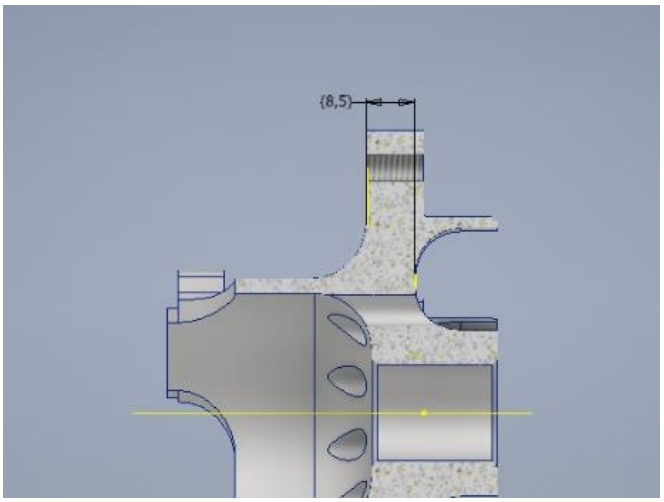

Figure 5.37 – Thickness parameter

- Angle between lateral faces of the support (*Figure 5.38*): this is related to the parameter b, increasing the width linearly the width of the wheel support, to compensate the bending moment which also increase linearly ($M_b = F \cdot \delta$, where δ is the distance from the applied force). The sensitive analysis was done on two cases: 0° (base case) and 10°.

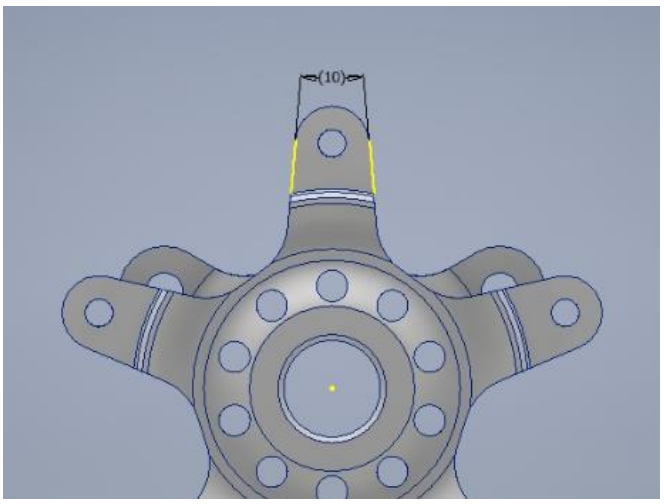

Figure 5.38 – Inclination parameter

- Holes: it is also analysed the influence of the presence of the ten holes on the front surface.

The analysis of the deformation are done again with the *Abaqus* FEA software: this procedure allows to measure the angles obtained at the wheel (the value are taken in correspondence of its reference point), for the three load case applied, each of which constituted by a unitary concentrated moment the wheel of 1 Nm on a different axis:

- M_x and M_z are the bending moments, their resulting angle values are averaged to obtain the bending stiffness (different values can be caused by the non-symmetry of the geometry for the two different axis).
- M_y is the torque moment, which doesn't affect the characteristic angles.

FE models are defined in the same way of section *5.4.2*. From the angle is then possible to calculate the stiffness as:

$$K_\theta = \frac{M}{\theta}$$

To compare the various result is also useful to normalize those values dividing them by the mass: this procedure shows which variation "uses better the material", so permitting a higher increase of performance for the same mass gain.

For each analysis is modified only one parameter at time to understand its contribution to mass and stiffness of the hub. In *Table 5.14* are reported the values of mass, rotational inertia, bending and torsional stiffness of the various cases, showing also the normalized values and the percentage variance.

Table 5.14 – Front hub sensitivity analysis

	Base	+ 1 mm	+ 2.5 mm	+ 10°	No holes
Mass [g]	150.00	154.00	160.00	155.00	158.00
Inertia [kgm^2]	108.87	111.24	114.79	114.06	111.46
Bending stiffness [Nm/°]	1677.7	1888.4	2236.8	1752.5	2111.7
Torsional stiffness [Nm/°]	1980.2	2001.9	2013.8	2048.3	2014.0
Variance %					
Mass	-	2.67%	6.67%	3.33%	5.33%
Inertia	-	2.18%	5.44%	4.77%	2.38%
Bending stiffness	-	12.56%	33.33%	4.46%	25.87%
Torsional stiffness	-	1.10%	1.70%	3.44%	1.71%
Normalized by mass					
Inertia [kgm^2/g]	0.726	0.722	0.717	0.736	0.705
Bending stiffness [Nm/°/g]	11.184	12.262	13.980	11.306	13.365
Torsional stiffness [Nm/°/g]	13.201	12.999	12.587	13.215	12.747
Normalized variance %					
Inertia	-	-0.48%	-1.15%	1.39%	-2.80%
Bending stiffness	-	9.64%	24.99%	1.09%	19.50%
Torsional stiffness	-	-1.53%	-4.66%	0.11%	-3.44%

Other useful information to optimize the shape can be extrapolated by normalizing the variations by the mass variation (*Table 5.15* and *Figure 5.39*): in this way we can get information about how much each added gram affect the final result. From the percentual variance can be seen if the added material is better (positive values) or worse (negative value) used for that scope. In the next table and the correlated plot are presented these values.

Table 5.15 – Variations ratios

	+ 1 mm	+ 2.5 mm	+ 10°	No holes
Inertia [kgm^2/g]	0.593	0.593	1.039	0.325
Bending stiffness [Nm/°/g]	52.682	55.913	14.963	54.252
Torsional stiffness [Nm/°/g]	5.423	3.369	13.633	4.227
Variance %				
Inertia	-18.4%	-18.3%	43.2%	-55.3%
Bending stiffness	371.0%	399.9%	33.8%	385.1%
Torsional stiffness	-58.9%	-74.5%	3.3%	-68.0%

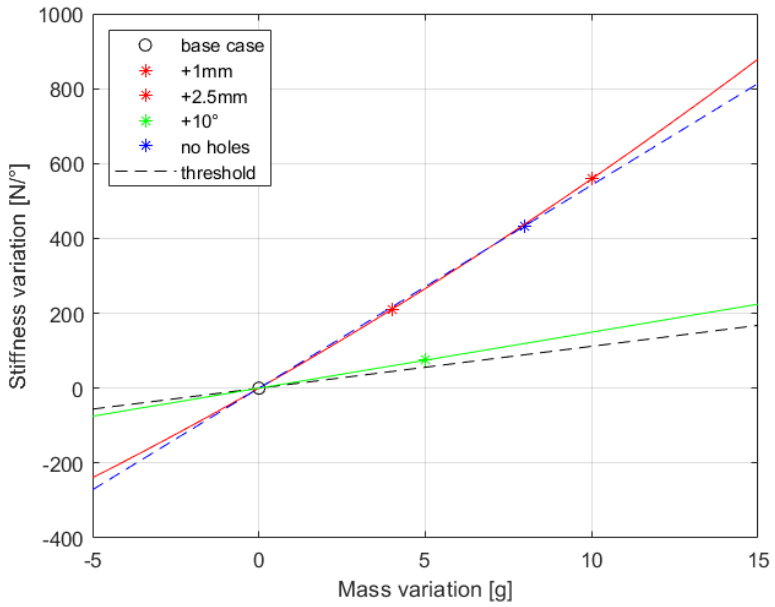

Figure 5.39 – Stiffness-mass variation diagram

The threshold line in the plot in *Figure 5.39* represent the points in which we have the same bending stiffness/mass ratio of the base case.

From these data it can be seen how increase the stiffness and remove the holes are very effective increasing the bending stiffness, with comparable results, while increasing the inclination, also if has beneficial effect, is much less suitable for the purpose since its effort is one order of magnitude lower respect the variation of the other two parameter. This is supported by the fact that thickness and removing holes add material near the centre of the hub, here the stresses due to the bending moment, giving a great contribution to the stiffness.

For the same reason, nothing but increasing the inclination is an effective way to increase the torsional stiffness: since the material added near the centre is mainly located under the section that connect the wheel side to the brake side, it does not actively participate withstand stresses due to the torque. Anyway, since our main interest is to increase the bending stiffness, the variation of this parameter has not been considered, leaving faces of the supports parallel.

So, for the final design the following decisions were made:

- Removal of the holes: this option not only has beneficial effect for the stiffness, but also it permits to simplify the overall design, reducing the machining operations, thus the cost of the part
- Since that is an "on-off" option, to increase more the stiffness, is required to vary also the thickness in order to reach the target

The target is defined by the angle variation in working condition: considered load are the same used for calculation concerning suspension tubes and axle. These values and the transportation moments are shown in *Table 5.16*.

Table 5.16 – Front hub race loads

	weight	braking	Internal curve	External curve
F_x	0	160 N	0	0
F_y	0	0	-120 N	120 N
F_z	400 N	476.7 N	316 N	484 N
Transportation moments				
M_x	18400 Nmm	21929 Nmm	-18944 Nmm	55744 Nmm
M_y	0	-44640 Nmm	0	0
M_z	0	-7360 Nmm	0	0

Since the higher bending moment is obtained for the outer wheel during curve, if we want to contain the camber variation between 20 and 25 thousandths of degree, the target stiffness must be approximately equal to

$$K_{\theta,target} = \frac{M}{\theta} = \frac{55.744\ Nm}{0.0225°} = 2477.5 \rightarrow 2500\ Nm/°$$

To obtain this value we start from the design without holes, increasing thickness to reach the desired stiffness. The contribute of the thickness is more than linear (as visible from the graph in *Figure 5.39*) but, in the small considered variation interval, it can be considered linear, thus simplifying calculations.

The thickness must increase the stiffness from the no holes case, i.e.

$$\Delta K_{\theta,thick} = K_{\theta,target} - K_{\theta,holes} = 2500 - 2111.7 = 338.7\ \text{Nm}/°$$

The contribution for each added millimetre added to the thickness is simply calculated as

$$k_{thick} = \frac{stiffness}{thickness} = \frac{K_{\theta,2.5mm} - K_{\theta,base}}{2.5\ mm} = \frac{599.1\ Nm/°}{2.5\ mm} = 223.6\ Nm/°/mm$$

Finally, we are able to find the required thickness variation as

$$\Delta Thick = \frac{\Delta K_{\theta,thick}}{k_{thick}} \cong 1.7\ mm \rightarrow 1.5\ mm$$

With this value of thickness, the expected bending stiffness for the front hub is 2447 Nm/°, with a torsional stiffness of 2034 Nm/° and a mass of 164 g.

The final design has been found and it must be also be subjected to Finite Elements Analysis, in the already shown way, to verify actual properties. The results have been sum up and compared to the original and the preliminary designs in *Table 5.17*.

Table 5.17 – Front hub results

	Original	Preliminary	Final
Mass [g]	333.00	150.00	164.00
Inertia [kgm^2]	268.08	108.87	114.65
Bending stiffness [Nm/°]	6039.66	1677.7	2510.0
Torsional stiffness [Nm/°]	5524.37	1980.2	2027.2
Variance %			
Mass	-	-54.95%	-50.75%
Inertia	-	-59.39%	-57.23%
Bending stiffness	-	-72.22%	-58.44%
Torsional stiffness	-	-64.16%	-63.30%
Normalized to the mass			
Inertia [kgm^2/g]	0.805	0.726	0.699
Bending stiffness [Nm/°/g]	18.137	11.184	15.305
Torsional stiffness [Nm/°/g]	16.590	13.201	12.361
Variance %			
Inertia	-	-9.85%	-13.16%
Bending stiffness	-	-38.33%	-15.62%
Torsional stiffness	-	-20.43%	-25.49%

The obtained stiffness of the new design is 2510 Nm/°, a higher than the one expected from calculation: this difference can be given by a non-independence of the two parameter, since both modify the quantity of the material in the same region.

The final design is also better in all the way with respect to the preliminary design (except for the mass): it has higher bending and torsional stiffness and the material is better exploited too.

Unfortunately, as clearly visible from the negative values of the normalized percentage variance, the new hub is less efficient with respect to the original: in the optimization has been shown how effective is increasing thickness for the stiffness and, since the original part is very thick, this explain this result. Anyway, since the main purpose of this study was to reduce the mass while maintaining a shape obtainable by chip removal process, thickness had to be reduced and the results are acceptable since the angle variation are small enough.

5.5 Front hub and axle interaction

After the processes of re-design front axle and hub, it is necessary to analyse their interaction: the two part must indeed be shrink-fitted, so in the next section stresses are verified by analytic formulas and Finite Elements Method. In the second section is discussed the variation of the characteristic angle in working condition, comparing the original system to de new one.

5.5.1 Shrink-fit

Shrink-fitting is a technique in which the joint between two elements is achieved by an interference fit of an internal part (shaft) with a diameter slightly bigger than the external one (hub). The mounting is made by exploiting the phenomenon of thermal expansion, cooling down the shaft and/or heating up the hub, thus decreasing and increasing respectively their dimensions.

Shrink fit it's a very effective method to obtain a mechanical joint, allowing to sustain high forces and torques, transmitted by the friction generated from the contact pressure at the interference. The pressure comes from the elastic forces due to the expansion of the hub and the compression of the shaft.

The first step consists to find the relation between the interference and the contact pressure [11]. Interference is defined as the difference between the external diameter of the shaft and the internal diameter of the hub and after the fitting the two dimensions must coincide. It is then possible to write:

$$i = D_S - D_H\,, \qquad D_S + \Delta D_S = D_H + \Delta D_H \quad \rightarrow \quad i = \Delta D_H - \Delta D_S$$

Variation of diameter can be expressed in function of the hoop strains and, since $D_H \cong D_S \cong D$, we write:

$$\Delta D_H = \varepsilon_{\theta,H} D_H = \varepsilon_{\theta,H} D$$
$$\Delta D_S = \varepsilon_{\theta,S} D_S = \varepsilon_{\theta,S} D$$

Based on constitutive law, hoop strains are calculated as

$$\varepsilon_{\theta,H} = \frac{1}{E_H}\left(\sigma_{\theta,H} - \nu_H \sigma_{r,H}\right)$$
$$\varepsilon_{\theta,S} = \frac{1}{E_S}\left(\sigma_{\theta,S} - \nu_S \sigma_{r,S}\right)$$

where E is the elastic modulus, σ_θ and σ_r hoop and radial stress respectively and ν the Poisson's ratio.

From the general equation for stresses in a disc, can be found the relation of tangential and radial stresses to the internal (for the hub) or external (for the shaft) pressure p.

At the internal diameter of the hub, stresses are:

$$\begin{cases} \sigma_{\theta,H} = p\dfrac{a_H^2 + 1}{a_H^2 - 1} \\ \sigma_{r,H} = -p \end{cases}$$

where $a_H = \frac{D_{ext,H}}{D_{int,H}}$. At the external diameter of the shaft:

$$\begin{cases} \sigma_{\theta,S} = -p\dfrac{a_H^2 + 1}{a_H^2 - 1} \\ \sigma_{r,S} = -p \end{cases}$$

Where $a_S = \frac{D_{ext,S}}{D_{int,S}}$. From the previous formulas is finally possible to write the relation between interference and contact pressure:

$$p = \frac{i}{D}\left(\frac{a_H^2 + \nu_H}{E_H} + \frac{a_S^2 - \nu_S}{E_S}\right)^{-1}$$

Table 5.18 sums up the data required to calculate stresses of the shrink-fit.

Table 5.18 – Shrink-fit data

Hub	
D_{ext}	29 ÷ 48 mm
Tolerance: S7	-21 ÷ -39 µm
E (aluminium)	70 GPa
v (aluminium)	0.33
Axle (shaft)	
D_{int}	10 mm
Tolerance: h6	0 ÷ -11 µm
E (steel)	206 GPa
v (steel)	0.3
Interference	
Minimum	10 µm
Maximum	39 µm
D	17 mm
Contact length	22 mm
μ_s steel-aluminium	0.61

We first need to verify if the contact length is enough to sustain the lateral forces: this must be calculated for the lower possible contact pressure and compared to the lateral design load ($F_y = 400\ N$). The external diameter of the hub is not constant and, for this analysis, is considered the minimum one since it gives the lower contact pressure. The minimum pressure obtained by the minimum interference, it's equal to 13.84 MPa

The joint must resist to the lateral force and, since the brake is mounted directly on the hub (differently to the rear one), it doesn't have to sustain any torque.

The total lateral force is equal to the integral of the tangential stress on the interface:

$$F_{y,MAX} = \int_0^{2\pi} \tau_{ax} L \frac{d}{2} d\theta = \tau_{ax} L d\pi = \mu_s p L d\pi = 9922\ MPa$$

Applying the formula with minimum contact pressure, 13.8 MPa, we found that the maximum lateral force is much greater than needed.

After this result it could be though to change the tolerances in order to obtain less interference, thus reducing maximum stresses, but, since the rod for the axles are only available with h6 tolerance and we must have interference fit, the choice has to be the S7, so it cannot be changed (for H6 you have backlash, while for X8 the interference is more severe).

For the failure resistance the maximum interference is considered, since it gives rise to the higher pressure and stresses. Von-Mises stresses are calculated with the multiaxial criterion:

$$\sigma_{VM} = \sqrt{(\sigma_\theta - \sigma_r)^2 + (\sigma_\theta - \sigma_{ax})^2 + (\sigma_{ax} - \sigma_r)^2}$$

where the axial stress in the axle is due to the bending moment. In the *Table 5.19* are reported the results in correspondence of the minimum and maximum external hub diameter.

Table 5.19 – Shrink-fit results

	$D_{ext,H,min}$ = 29 mm	$D_{ext,H,MAX}$ = 48 mm
Contact pressure	53.99 MPa	72.52 MPa
Hub		
Hoop stress	110.5 MPa	93.33 MPa
Radial stress	-53.99 MPa	-72.52 MPa
Von-Mises stress	145.2 MPa	144.0 MPa
Axle		
Hoop stress	-111.1 MPa	-149.3 MPa
Radial stress	-53.99 MPa	-72.52 MPa
Axial stress	474.7 MPa	474.7 MPa
Von-Mises stress	559.4 MPa	589.3 MPa

Shrink-fit, as well as with analytic formulas, was also verified with a Finite Elements Analysis: the hub was imported from the *Inventor* CAD software, drawn with the minimum possible inner diameter allowed by the tolerance (16.963 mm), while the axle, due to its simple shape, was directly drawn as 3D solid deformable extruded part in *Abaqus*.

The axle was partitioned to define the location of the two bearings (A and B) and the contact surface of the shrink-fit (H in *Figure 5.40*).

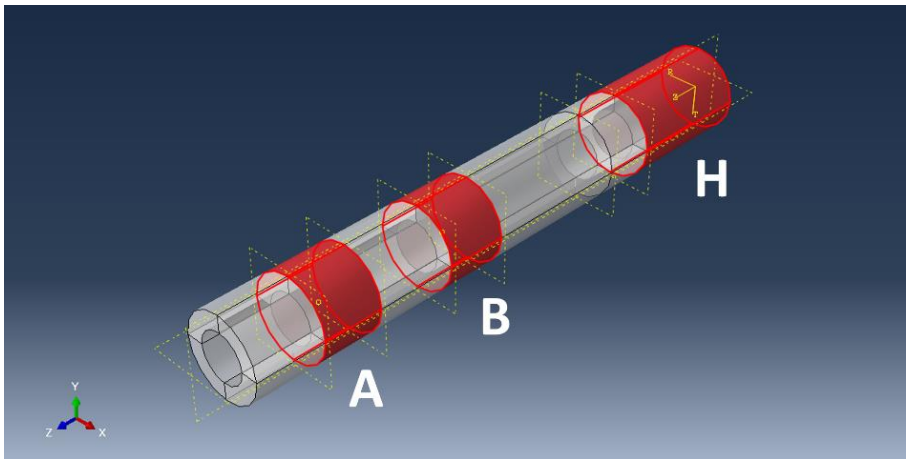

Figure 5.40 – Axle partitioning

Then to each part was applied a solid homogeneous section of the respective material: steel (elastic homogeneous, Young's modulus equal to 206000 MPa and Poisson's ratio of 0.3) for the axle and aluminium (elastic modulus 70000 MPa, Poisson's ratio 0.33) for the hub.

For this analysis was created a static general step and, to reach convergence, it was necessary to enable the *automatic stabilization*, setting the damping factor to 0.0002 (the standard value provided by *Abaqus*).

To apply loads and constraints, four reference point were created: two for the bearings and other two for wheel and brake's bolted joints, as done for the hub FEA: also in this case, they were rigidly coupled to the relative surface, as shown in *Figure 5.41*.

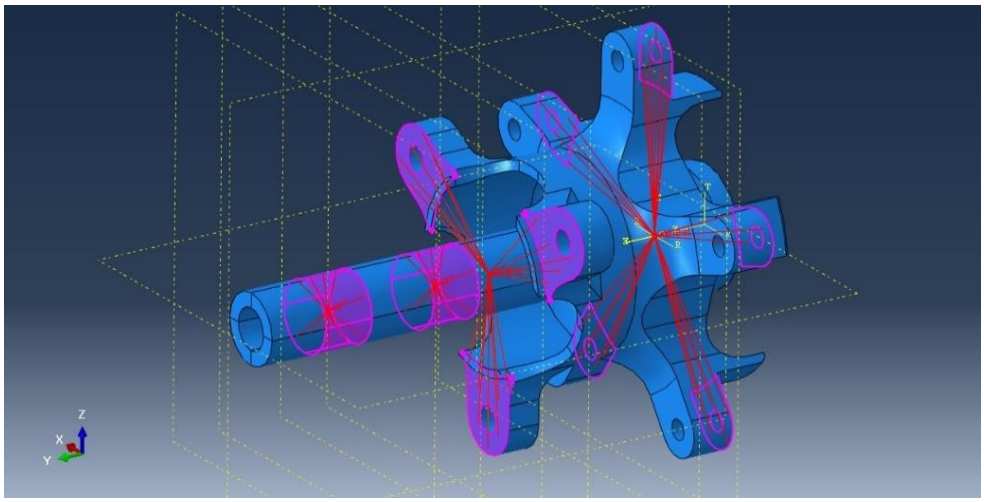

Figure 5.41 – Bearings and bolted joints' couplings

At shrink-fit was created a surface-to-surface contact interaction: sliding formulation was set to *small sliding* and in *option* was selected to *gradually remove slave node overclosure during the step*. For the *contact property* two behaviour were defined:

- Tangential: to describe interaction effects due to friction, with an isotropic coefficient of 0.61 (static value for aluminium-steel contact)
- Normal: to actually create the contact between the two surfaces, setting the *pressure-overclosure* to *"hard" contact*

This interaction was applied between the external diameter of the axle, chose as master surface (in red), and the inner diameter of the hub (highlighted in pink in *Figure 5.42*).

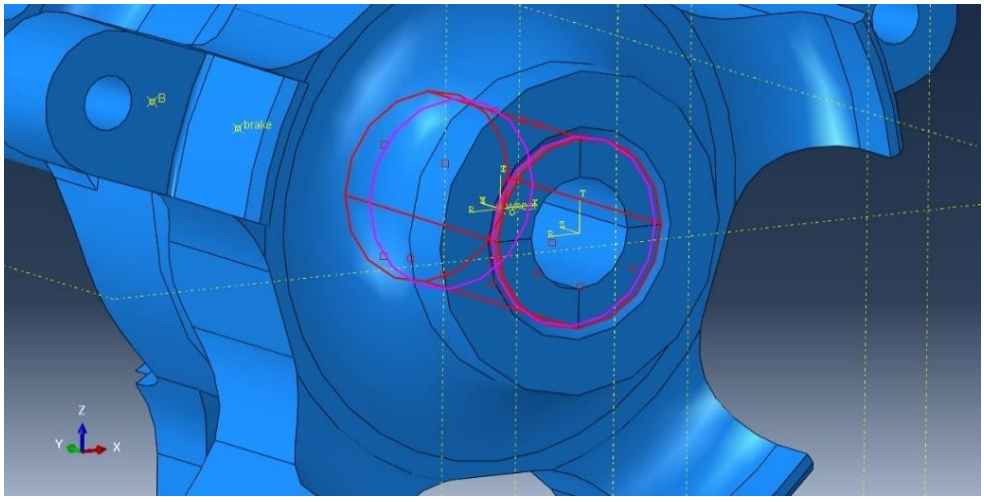

Figure 5.42 – Surface-to-surface contact of the shrink-fit

The constrain applied are:

- Bearing A: all displacements
- Bearing B: longitudinal and vertical direction
- Brake: torsion

As previously said, due to the shape of the hub you need to use tetrahedral mesh but, because of the complexity given by the interaction, the linear geometry version (*C3D4*) was chosen. A shrewdness to respect was to use a more refined mesh for the slave surface (hub) with respect to the master one (shaft), as shown in *Figure 5.43*: seeds chosen are 0.6 mm for the hub and 1 mm for the axle.

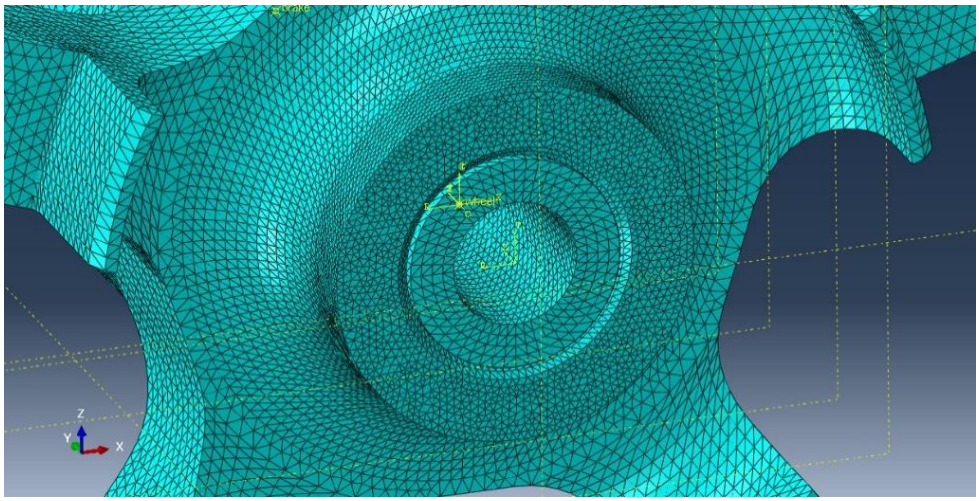

Figure 5.43 – Shrink-fit mesh

Data was taken from two different linear paths on the internal diameter of the hub (*Figure 5.44*): one (path 1) in correspondence of the section of the wheel support and one (path 2) in the section between them.

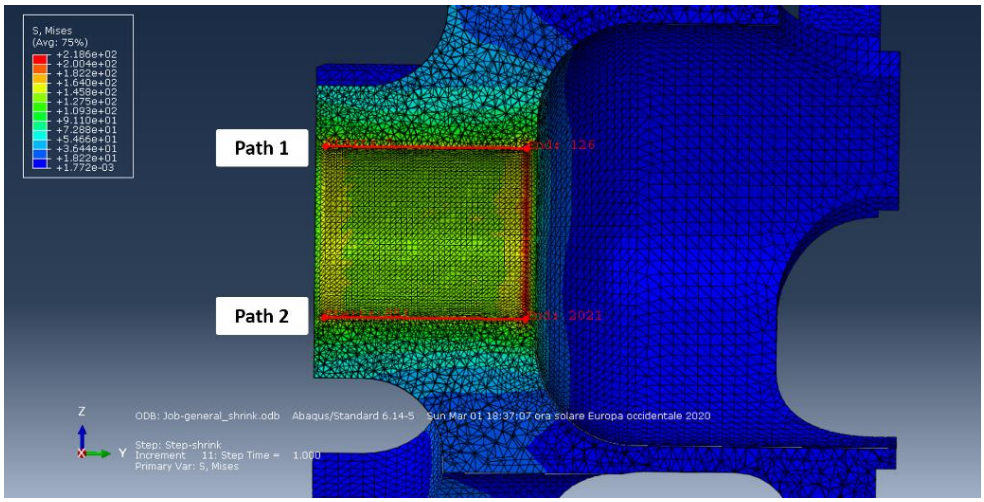

Figure 5.44 – Paths

In *Figure 5.45* is presented the plot of *contact pressure* (blue), *hoop stress* (red) and *Von-Mises stress* (black); *1* and *2* means the phat used. On abscissa is represented the distance along the contact, starting from the most external point.

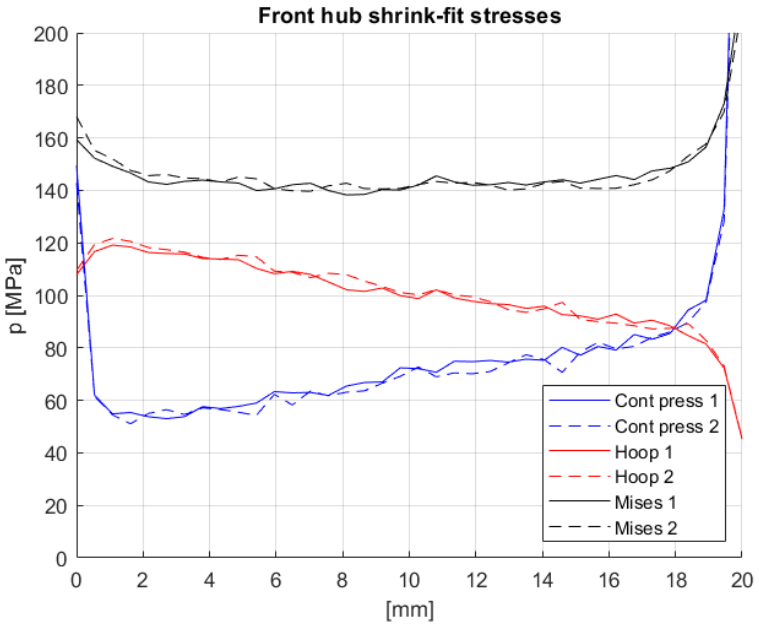

Figure 5.45 – Front hub shrink-fit stresses

Table 5.20 – Analytic and FEM results comparison

Stress	Analytic result	FEM result
Contact pressure	53.99 ÷ 72.52 MPa	53 ÷ 98 MPa
Hoop stress	110.5 ÷ 93.33 MPa	120 ÷ 82 MPa
Von-Mises	145.2 ÷ 144 MPa	150 ÷ 147 MPa

In *Table 5.20* analytic and FEM results are compared: first and last values obtained from FEM were discarded, since, as visible in the plot, we have a stress rise in those region and would be meaningless compare them to the analytic values.

The first values in the table are the ones at the beginning on the contact length (1-2 mm), the second ones are taken between 18-19 mm. The detectable differences for the second values are mainly due to the difficult to take a correct diameter for the analytic calculations, since in that region there's the presence of the wheel supports.

Anyway, since the Von-Mises stress are small than the yield stress, with a safety coefficient $\eta = \frac{240}{150} = 1.6$, the failure resistance is verified.

5.5.2 Characteristic angles variation

The focus of this section is to calculate the variation of camber and toe due to the deformation of the system composed by front axle and hub: these are evaluated with a FEM model to which only one contact force at time is applied. To the angles found in this way is applied the superimposition principle to find the characteristic angles for each load case.

The model used differs from the shrink-fit one in the following three aspects:

- Shrink-fit interaction: rather than surface to surface contact, since we for this analysis we are not interested in stresses, it was set as tie constraint, allowing an easier and faster computation of the deformations
- Step: automatic stabilization was disabled, since it was needed only because of the shrink-fit contact interaction
- Mesh type: the simpler analysis of the tie with respect to the contact, made possible the use of quadratic tetrahedral elements (C3D10) instead of the linear ones, thus improving the result

For each analysis only one contact force was considered, with a value of 100 N: in this way it is possible to calculate the deflection under race loads simply applying the effects superimposition:

$$\theta_{race} = \sum_i \theta_{F_i=1N} \cdot F_{i,race} = \sum_i \frac{\theta_{F_i=100N}}{100} F_{i,race}$$

The reason why was not used a unitary force of 1 N for the analysis is because such a small value could give rise to some numerical error, thus reducing the precision of the evaluation, while the chosen value of 100 N has the same order of magnitude of the real forces.

Longitudinal, lateral and vertical load are applied to the wheel with their respective transportation moments and, for the longitudinal one, there are also the reaction forces of the brake. For each force was created two relative rotated load cases (0° and 90°), to consider the non-symmetry of the rotating system (i.e. supports and, for the rear hub, presence of keyseats on the rear axle), which create different deflection: then the two values found for toe and camber are then averaged. The values are reported in *Table 5.21*.

Table 5.21 – Single contact force loads

	F_{long} 0°	F_{long} 90°	F_{lat} 0°	F_{lat} 90°	F_{vert} 0°	F_{vert} 90°
F_x	100 N	0	0	0	0	-100 N
F_y	0	0	100 N	100 N	0	0
F_z	0	100 N	0	0	100 N	0
M_x	0	4600 Nmm	27900 Nmm	0	4600 Nmm	0
M_y	-27900 Nmm	-27900 Nmm	0	0	0	0
M_z	-4600 Nmm	0	0	27900 Nmm	0	4600 Nmm
$F_{x,brake}$	-59.84 N	363.4 N	0	0	0	0
$F_{z,brake}$	-363.4 N	-59.84 N	0	0	0	0

Race condition loads (section *3.3.2*) were considered for this analysis.

In *Table 5.22* are presented the results of the deflections, comparing the angles obtained for the original system to the new one; angles are expressed in thousands of degrees to be clearer.

Table 5.22 – Front hub angle deflection (in thousandths of degrees)

	Original [1E-3°]			New [1E-3°]			Variation [1E-3°]		
Load	Camber	Toe	Torsion	Camber	Toe	Torsion	Camber	Toe	Torsion
Fx = 100 N	-15.42	-2.90	-4.08	-22.80	-4.64	-13.76	-7.38	-1.74	-9.68
Fy = 100 N	103.61	0	0	135.61	0	0	32.00	0	0
Fz = 100 N	5.44	0	0	8.39	0	0	2.95	0	0
Weigth	21.77	0	0	33.58	0	0	11.81	0	0
Curve ext	150.67	0	0	203.36	0	0	52.69	0	0
Curve int	-107.13	0	0	-136.21	0	0	-29.07	0	0
Braking	1.27	-4.64	-6.54	3.54	-7.42	-22.02	2.27	-2.78	-15.49

Can be notice that the worst camber variation, obtained in correspondence of the outer wheel, are not negligible (0.2°) also if the variation with respect to the original hub is very small (1/20 of degree): this is mainly due, as already said in section *5.2.1*, is due to the small external diameter, a basic problem that was not possible to solve. Anyway, since the difference to the original system is very small, the obtained results are acceptable.

5.6 Rear Hub

The rear hub has been redesigned in the same way of the front one, so we focus on the main differences.

The biggest difference between front and rear hubs is the position of the brake disc: while on the front it is directly bolted on the hub, on the rear it is fixed on the axle, giving to the hub a much more simple geometry (*Figure 5.46*). In this case the shrink fit must also sustain the braking torque.

Material, internal diameter and wheel screws positions are the same for both the hubs.

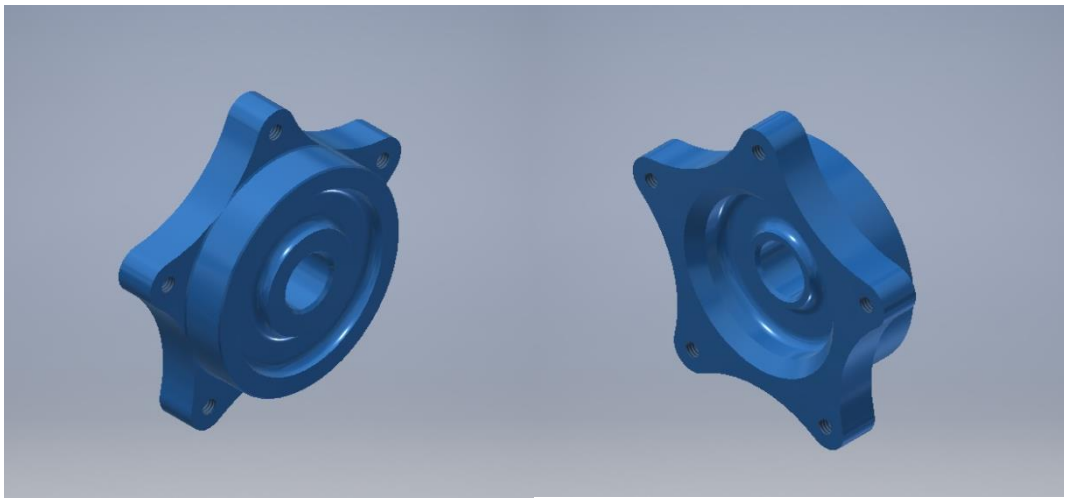

Figure 5.46 – Rear hub

5.6.1 Basic topology optimization

The design space is defined by the constraints of:

- Length of the threated part: as for the front hub, it was initially decided to maintain a length of 12 mm to avoid unscrewing due to vibration, but then it was possible to reduce it to 10 mm for the preliminary design
- Wheel centering: again, it has an external diameter of 69 mm and a length of 13 mm
- Position of the wheel bolts (five M6 on a diameter of 86 mm)

In *Figure 5.47* can be seen how the geometry is much more simple than the one of the front hub.

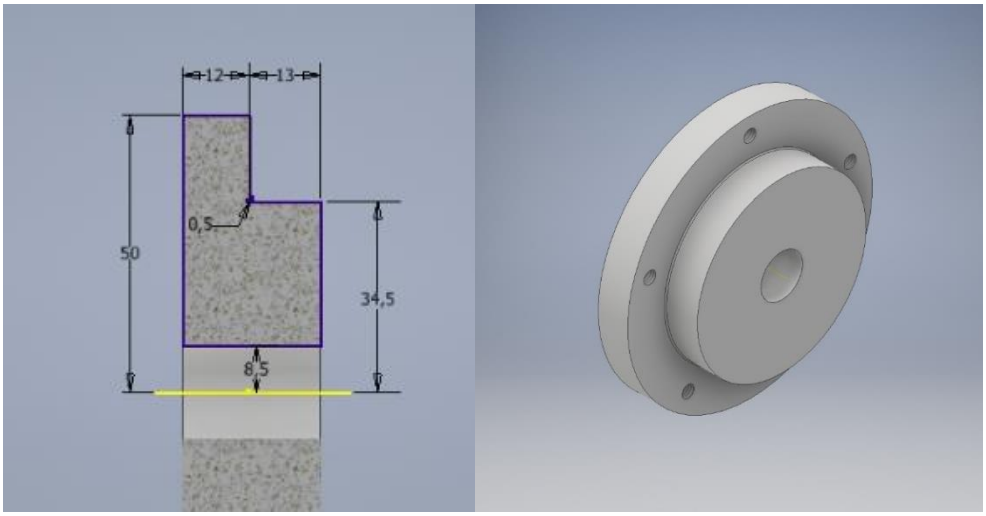

Figure 5.47 – Rear hub design space

The CAD model was then imported in *Altair Inspire* for the topology optimization, creating the partition for the threated holes, wheel centering and inner diameter. As for the front hub, to apply forces and moments on the bolted connection was created a point then rigidly connected to interface of hub and rim (*Figure 5.48*). Differently instead at the inner diameter all the degrees of freedom are constrained, axial rotation included.

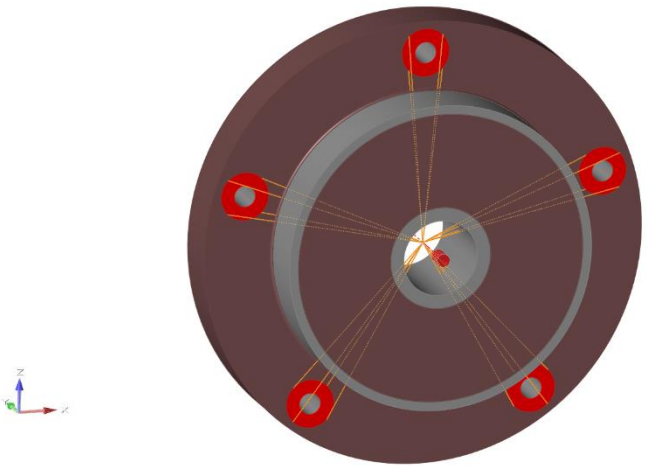

Figure 5.48 – Connections

To obtain better results is applied cyclic shape control with 5 planes of symmetry (one for each bolt), as shown in *Figure 5.49*.

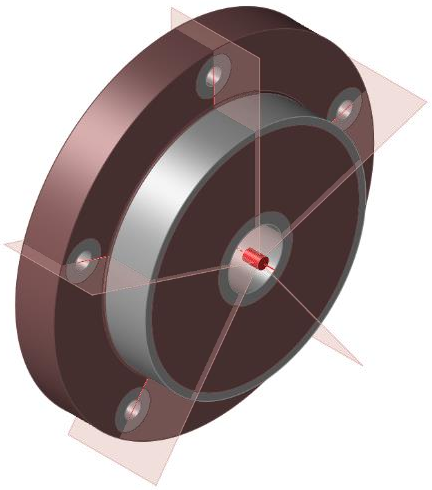

Figure 5.49 – Shape control

Only two load cases were needed (differently from the four of the front hub, due to the absence of the brake disc): they represent the case of braking in curve with a relative rotation of 90° and the forces considered are the usual design loads, so the difference to the front ones is the direction of the longitudinal force (*Table 5.23*).

Table 5.23 – Rear hub design loads

Design	F_x	F_y	F_z	M_x	M_y	M_z
Loads 0°	-400 N	400 N	1200 N	-	-	-
Loads 90°	-1200 N	400 N	-400 N	-	-	-
Wheel forces and moments						
Load case 0°	-400 N	400 N	1200 N	166800 Nmm	111600 Nmm	18400 Nmm
Load case 90°	-1200 N	400 N	400 N	-18400 Nmm	111600 Nmm	166800 Nmm

The topology optimization was based on the maximum stiffness research, with a target mass of 30%, in the same way of the front hub, obtaining the geometry in *Figure 5.50*, *Figure 5.51* and *Figure 5.52*.

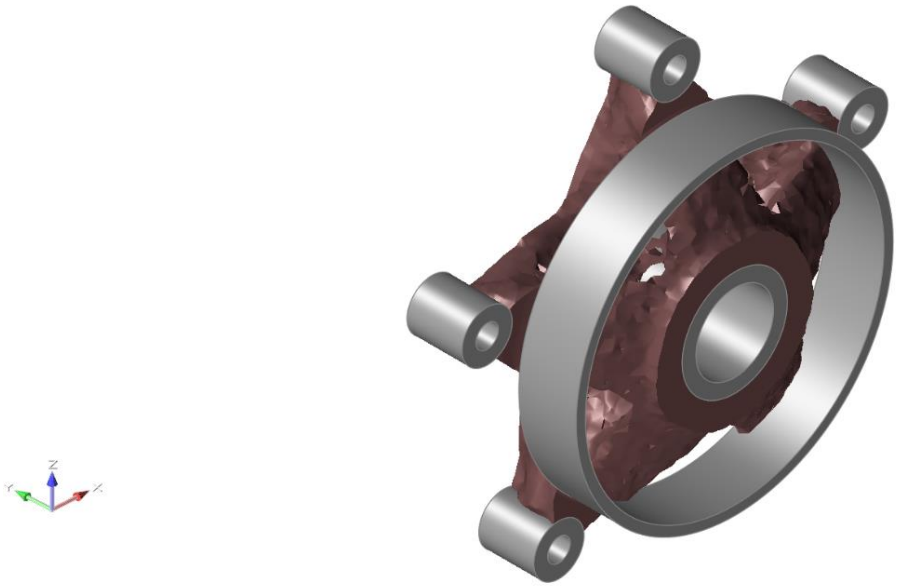

Figure 5.50 – Result of the stiffness maximization, isometric front view

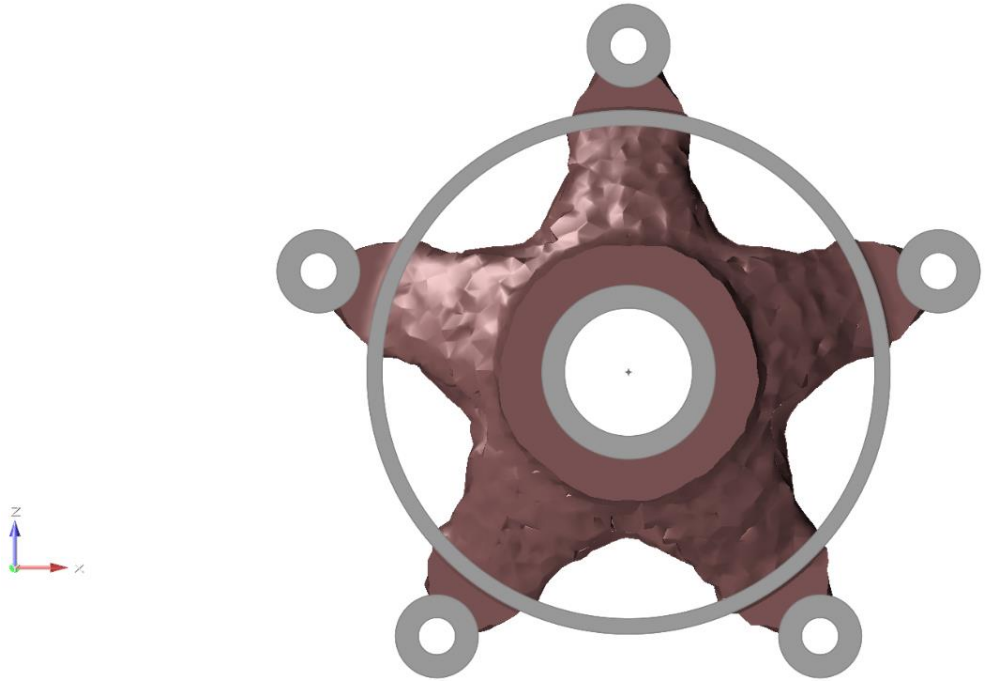

Figure 5.51 – Result of the stiffness maximization, front view

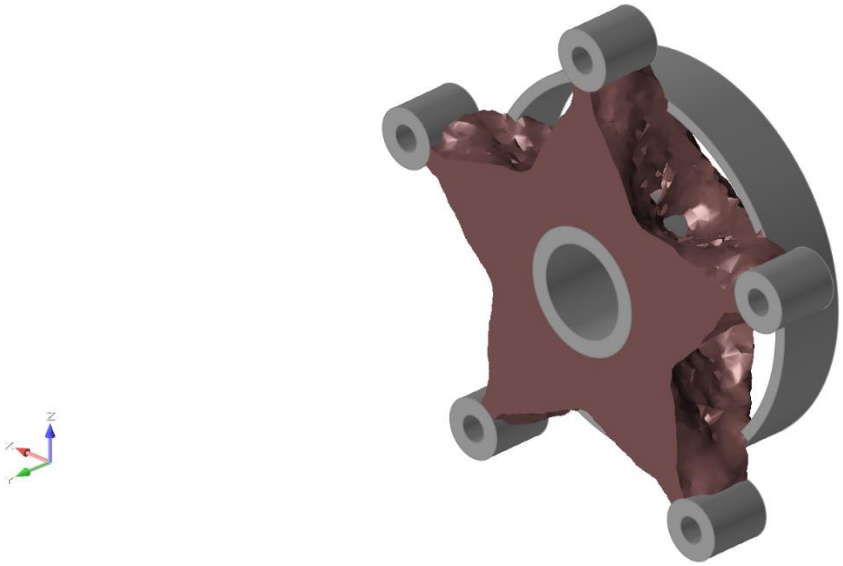

Figure 5.52 – Result of the stiffness maximization, isometric rear view

As for the front hub, the optimization gives as result a star shape, this time more visible thanks to the simpler geometry. Can be also notice the thickness increasing from the screws to the centre.

5.6.2 Preliminary design

The preliminary design takes up the concept of the front hub: the material between the hubs has been resected to obtain the desired star shape, leaving one shelf at each wheel support for the centering. The length of the threated section, as mentioned, was reduced to 10 mm too.

The relative inclination of the front and rear face of the support give the thickness enlargement from the top to the centre.

Figure 5.53 and *Figure 5.54* show dimensions and geometry of the preliminary design.

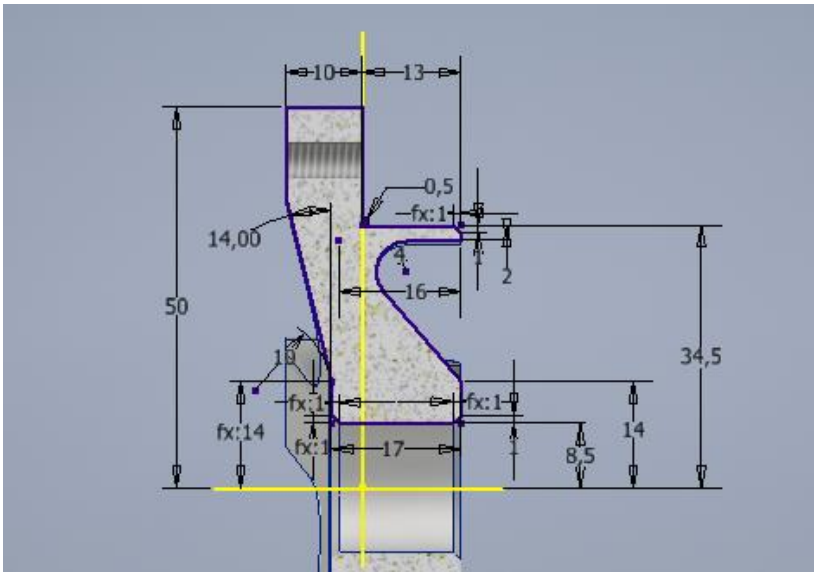

Figure 5.53 – Preliminary design dimensions

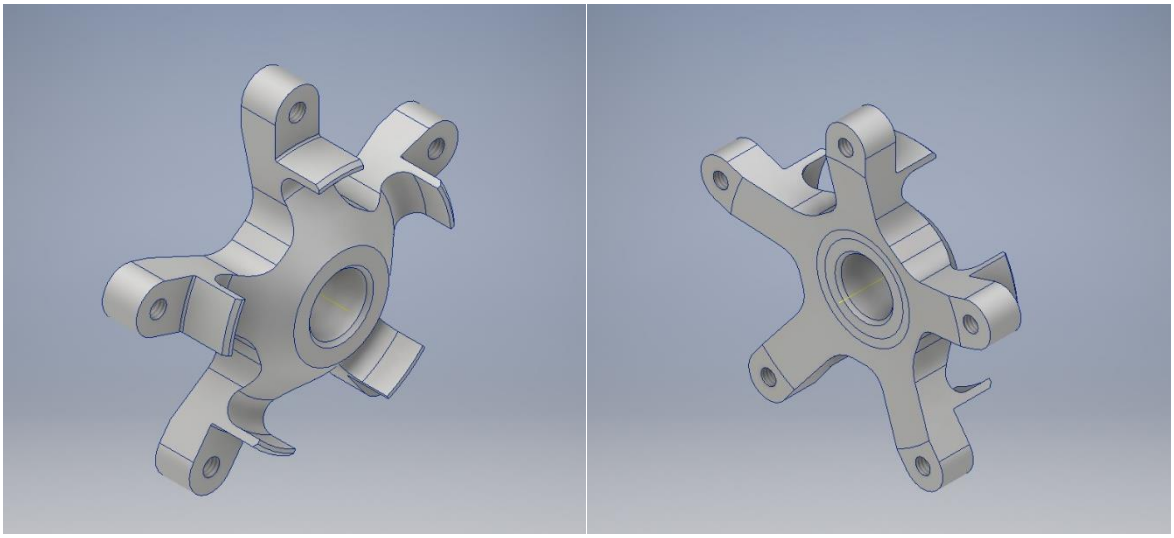

Figure 5.54 – Preliminary design, front and rear isometric view

The design was subjected to a preliminary FEM analysis.

The main differences of this model with respect to the front hub are:

- the absence of the brake disc reference point (in *Figure 5.55* are pictured the kinematic coupling of wheel and inner diameter)
- since the braking torque is transmitted by the shrink-fit, in the correspondent reference point also the torsion constrained.

In *Figure 5.56* are indicated the most stressed region with their values.

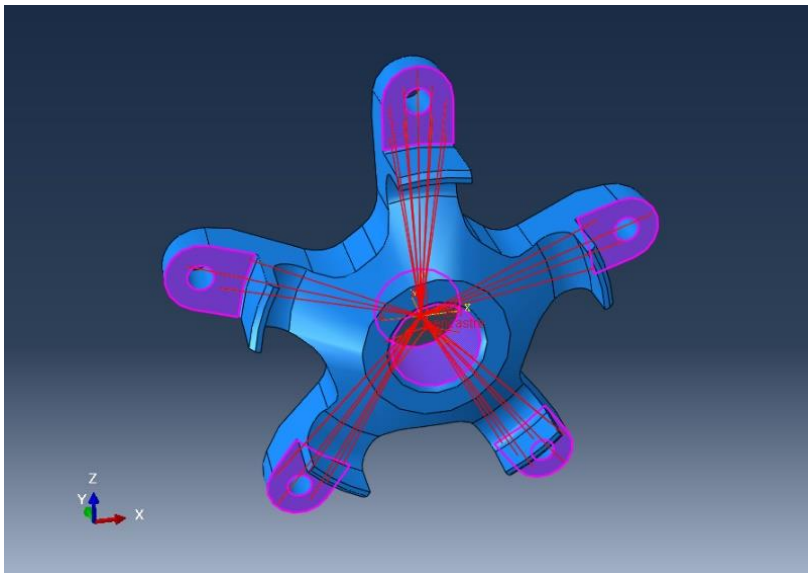

Figure 5.55 – Couplings

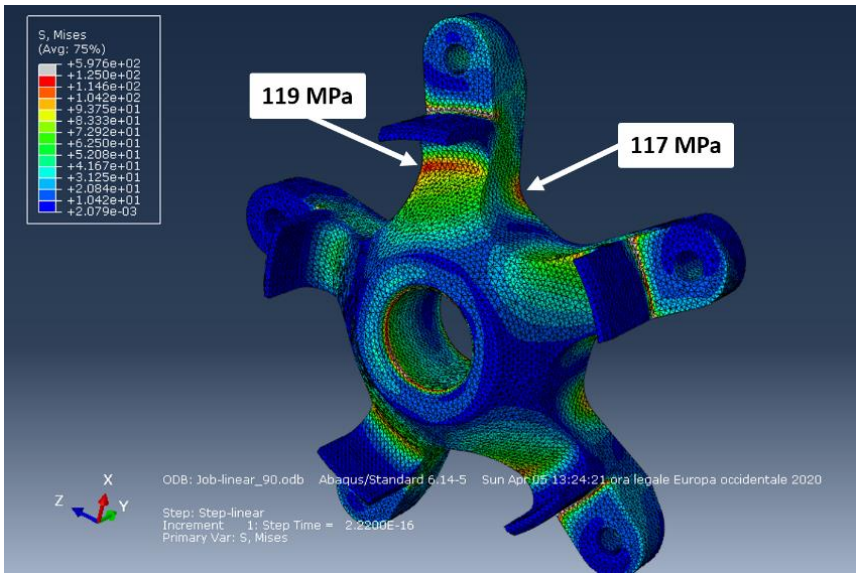

Figure 5.56 – Stresses

Since no over-stressed region are present, we can procced with the optimization (also in this case the shrink-fit is later discussed).

5.6.3 Shape optimization

Considering the analogy between support and a cantilever beam described in section *5.4.3*, the chosen parameters [8] [9] are:

- Top thickness (*Figure 5.57*): increase the thickness near the bolted connection; differently from the front hub it doesn't change the thickness near the centre, so this parameter could be less effective. It is defined as showed in *Figure 5.57*, analysing the case of 7 mm (base case) and 8 mm (+1 mm).

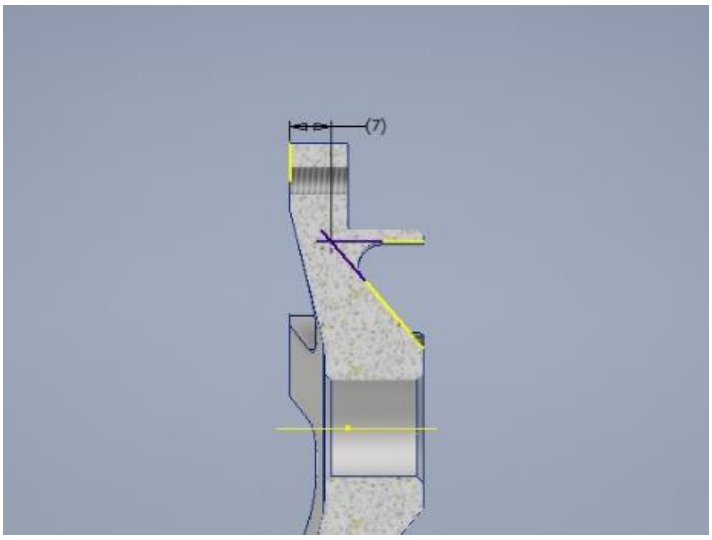

Figure 5.57 – Thickness parameter

- Angle between lateral faces of the supports (*Figure 5.58*): this parameter allows the width to increase from the tip to the base, where stresses are bigger. The sensitivity analysis is done for parallel faces (0°, base case) and 10°.

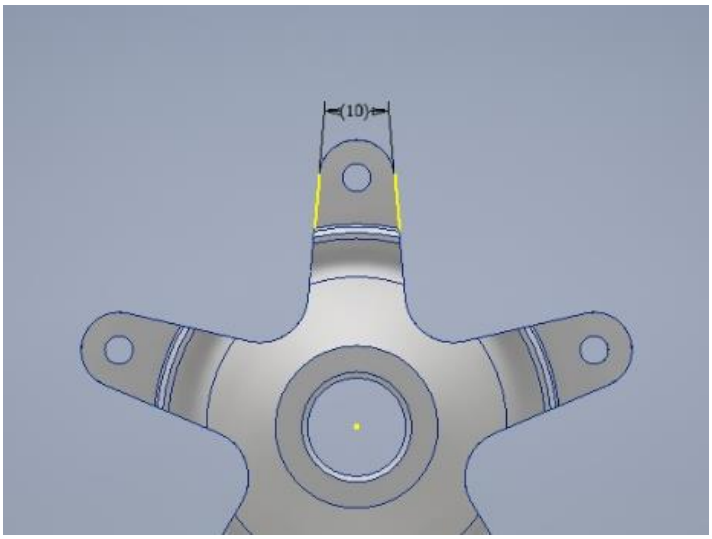

Figure 5.58 – Angle parameter

Applying a single unitary moment of 1 Nm for each analysis, following the procedure already used for the front hub in chapter *5.4.3*, we find bending and torsional stiffness for the rear hub. *Table 5.24* shows the results, whit the normalized values and percentage variations too.

Table 5.24 – Rear hub sensitivity analysis

	Base	+ 1 mm	+ 10°
Mass [g]	97.00	100.00	105.00
Inertia [kgm^2]	72.80	73.84	79.19
Bending stiffness [Nm/°]	1652.4	1750.4	1872.1
Torsional stiffness [Nm/°]	3433.6	3529.9	4050.1
Variance %			
Mass	-	3.09%	8.25%
Inertia	-	1.42%	8.77%
Bending stiffness	-	5.93%	13.30%
Torsional stiffness	-	2.80%	17.95%
Normalized by mass			
Inertia [kgm^2/g]	0.751	0.738	0.754
Bending stiffness [Nm/°/g]	17.035	17.504	17.829
Torsional stiffness [Nm/°/g]	35.398	35.299	38.572
Variance %			
Inertia	-	-1.62%	0.49%
Bending stiffness	-	2.75%	4.67%
Torsional stiffness	-	-0.28%	8.97%

In *Table 5.25* are instead reported stiffness variation normalized by mass variation for optimization purposes.

Table 5.25 – Variations ratios

	+ 1 mm	+ 10°
Inertia [kgm²/g]	0.346	0.798
Bending stiffness [Nm/°/g]	32.676	27.465
Torsional stiffness [Nm/°/g]	32.092	77.059
Variance %		
Inertia	-53.9%	6.4%
Bending stiffness	91.8%	61.2%
Torsional stiffness	-9.3%	117.7%

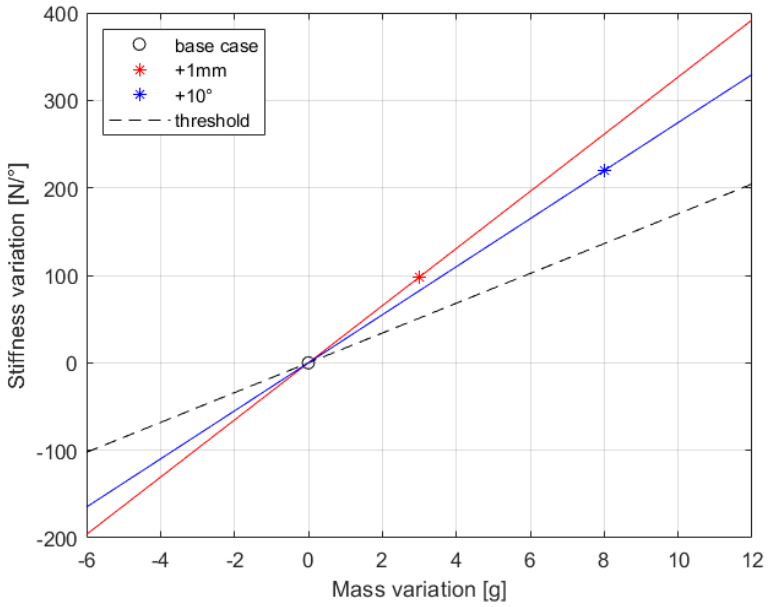

Figure 5.59 – Stiffness-mass variation diagram

From these results some differences can be seen between front and rear hub:

- Thickness: as hypnotized before, it is way less advantageous for the rear hub (32.7 instead of 52.7÷56 Nm/°/g)
- Angle: this parameter is instead twice more effective than at the front (27.5 rather than 15 Nm/°/g), probably this fact is related to the greater length of the wheel support for the rear hub

These differences make the two option more comparable and even if the thickness variation is still better, increasing the angle allows to effectively increase also the torsional stiffness. It was then decided to set an angle of 10.6°, since it allows to use a single corner radius between two support, thus simplifying the definition of the geometry.

To define the stiffness target was decided to maintain the maximum camber variation between 25 and 30 thousandths of degrees. Forces and moments acting on the rear hub are shown in *Table 5.26*.

Table 5.26 – Rear hub race loads

	weight	braking	Internal curve	External curve
F_x	0	-160 N	0	0
F_y	0	0	-120 N	120 N
F_z	400 N	323.3N	301.2 N	498.8 N
Transportation moments				
M_x	18400 Nmm	14871 Nmm	-19626 Nmm	56426 Nmm
M_y	0	44640 Nmm	0	0
M_z	0	7360 Nmm	0	0

The maximum bending is again obtained for the external wheel during curve, so the target stiffness in calculated as

$$K_{\theta,target} = \frac{M}{\theta} = \frac{56.426\ Nm}{0.0275°} = 2051.9 \rightarrow 2000\ Nm/°$$

To calculate the thickness needed to reach the target we can proceed as follow:

$$k_{angle} = \frac{stiffness}{angle} = \frac{K_{\theta,10°} - K_{\theta,base}}{10°} = 21.97\ Nm/°/°$$

$$k_{thick} = \frac{stiffness}{thickness} = \frac{K_{\theta,+1mm} - K_{\theta,base}}{1\ mm} = 98\ Nm/°/mm$$

$$K_{\theta,target} = K_{\theta,base} + k_{angle} \cdot 10.6° + k_{thick} \cdot \Delta t \quad \rightarrow \quad \Delta t = 1.16\ mm \rightarrow 1\ mm$$

With these values the expected bending stiffness for the rear hub is 1984 Nm/°, with a torsional stiffness of 4186 Nm/° and a mass of 108.5 g. *Table 5.27* shows CAD and the FEA results.

Table 5.27 – Rear hub results

	Original	Preliminary	Final
Mass [g]	216.00	97.00	108.00
Inertia [kgm^2]	195.32	72.80	80.91
Bending stiffness [Nm/°]	2759.17	1652.4	2004.3
Torsional stiffness [Nm/°]	5634.80	3433.6	4197.6
Variance %			
Mass	-	-55.09%	-50.00%
Inertia	-	-62.73%	-58.58%
Bending stiffness	-	-40.11%	-27.36%
Torsional stiffness	-	-39.06%	-25.51%
Normalized to the mass			
Inertia [kgm^2/g]	0.904	0.751	0.749
Bending stiffness [Nm/°/g]	12.774	17.035	18.558
Torsional stiffness [Nm/°/g]	26.087	35.398	38.867
Variance %			
Inertia	-	-17.00%	-17.15%
Bending stiffness	-	33.35%	45.28%
Torsional stiffness	-	35.69%	48.99%

We can see from the positive values of the normalized percentage variance of the stiffness that the new hub is more efficient than the original: since the rear hub was less thick with respect to the front one and presents a simpler geometry, was possible to optimize the shape redistributing better the material without the necessity to decrease the thickness, which has high importance for the stiffness.

5.7 Rear hub and axle interaction

Is now necessary to verify the shrink-fit and the characteristic angles variation due to axle and hub assembly, repeating the same procedures used for the front system (chapter *5.5*).

5.7.1 Shrink-fit

Front and rear system have in common:

- Materials
- Tolerances
- Diameter of the shrink-fit

Unlike the front one, at rear we have a solid axle: in this case the equation for stress in a disc, due to different boundary conditions, give a different solution for hoop and radial stresses of the shaft that, at the external diameter, takes the values:

$$\begin{cases} \sigma_{\theta,S} = -p \\ \sigma_{r,S} = -p \end{cases}$$

where you remember p is the contact pressure. The relation between interference and contact pressure then became:

$$p = \frac{i}{D}\left(\frac{a_H^2 + \nu_H}{E_H} + \frac{1 - \nu_S}{E_S}\right)^{-1}$$

Table 5.28 reports the data required to calculate the shrink-fit stresses.

Table 5.28 – Shrink-fit data

Hub	
D_{ext}	~50 mm
Tolerance: S7	-21 ÷ -39 µm
E (aluminium)	70 GPa
v (aluminium)	0.33
Axle (shaft)	
Tolerance: h6	0 ÷ -11 µm
E (steel)	206 GPa
v (steel)	0.3
Interference	
Minimum	10 µm
Maximum	39 µm
D	17 mm
Contact length	17 mm
μ_s steel-aluminium	0.61

Another difference between front and rear hub is the transmission of the braking force: since in this case the brake disk is mounted on the axle, the shrink-fit must sustain not only the lateral force, but also the braking torque. The transmissible torque is calculated as the integral of the circumferential shear on the contact surface, multiplied by the moment arm, correspondent to the radius of the shaft:

$$T = \int_0^{2\pi} \tau_T \left(L \frac{d}{2} d\theta \right) \frac{d}{2} = \frac{L \tau_T \pi d^2}{2}$$

$$\tau_T = \frac{2M_y}{L\pi d^2}$$

Remembering that

$$\tau_{ax} = \frac{F_y}{\pi L d}$$

it is finally possible to find the minimum contact pressure required to guarantee the transmission of the forces; considering the design load ($F_y = 400\ N$, $M_y = 111600\ Nmm$), we obtain

$$p_{min} = \frac{\tau}{\mu_s} = \frac{\sqrt{\tau_{ax}^2 + \tau_T^2}}{\mu_s} = 18.33\ MPa < p_{i,min} = 22.51\ MPa$$

The connection is verified since the required pressure is smaller than the one obtained for the minimum interference.

Stresses (hoop, radial and Von-Mises) are calculated in the same way of the front hub, for the maximum possible interference (39 µm); *Table 5.29* shows the results.

Table 5.29 – Shrink fit results

Failure resistance	
Contact pressure	87.79 MPa
Hub	
Hoop stress	110.7 MPa
Radial stress	-87.79 MPa
Von-Mises stress	172.3 MPa
Axle	
Hoop stress	-87.79 MPa
Radial stress	-87.79 MPa
Axial stress	417.8 MPa
Von-Mises stress	505.6 MPa

The higher stress of the hub respect to the front one is due to the solid axle since it deforms less.

Obtained analytic result must be compared to the FEM analysis: the model was created following the same procedures for the front one (section *5.5.1*).

Axle was in this case created in *Inventor* and then imported in *Abaqus*, partitioning it for bearings and shrink-fit surfaces definition and coupling (*Figure 5.60*).

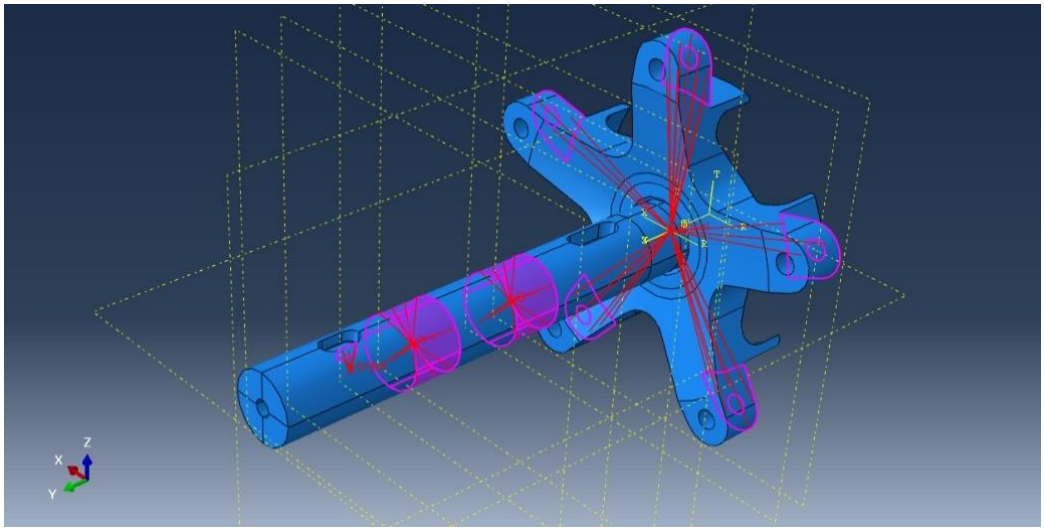

Figure 5.60 – Rear hub couplings

In particular, braking torque is transmitted from disc to the axle by a key: to simulate this interaction the lateral surface of the keyhole was kinematic coupled with the reference point, created on the shaft axis in correspondence of the brake disc, as visible in *Figure 5.61*.

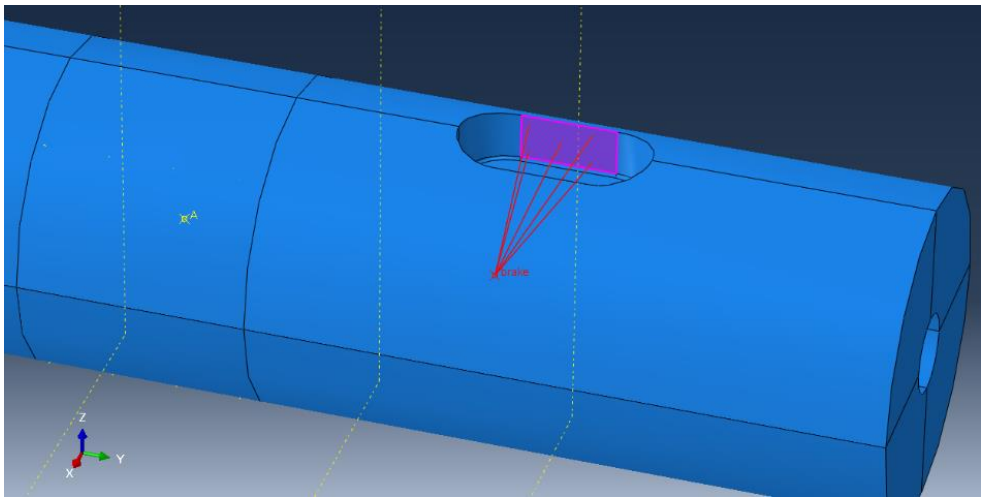

Figure 5.61 – Detail of the brake disc coupling

Constraints and mesh definitions are the same of the front system.

Figure 5.62 shows the two paths used to plot the data of contact pressure, hoop stress and Von-Mises stress (*Figure 5.63*). *Table 5.30* compare analytic and FEM results.

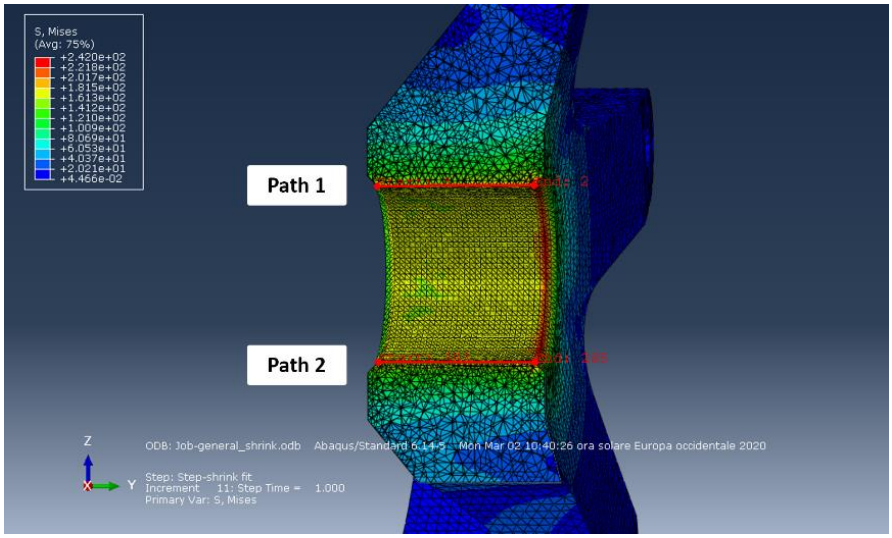

Figure 5.62 – Paths

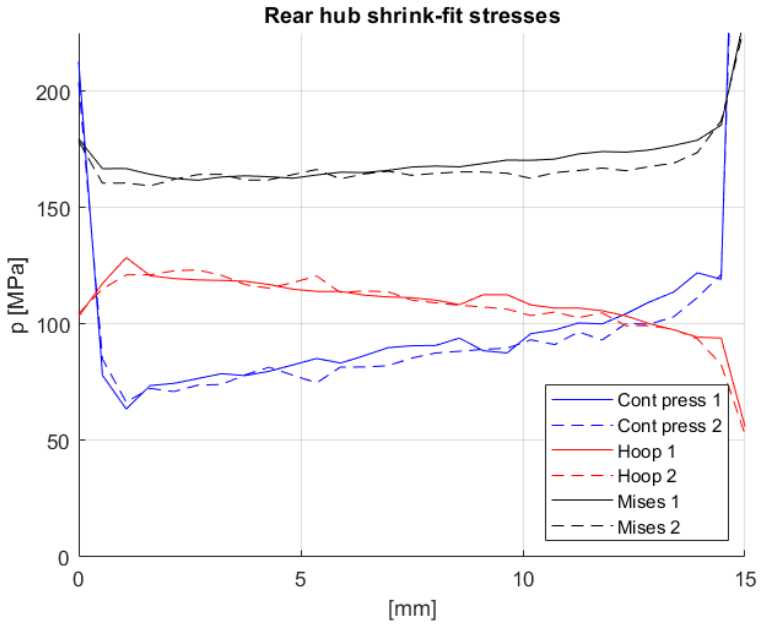

Figure 5.63 – Rear hub shrink-fit stresses

Table 5.30 – Analytic and FEM results comparison

Stress	Analytic result	FEM result
Contact pressure	87.79 MPa	67 ÷ 118 MPa
Hoop stress	110.7 MPa	124 ÷ 93 MPa
Von-Mises	172.3 MPa	167 ÷ 176 MPa

Also in this case, differences in the results are due to the non-constant value of the diameter of the hub. Anyway, values found are comparable.

The stress is higher for the rear hub, but still allowed with a safety factor $\eta = \frac{240}{176} = 1.36$.

5.7.2 Characteristic angles variation

Displacements are calculated in the same way explained in section *5.5.2*.

The only difference is the brake force due to different disc radius ($r_{brake} = 45\ mm$) and angle of the brake pad ($\theta_{brake} = 90.8°$), defined as in *Figure 5.7*.

Table 5.31 shows the braking force to apply at the reference point for the case of $F_{long} = 100\ N$.

Table 5.31 – Brake forces

	F_{long} 0°	F_{long} 90°
F_x	100 N	0
F_z	0	100 N
$F_{x,brake}$	-9.09 N	619.9 N
$F_{z,brake}$	-619.9 N	-9.09 N

Race condition load related to the rear wheel are applied. Results are summarized in *Table 5.32*.

Table 5.32 – Rear hub deflections (in thousandths of degrees)

	Original [1E-3°]			New [1E-3°]			Variation [1E-3°]		
Load	Camber	Toe	Torsion	Camber	Toe	Torsion	Camber	Toe	Torsion
Fx = 100 N	1.96	-9.76	-1744	1.97	-10.47	-1885	0.01	-0.71	-141.33
Fy = 100 N	115.61	0	0	120.64	0	0	5.03	0	0
Fz = 100 N	9.73	0	0	10.45	0	0	0.71	0	0
Weigth	37.60	0	0	40.45	0	0	2.85	0	0
Curve ext	222.57	0	0	233.47	0	0	10.90	0	0
Curve int	-147.37	0	0	-152.57	0	0	-5.20	0	0
Braking	34.47	15.61	2791	37.30	16.75	3017	2.83	1.14	226.13

With respect to the front system, variation between original and new design are smaller because in this case they are due to the hub only, since the axle has not been modified.

Torsion angles are big (3°): since hub and brake are positioned on the opposite site of the axle, it twists along its entire length. Anyway, since this parameter doesn't influence the efficiency of the vehicle during the race, this result is acceptable.

6 Conclusions

The purpose of this thesis work was the lightweight design of components of a high efficiency vehicle for the Shell Eco-marathon competition. In particular, the work concerned:

- Suspension supports: the component is designed as a tube made from Al 7075 T6, fixed to the chassis with two clamps. The suspension arm is mounted on the tube. First the component is designed in order to avoid structural failure, then deformations and the corresponding wheel angles variations are evaluated. The final design is compliant with the constraints of structural strength and maximum allowable wheel angles variation. Finally a static assessment of the component with the aid of FE method is carried out.
- Front axle: the part is a tube made from 39NiCrMo4 mounted on two angular contact ball bearings and shrink-fitted to the hub. First the maximum allowable internal diameter is evaluated according to failure constraints. The component is designed by solving a minimum mass optimization problem with constraints the maximum allowable internal diameter and the maximum allowable wheel angles variation.
- Hubs: made of aluminium 6061-T6, they are shrink-fitted to the axles and connected to the wheel rims by means of a bolted coupling. The design process consists in a topology and shape optimization: first the design space was defined and subjected to minimum mass and maximum stiffness topology analysis. Based on the obtained result, a preliminary design was defined and assessed with a FE analysis. The desired stiffness was then obtained with the shape optimization, which consists in the definition of appropriate design variables and, after the analysis of their contribution to the deformation, in the choice of their values. Finally, shrink-fit stresses and hubs deformations under race loads were evaluated.

In the next tables are shown the main results of this thesis work:

- *Table 6.1*: reports the mass of each component and the saved mass with respect to the original ones. The percentage reduction is expressed first respect to the original parts and then to the overall mass of the vehicle.
- Table 6.2 and Table 6.3: total toe and camber angles variation due to the superimposition of the designed components (suspension support, axle, hub). Is also tabulated the variation with respect to the original parts, showing very small variations with maximum deviations of ±0.04°.

Table 6.1 – Mass

	Mass	Reduction	Reduction %	Overall %
Tubes (x4)	100 g	-410 g	-80.4%	-1.82%
Front axle (x2)	136.6 g	-72.3 g	-34.6%	-0.16%
Front hub (x2)	164 g	-169 g	-50.75%	-0.38%
Rear hub (x2)	108 g	-108 g	-50%	-0.24%
Total	1434 g	-2338.6 g	-65.75%	-2.60%

Table 6.2 – Camber and toe angles variation at front

[1e-3°]	weight	braking	Internal curve	External curve
Toe	1.10	-0.92	7.90	-5.70
Toe variation	0.88	2.42	6.20	-4.50
Camber	20.58	-11.96	-150.11	191.26
Camber variation	1.51	-10.03	-40.07	43.09

Table 6.3 – Camber and toe angles variation at rear

[1e-3°]	weight	braking	Internal curve	External curve
Toe	10.10	29.95	-0.52	20.80
Toe variation	8.00	11.64	-0.41	16.40
Camber	27.75	27.10	-166.17	221.97
Camber variation	-7.05	-5.17	-16.00	1.80

Appendix

In the following pages, technical drawings of mechanical components described in previous chapters are collected.

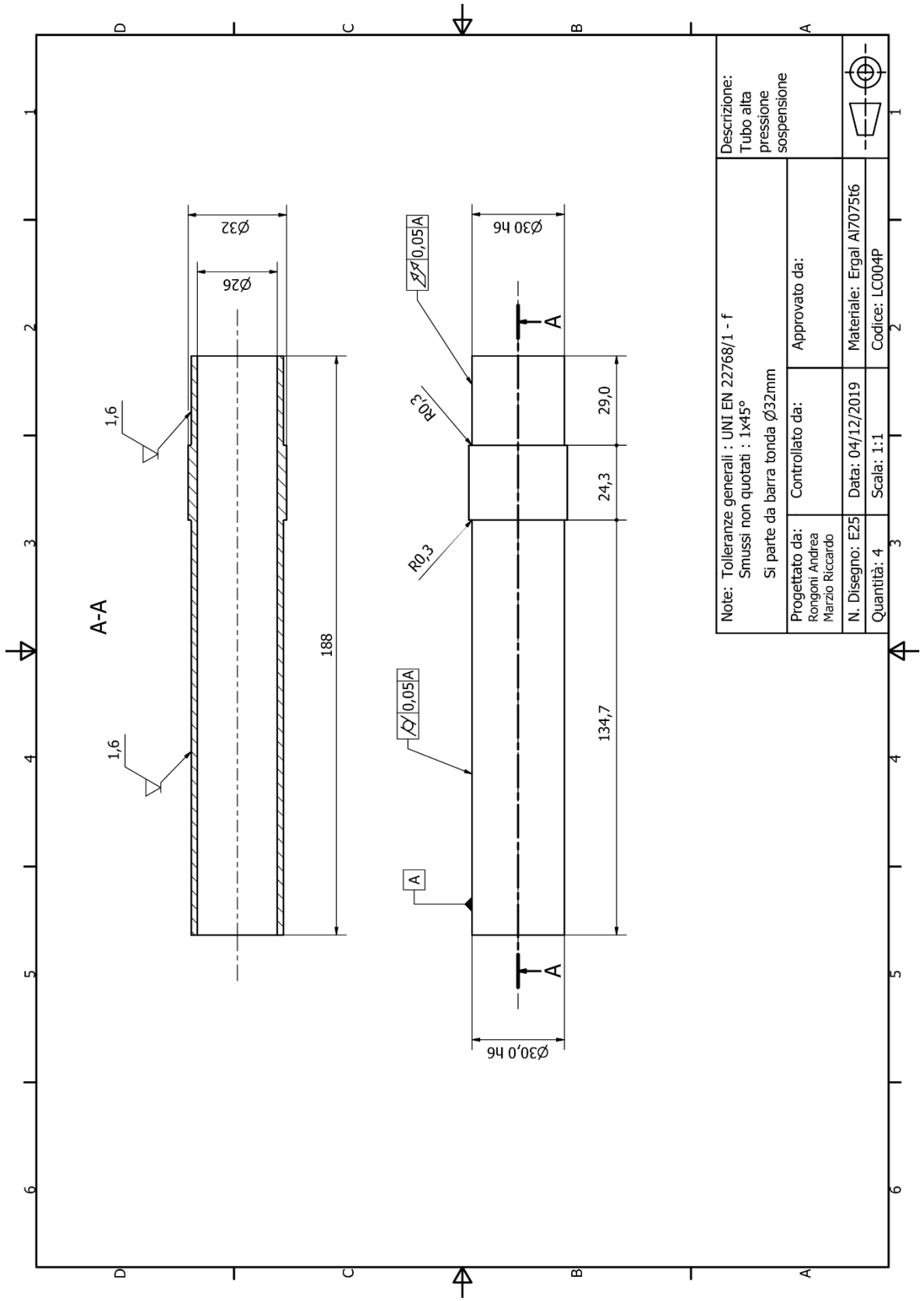
A-A
Ø32
Ø26
188
1,6
1,6
Ø30 h6
Ø30,0 h6
0,05 A
R0,3
R0,3
29,0
24,3
134,7
A
A
A
Note: Tolleranze generali : UNI EN 22768/1 - f
Smussi non quotati : 1x45°
Si parte da barra tonda Ø32mm
Descrizione: Tubo alta pressione sospensione
Progettato da: Rongoni Andrea Marzio Riccardo
Controllato da:
Approvato da:
N. Disegno: E25
Data: 04/12/2019
Materiale: Ergal Al7075t6
Quantità: 4
Scala: 1:1
Codice: LC004P

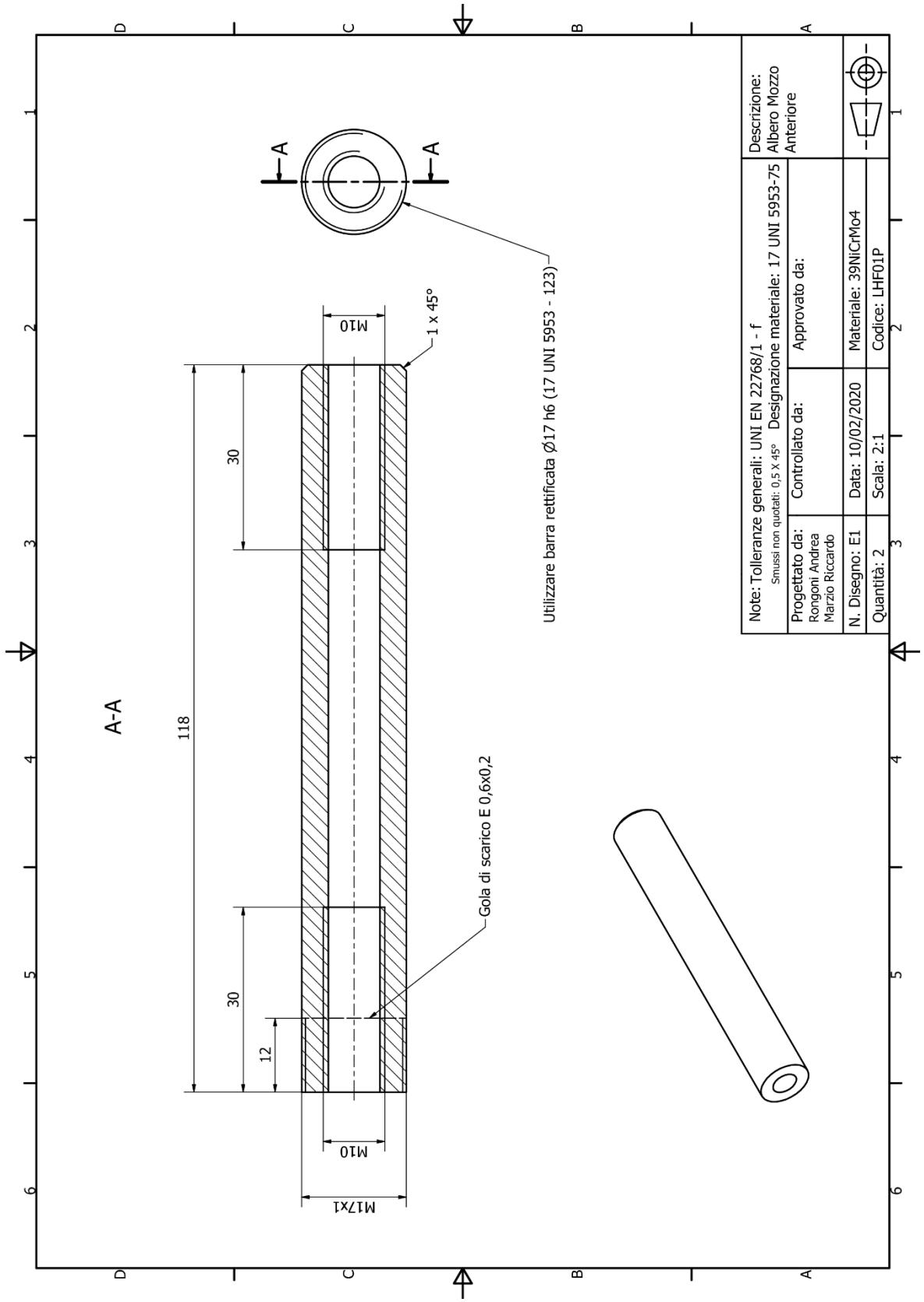
A-A
A
A
M10
1 x 45°
30
118
30
12
M10
M17x1
Gola di scarico E 0,6x0,2
Utilizzare barra rettificata Ø17 h6 (17 UNI 5953 - 123)
Note: Tolleranze generali: UNI EN 22768/1 - f
Smussi non quotati: 0,5 X 45° Designazione materiale: 17 UNI 5953-75
Progettato da: Rongoni Andrea Marzio Riccardo
Controllato da:
Approvato da:
N. Disegno: E1
Data: 10/02/2020
Materiale: 39NiCrMo4
Quantità: 2
Scala: 2:1
Codice: LHF01P
Descrizione: Albero Mozzo Anteriore

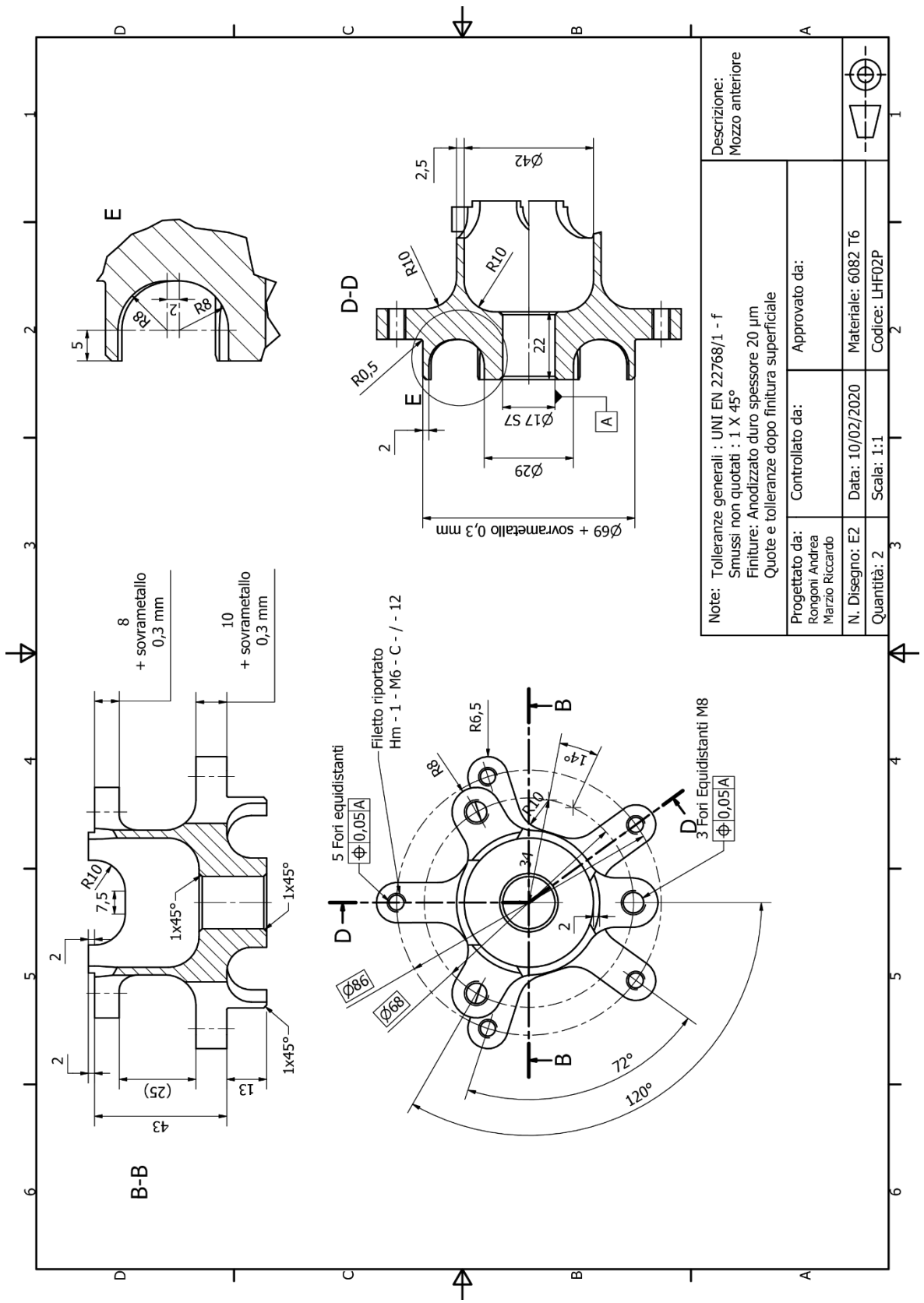
Note: Tolleranze generali : UNI EN 22768/1 - f
Smussi non quotati : 1 X 45°
Finiture: Anodizzato duro spessore 20 µm
Quote e tolleranze dopo finitura superficiale
Progettato da: Rongoni Andrea Marzio Riccardo
Controllato da:
Approvato da:
Descrizione: Mozzo anteriore
N. Disegno: E2
Data: 10/02/2020
Materiale: 6082 T6
Quantità: 2
Scala: 1:1
Codice: LHF02P
D-D
E
B-B
Ø69 + sovrametallo 0,3 mm
Ø42
Ø29
Ø17 S7
22
R10
R0,5
2,5
5 Fori equidistanti
Filetto riportato
Hm - 1 - M6 - C - / - 12
R6,5
R8
3 Fori Equidistanti M8
Ø86
Ø68
34
14°
72°
120°
8
+ sovrametallo
0,3 mm
10
+ sovrametallo
0,3 mm
1x45°
(25)
43
13
7,5
R8
2

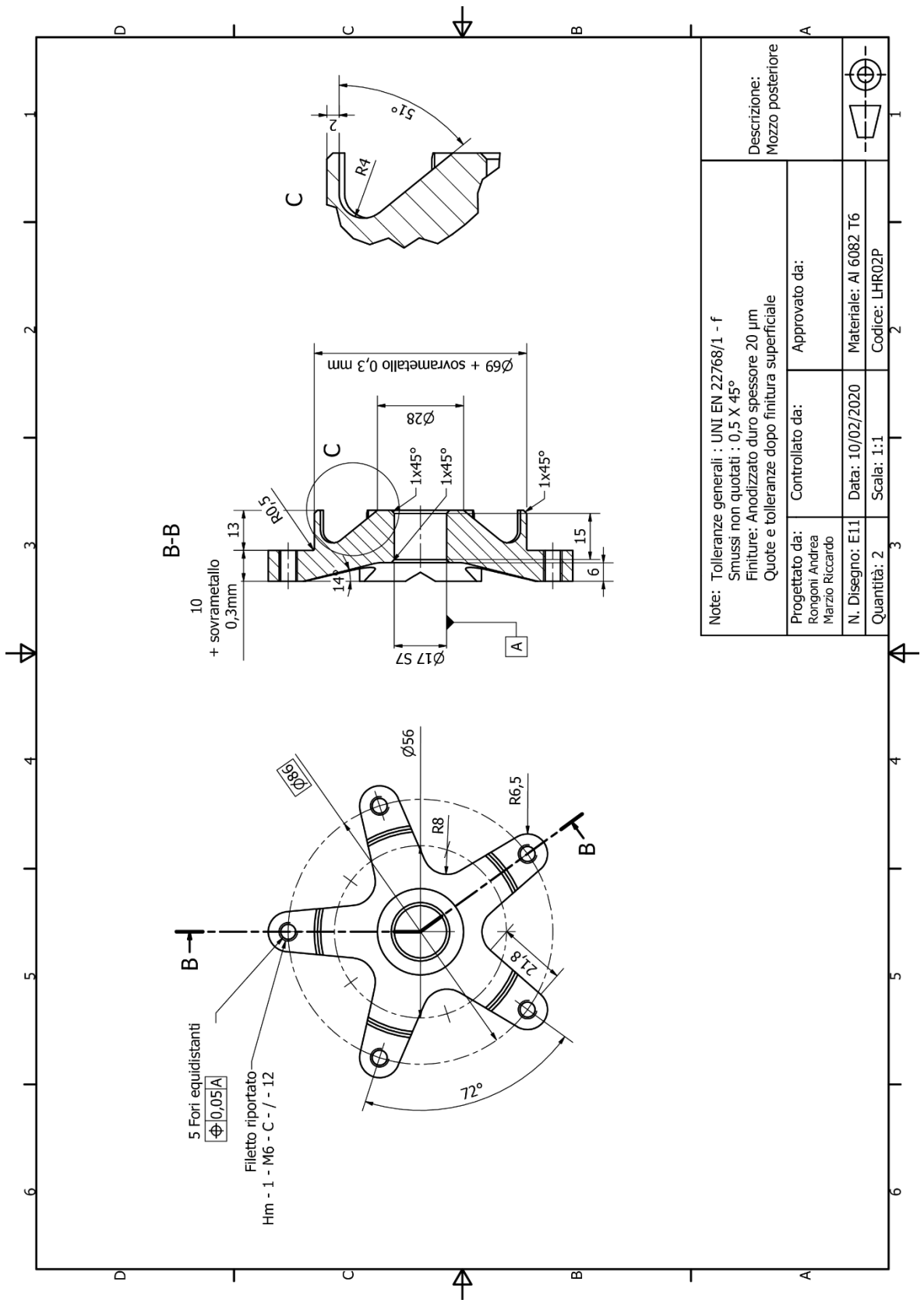
Note: Tolleranze generali : UNI EN 22768/1 - f
Smussi non quotati : 0,5 X 45°
Finiture: Anodizzato duro spessore 20 µm
Quote e tolleranze dopo finitura superficiale
Descrizione: Mozzo posteriore
Progettato da: Rongoni Andrea Marzio Riccardo
Controllato da:
Approvato da:
N. Disegno: E11
Data: 10/02/2020
Materiale: Al 6082 T6
Quantità: 2
Scala: 1:1
Codice: LHR02P
B-B
C
Ø69 + sovrametallo 0,3 mm
Ø28
1x45°
1x45°
1x45°
R0,5
13
14°
15
6
10
+ sovrametallo
0,3mm
Ø17 S7
A
Ø56
Ø86
R8
R6,5
21,8
72°
5 Fori equidistanti
⌖ 0,05 A
Filetto riportato
Hm - 1 - M6 - C - / - 12
R4
2
51°

Bibliography

[1] G. Mastinu & M. Ploechl, *Road and off-road vehicle system dynamics Handbook*, CRC press.

[2] P. Stabile, *Design and realization of a new high-efficiency vehicle for Shell Eco-marathon competition: design of the vehicle chassis*.

[3] J. Capuana, *Progetto delle carene di un veicolo per competizione Shell Eco-Marathon*.

[4] E. Pasta & D. Pistoia, *Design and realization of a new high efficient vehicle for Shell Eco-Marathon competition: design of vehicle subsystems and on-track tests*.

[5] M. Carboni, Lecture notes from "*Laboratorio progettuale di calcolo strutturale*" course.

[6] W. D. Pilkey & D. F. Pilkey, *Peterson's Stress Concentration Factors*, Wiley.

[7] P. Davoli, L. Vergani, S. Beretta, M. Guagliano & S. Baragetti, *Costruzione di macchine 1*, McGraw-Hill.

[8] M. Gobbi, Lecture notes from "*Vehicle design (optimal design)*" course.

[9] F. Levi, *Metodi e Criteri di Progettazione Ottima di Sistemi Complessi*.

[10] A. Bernasconi, Lecture notes from "*Lightweight design for mechanical structures*" course.

[11] S. Beretta, Lecture notes from "*Machine design 2*" course.